

Floating gate MOS based olfactory sensor system

By

Vaibhav Rajesh Dubey

A thesis submitted to the faculty of graduate studies of the University of
Manitoba in partial fulfilment of the requirements of the degree of

Doctor of Philosophy

Department of Electrical and Computer Engineering

University of Manitoba

Winnipeg

Copyright © 2020 by Vaibhav Rajesh Dubey

Abstract

The mammalian olfactory senses often help mammals take many important actions. The olfaction ability of animals is a synchronised action of the olfactory organ and the brain. An electronic sensing system that can mimic the mammalian olfactory senses can be paired with the mature electronic computing platforms to be utilized in different applications. This work demonstrates the development of an electronic olfaction system which is based on integration of gas sensitive conducting polymers and Floating Gate Metal Oxide Semiconductor (FGMOS) sensors. The commercially available Taiwan Semiconductor Manufacturing Company (TSMC) 350 nm technology process was used for the design of the integrated circuits of this work. The FGMOS sensors were designed with a conductive extension of the floating gate terminal to a sensing surface. Multiple postprocessing steps were developed and practiced, creating the semiconductor chip compatibility to different sensing polymers and their electrochemical deposition environment. A sensing polymer, polypyrrole for example, was electrochemically deposited onto this sensing surface. The analyte influenced response of gas sensitive polymers was tailored by adopting different techniques at the time of electrodeposition of the polymer films. A novel integrated system having an array of FGMOS sensors coupled to these chemically diverse polymers was developed. The sensors in the array were accessed and analysed individually using a specially designed addressing circuit. The experiments performed under this work involved as many as six chemically distinct polymers on a single chip. These polymers were synthesised using pyrrole and aniline monomers. Acetone, ethanol, methanol, isopropyl alcohol, petrol, toluene, ammonium hydroxide, acetic acid and water vapours were used to test the sensor system. Individual sensors coupled to distinct sensing polymers produced unique responses to the given analytes. The comparative measurements of these different sensor responses upon exposure to any

vapour analyte facilitated a group signature-like response. The experiments have confirmed functional system response to different vapour analytes and their concentrations. A statistical data analysis technique, principal component analysis (PCA), was used to process the “analyte fingerprints” generated by the sensor array. In experiments involving multiple random order exposures of different vapour analytes, the PCA method produced a graphical representation having different isolated clusters of datapoints where each cluster corresponds to an analyte under test. This technique was demonstrated for its effectiveness in detection of any ‘unknown vapour analyte’ from the given set of analytes. The commercial CMOS technology used for this work enables the possibility of cost-effective large-scale production of these chips. The ability to tailor the polymer sensitivity to different vapour analytes has potential for development of the system specific to different industrial applications.

Acknowledgements

The written words have an unfortunate tendency to convert genuine gratitude into a stilled formality, but they create permanent impressions. I would like to take this opportunity to thank the people who have contributed their time and efforts in helping me complete the graduate research successfully.

To begin with, I must start with expressing my greatest gratitude to Prof. Douglas Buchanan, my research advisor. Dr. Buchanan's knowledge, critical thinking and hard work comes out as an inspiration to me. He has always been there to share his expertise in this field and most valuable supervision to this PhD research. Dr. Buchanan has been continuous support in my academic journey and at times even beyond that. I feel very fortunate to get this opportunity to work under his supervision and learn from him. Working with Dr. Buchanan has shaped my professional future and I look forward to staying in contact with him always.

I would like to sincerely thank Dr. Michael Freund and members of his research group, especially Dr. Akin Iyogun, for sharing valuable information and suggestions related to the sensing polymers. Members of my advisory committee, Dr. Thomson and Dr. Gericke, always shared valuable inputs and suggestions during the progress report meetings. I appreciate and thank their contribution to shape this research work.

I received a lot of support from Daryl Hamelin, Dwayne Chrusch and Cory Smit for any technical difficulties during this research period. I thank them all for all their support.

The research work was supported by the Natural Science and Engineering Research Council of Canada (NSERC), the Canadian Foundation of Innovation (CFI) and Canadian Microelectronics Corporation (CMC). Jim Quinn from CMC worked tirelessly during the design submission process to ensure timely submission of designs to the foundry, Thank you Jim.

My friends at the university, Robin Raju, Mayank Thacker and Anton Vykhodtsev, created a pleasant working environment and shared their technical expertise to help me whenever it was required. They make this long journey look short, thank you. Amy Dario, our graduate student advisor, deserves a special mention for her all you can eat candies supply which was the biggest reason that some of us could work long hours in the lab, Thank you Amy. And last but not the least, I would like to thank my family, friends, and everyone else who have helped in any possible way in carrying out this work successfully.

Dedicated to

The frontline health care workers
during Covid-19

Table of Contents

Abstract	ii
Acknowledgements	iv
Table of Contents	vii
List of Figures	ix
List of Tables	xv
List of Symbols	xvi
List of Abbreviations and Acronyms	xvii
Chapter 1 – Introduction	1
1.1 Literature review	2
1.2 Thesis outline	9
Chapter 2 – Design of sensor chip	12
2.1 Floating Gate Metal Oxide Semiconductor transistor	12
2.2 Address and Control circuits	22
2.3 Transimpedance Amplifier	25
2.4 Analog to Digital converter	27
Chapter 3 – Post processing and Polymer deposition	31
3.1 Electroless Gold Plating	32
3.2 Electrodeposition setup	35
3.3 Selective encapsulation and electrochemical cell setup	38

3.4 Polymer depositions	44
Chapter 4 – Sensor characterization for analyte exposure	49
4.1 The vapour flow setup	49
4.2 Polymer coated sensor transfer characteristics.....	52
4.3 Coupled charge analysis	56
4.4 Sensor transient response.....	63
Chapter 5 – Discussions, conclusion, and future work	92
5.1 Discussion on polymer sensing mechanism	92
5.2 Conclusion	97
5.3 Future Work.....	100
References.....	102

List of Figures

Fig. 1.1 Cross sectional diagram of a typical metal oxide gas sensor	3
Fig. 1.2 A typical design of two port surface acoustic wave (SAW) gas sensor	
Fig. 1.3 Cross sectional diagram of a typical metal oxide gas sensor	3
Fig. 2.1 Schematic diagram of an n type FGMOS transistor	13
Fig. 2.2 Energy Band diagram of n type FGMOS at Fowler Nordheim tunneling.....	14
Fig. 2.3 An extended floating gate design for n type FGMOS sensor	15
Fig. 2.4 An extended floating gate design of the FGMOS sensor functionalized using a sensing polymer	16
Fig. 2.5 Schematic representation of FGMOS bias setup and expected change in sensor current on exposure to different vapor analytes	17
Fig. 2.6 Transfer characteristic of the FGMOS sensors having different WL ratios	19
Fig. 2.7 Cadence virtuoso layout view of the Chip.....	20
Fig. 2.8 A block schematic for the designed Olfactory Sensor system chip	21
Fig. 2.9 The address and control signal generation logic for 8 x 8 sensor array	22
Fig. 2.10 Schematic representing FGMOS addressing scheme in an array cell	23
Fig. 2.11 Cadence virtuoso layout view of the array cells.....	24

Fig. 2.12 A schematic diagram for the transimpedance amplifier circuit (the annotations inside the amplifier blocks indicates the names used for the cadence schematic circuits)	25
Fig. 2.13 (a) Simulated electrical response (b) actual electrical characteristics of the transimpedance amplifier.....	26
Fig. 2.14 Block schematic representation of the analog to digital converter.....	27
Fig. 2.15 Block schematic representation of a 3-bit flash type analog to digital converter.....	30
Fig. 3.1 (a) Nickel coated extended floating gate pads (b) SEM image for nickel surface and (c) EDS analysis for the surface to confirm presence of nickel layer	33
Fig. 3.2 (a) Gold coated extended floating gate pads (b) SEM image for gold surface and (c) EDS analysis for the surface to confirm presence of gold layer.....	35
Fig. 3.3 Mechanical clamp setup used for the electrodeposition process	37
Fig. 3.4 The packaged chip with selective Encapsulation of wirebonds using SU-8	39
Fig. 3.5 Schematic diagram of the 3- electrode cell setup	40
Fig. 3.6 Cycling behavior of 0.2 M Pyrrole, 0.1 M pTSA solution in DI water measured at gold plated floating gate electrode	41
Fig. 3.7 Undesired polymer growth on the wire bonds exposed to the electrolytic solution.....	42
Fig. 3.8 (a) Chip package with double layer of SU-8 encapsulation (b) A chip package with encapsulation and an additional coating of nail polish	43

Fig. 3.9 Cyclic voltammograms of (a) pyrrole monomer with sulfuric acid (red) and oxalic acid (black) (b) styrene monomer doped with Bu₄NBF₄ and (c) aniline monomer with pTSA (red) and sulfuric acid (black) showing different electrodeposition potentials available to grow the polymer films 45

Fig. 3.10 The current measured at the floating gate terminal as a function of time during electrodeposition of pyrrole films using (a) 0.075M pyrrole monomer with 0.1M sulfuric acid and (b) 0.1 M pyrrole monomer with 0.1M oxalic acid 46

Fig. 3.11 Chemically diverse Conducting Polymer films grown on the extended floating gate pads of the 4x4 sensor array, PPy/H₂SO₄ films on row 0, PPy/oxalic acid films on row 1 and clean gold coated extension pads in row 3 and 4 47

Fig. 3.12 (a) The current measured at the floating gate terminal of row-5 sensors as a function of time during electrodeposition of PANI film using 0.1M aniline monomer with 0.1M sulfuric acid and (b) PANI films grown on the extended floating gate pads of the 8x8 sensor array 48

Fig. 4.1 Vapour flow setup for characterization of system in controlled analyte vapour environment (MFC : Mass flow controller) 49

Fig. 4.2 Electrical characteristics of the FGMOS sensor (a) Drain characteristics (b) Transfer characteristics..... 51

Fig. 4.3 (a) Transfer characteristics of the PPy/H₂SO₄ coated sensor in 6 different analytes after 1 hour of exposure and (b) rescaled plot of it on linear scale of drain current 52

Fig. 4.4 (a) Transfer characteristics of the of the PPy/Oxalic acid coated sensor in 6 different analytes after 1 hour of exposure and (b) rescaled plot of it on linear scale of drain current..... 54

Fig. 4.5 (a) Transfer characteristics of the PPy/KCl coated sensor in 6 different analytes after 1 hour of exposure and (b) rescaled plot of it on a linear scale of drain current	54
Fig. 4.6 (a) Transfer characteristics of the PPy/pTSA coated sensor in 6 different analytes after 1 hour of exposure and (b) rescaled plot of it on a linear scale of drain current	54
Fig. 4.7 (a) Transfer characteristics of the PANI/H ₂ SO ₄ coated sensor in 6 different analytes after 1 hour of exposure and (b) rescaled plot of it on a linear scale of drain current	55
Fig. 4.8 (a) Transfer characteristics of the PANI/pTSA coated sensor in 6 different analytes after 1 hour of exposure and (b) rescaled plot of it on a linear scale of drain current	55
Fig. 4.9 Normalised threshold voltage (ΔV_{THN}) relative to nitrogen for 4 PPy and 2 PANI based sensors doped with variable dopants for their exposure to 6 analytes	58
Fig. 4.10 Normalised change in sensor current of 4 PPy and 2 PANI based sensors doped with variable dopants for their exposure to 6 analytes.....	62
Fig. 4.11 Transient response of PPy/pTSA based sensor for exposure to 4 analytes	64
Fig. 4.12 Transient response of PPy/H ₂ SO ₄ based sensor for cyclic exposure to nitrogen and toluene.....	65
Fig. 4.13 Transient response of PPy/H ₂ SO ₄ based sensor for exposure to methanol.....	66
Fig. 4.14 Transient response of PPy/H ₂ SO ₄ based sensor for exposure to 4 analytes.....	67
Fig. 4.15 Transient response of PPy/KCl based sensor for exposure to different concentration of petrol vapours.....	68
Fig. 4.16 Transient response of PPy/Oxalic acid based sensor for exposure to different concentration of water vapours.....	69
Fig. 4.17 Transient response of PANI/pTSA based sensor for exposure to water and petrol	70

Fig. 4.18 Transient response of PANI/pTSA based sensor for exposure to different concentrations of water vapour	71
Fig. 4.19 Transient response of PANI/pTSA based sensor for exposure to different concentrations of methanol	72
Fig. 4.20 Transient response of PANI/ H ₂ SO ₄ based sensor for exposure to water vapour.....	73
Fig. 4.21 Steady state response of PPy / H ₂ SO ₄ and PPy / Oxalic acid sensor for exposure to water vapour	75
Fig. 4.22 Comparison of PPy/H ₂ SO ₄ and PPy/Oxalic sensor response to 6.315% water vapour relative to nitrogen	76
Fig. 4.23 Steady state response of PPy/KCl sensor for exposure to 7 different analytes	77
Fig. 4.24 Comparison of PPy/KCl sensor response to 6.315% flow of 7 different analyte vapours relative to nitrogen	78
Fig. 4.25 Steady state response of PANI/H ₂ SO ₄ and PANI/pTSA sensor for exposure to 4 different analytes and nitrogen	79
Fig. 4.26 Comparison of PANI/H ₂ SO ₄ and PANI/pTSA sensor response to 6.315% flow of 4 different analyte vapours relative to nitrogen	80
Fig. 4.27 Steady state response of PPy/H ₂ SO ₄ (S1), PPy/oxalic (S2) and PPy/KCl (S3)sensor for exposure to 6.315% flow of 8 different analytes and nitrogen.....	81
Fig. 4.28 Comparison of PPy/H ₂ SO ₄ (S1), PPy/oxalic (S2) and PPy/KCl (S3) sensor response to 6.315% flow of 8 different analyte vapours relative to nitrogen	82
Fig. 4.29 Comparison of PPy/H ₂ SO ₄ (S1), PPy/oxalic (S2) and PPy/KCl (S3) sensor response to 6.315% flow of 8 different analyte vapours relative to nitrogen, 3 different sets of exposure.....	83

Fig. 4.30 Principal component analysis of PPy/H ₂ SO ₄ (S1), PPy/oxalic (S2) and PPy/KCl (S3) sensor response to 6.315% flow of 8 different analyte vapours relative to nitrogen, 3 different sets of exposure.....	85
Fig. 4.31 Comparison of PPy/H ₂ SO ₄ (S1), PPy/pTSA (S2), PANI/ H ₂ SO ₄ (S3) and PANI/pTSA (S4) sensor response to 6.315% flow of 6 different analyte vapours relative to nitrogen, 3 different sets of exposure.....	87
Fig. 4.32 Principal component analysis PPy/H ₂ SO ₄ (S1), PPy/pTSA (S2), PANI/ H ₂ SO ₄ (S3) and PANI/pTSA (S4) sensor response to 6.315% flow of 6 different analyte vapours relative to nitrogen, 3 different sets of exposure.....	88
Fig. 4.33 Comparison of PPy/H ₂ SO ₄ (S1), PANI/ H ₂ SO ₄ (S2) and PPy/oxalic (S3) sensor response to 6.315% flow of 7 different analyte vapours relative to nitrogen, 3 different sets of exposure cycles	89
Fig. 4.34 Principal component analysis of PPy/H ₂ SO ₄ (S1), PANI/ H ₂ SO ₄ (S2) and PPy/oxalic (S3) sensor response to 6.315% flow of 7 different analyte vapours relative to nitrogen, 3 different sets of exposure cycles.....	90
Fig. 5.1 Typical structure of (a) polypyrrole and (b) polyaniline conducting polymers in their intrinsic state	93
Fig. 5.2 Mechanism of polaron formation on polypyrrole backbone through oxidation doping..	94

List of Tables

Table 4.1 The observed threshold voltage at control gate under influence of vapour analytes....	57
Table 4.2 The Observed change in threshold voltage (ΔV_{THN}) relative to Nitrogen.....	57
Table 4.3 The calculated numbers for change in electron count in the channel.....	61

List of Symbols

μ_n	Average electron mobility	$\text{cm}^2/(\text{V}\cdot\text{s})$
Q_b^{inv}	Charge per unit area in the depletion region at inversion	C/cm^2
Q_{SS}	Charge due to gate oxide imperfections	C
ϵ_{Si}	Permittivity of silicon	$\text{C}/(\text{V}\cdot\text{m})$
ϕ_F	Electrostatic potential of the substrate	V
ϕ_S	Electrostatic potential at the oxide silicon interface	V
ϕ_{ms}	Surface potential between the substrate and the polysilicon gate	V
C_{ox}	Gate-oxide capacitance per unit area	F/cm^2
I_{DS}	Drain-Source Current	A
L	Length of the channel	μm
N_A	Substrate doping concentration (p type)	cm^{-3}
q	Electron charge	C
Q_b	Charge per unit area in the depletion region	C/cm^2
V_{CG}	Control gate voltage	V
V_{DS}	Drain voltage	V
V_{FG}	Floating gate voltage	V
V_{REDOX}	Redox potential at working electrode for polymer electrodeposition	V
V_S	Source voltage	V
V_{SUB}	Substrate voltage	V
V_{THN}	Threshold voltage of nFET	V
W	Width of the channel	μm

List of Abbreviations and Acronyms

A/D	Analog to digital
Ag/AgCl	Silver/silver chloride
BAW	Bulk acoustic wave
CMC	Canadian Microelectronics Corporation
CMOS	Complementary Metal Oxide Semiconductor
CPGA	Ceramic Pin Grid Array
CV	Cyclic Voltammetry/Voltammogram
EDS	Energy dispersive x-ray spectroscopy
FET	Field effect transistor
FGMOS	Floating Gate Metal Oxide Semiconductor
FN	Fowler-Nordheim
GPIO	General-purpose input/output
I/O	Input/output
IDE	Interdigitated electrode
IDT	Interdigital transducer
ILD	Inter-layer dielectric
I-V	Current-Voltage
MIR	Mid-infrared
MOSFET	Metal-oxide-semiconductor field-effect transistor
nMOS	n-type metal-oxide-semiconductor
PANI	Polyaniline

PCA	Principal component analysis
pMOS	p-type metal-oxide-semiconductor
poly1	The lower polysilicon layer
poly2	The upper polysilicon layer
PPy	Polypyrrole
pTSA	p-toluenesulfonic acid
QCM	Quartz crystal microbalance
Redox	Oxidation-Reduction
SAW	Surface acoustic wave
SMU	Source/measurement units
TSMC	Taiwan Semiconductor Manufacturing Company

Chapter 1 – Introduction

Humans have made great technological advancements in the last century. Use of multiple different electronic systems has become a common practice of daily life. Sensors are an important part of many of these electronic systems. The availability of a wide variety of sensors to detect different physical responses is assisting in the design of better solutions to improve the living environment. These sensors are an essential part of many handheld devices, earning them a tag of being ‘smart’. Humans have five basic senses: vision, hearing, touch, taste and olfaction. The first three of these senses are responsive to physical interaction whereas the taste and olfaction abilities are based on chemical responses to different analytes. To develop an artificial intelligence system, capable of replicating human olfaction abilities, sensors capable of detecting chemical stimulants need to be developed.

The sense of smell provides very useful information to animals by helping to analyse, distinguish or identify numerous odorants. The mammalian olfactory system senses different smells when the odor molecules bind with the olfactory receptor neurons located at the olfactory epithelium in the nasal cavity. The olfactory receptor neurons act as transducers to translate the odor information into electrical signals. These electrical signals are received by the olfactory bulb which processes and communicates the odor information to the brain [1][2]. Research on developing artificial olfactory systems, as the means to extract information from odorants, has grown tremendously [3][4][5]. The approach towards the development of artificial olfactory systems generally resembles their biological counterparts where an active layer reacts to chemical stimuli of the odorant and generate signals for advanced processing of the information. The broad and diverse range of smells animals can process are a result of at the very least, millions of years of evolution. Research in chemistry has shown promise and potential to develop advanced

vapour sensitive materials, taking these devices closer to a truly artificial olfactory sensor platform that closely mimics its biological equivalent. The recent advancements in chemistry have given new potential materials and multiple chemical derivatives thereof, with the potential to deliver an effective olfactory sensing platform. One such class of materials is conducting polymers which have change in their electrical properties with exposure to different odorant vapours [6][7][8]. The objective of this research is to integrate these gas sensitive polymers to an electronic platform for development of a small and inexpensive olfactory sensor chip.

1.1 Literature review

Over the years, a number of gas sensing systems have been developed using many different sensing mechanisms [3][4][5][9][10]. The first reported olfaction system was introduced as a mechanical nose by Moncrieff in the early 1960s [11]. This research was followed by the development of many different sensing mechanisms which can be broadly categorised as metal oxide sensors, conducting polymers, bioelectronics noses, optical and/or piezoelectric sensors [3][4][5][9][10]. The first metal oxide sensor based on zinc oxide film was reported in the year 1962 [12]. Most commercially available electronic nose systems are based on metal oxide sensors technology [10][13][14]. The operation of metal oxide gas sensors is based on the principle of change in conductance of an oxide layer when it is exposed to a gas analyte. This change in conductance is (usually) proportional to the concentration of the exposed analyte [9][15]. The metal oxide films typically have lower conductivity and less surface activity at ambient temperatures. The sorption properties of metal oxide layers and the rate of any surface reaction with the analyte vapours are improved by operating the sensors at elevated temperatures [16]. The selectivity of these sensors is modified by doping the oxide layer with different noble metals [14][17][18]. The metal oxide sensors have strong sensitivity compared to other types of gas

sensors, a relatively fast response time for analyte detection and are compatible to standard silicon processing which makes them cost effective [10][14][17]. The metal oxide sensors require high operating temperatures which is their major limiting factor. For an integrated design application, they would require an on-chip microheater which is linked to higher power consumption, making it difficult to be used in a handheld or mobile device [9][14]. However, the metal oxide sensor technology still remains the most common olfactory sensor platform and different research efforts have been reported that show an improvement in their performance [15]. The recent work in the implementation of such systems, use nanostructured materials such as nanowires/nanotubes as well as other new materials some of which show promise for the future of the metal oxide sensor technology [15][19][20]. A cross sectional diagram of a typical metal oxide gas sensor is shown in Fig. 1.1. An anisotropically etched substrate with the heating element creates a micro hotplate structure. The metal oxide sensing layer lies on top of the heating element, insulated by the dielectric passivation layer.

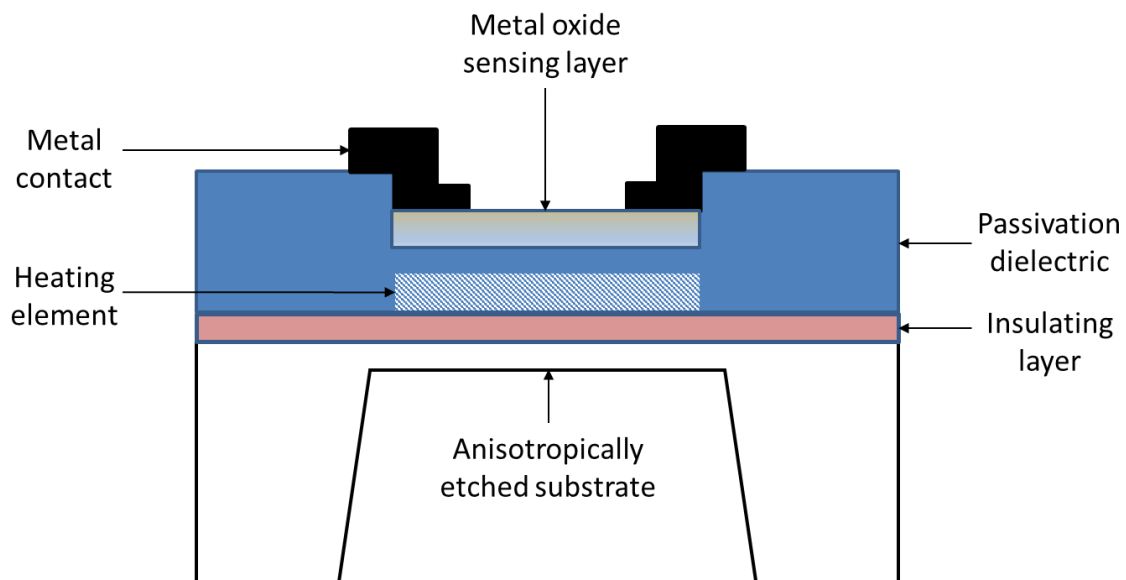


Fig. 1.1 Cross sectional diagram of a typical metal oxide gas sensor

A bio-electronic nose is a relatively new but promising class of olfaction system based on the use of biological olfactory receptors as sensing elements for detecting different odorant molecules [3][21][22]. The biological sensing elements in these systems are either olfactory receptor proteins or olfactory receptor cells [23]. The sensing mechanism of a bioelectronic nose is a two layer structure where the primary layer of biological olfactory receptor cells or receptor proteins, interacts with the exposed analyte vapour to generate a biochemical signal and the second layer of transducer converts it to an electrical signal [3]. Different mechanisms, such as the use of microelectrodes, resonance detection, piezoelectric layers and optical detectors have already been used as a secondary layer electrical transducer [3][23]. The bio-electronic nose has compatibility with traditional silicon systems, that enables their potential for mass production using commercial silicon technologies [3][24]. The selectivity of the bioelectronic nose is high (reported up to 0.02 parts per trillion) as its receptor layer is developed using biological olfactory receptor proteins/cells which are able to detect most of the odors human nose can respond to [25][26][27]. The sensitivity of these systems is dependent on the properties of the transducer layer and its integration with biological receptor cells [25]. Recent advancements in biotechnology are helping researchers find new methods of binding the olfactory bio-cells of the bio-electronic noses to the transducer layer. In recent research, a bioelectronic nose developed using protein nanowires has shown the highest sensitivity, up to 10 parts per billion, for detection of ammonia gas [26]. New nanomaterials, like graphene and carbon nanotubes, have also been reported for their possible application in bioelectronic nose system for improving its sensitivity [3][25][28]. The bioelectronic nose has shown great potential to be a promising olfactory sensor platform. However, there are still some limitations that include stability, repeatability of measurements and the ease of integration as a single chip olfactory sensor platform [3][28]. With

continued research in this area, improvements in the performance of bioelectronic noses can be expected in the future.

Piezoelectric sensors are very popular for a wide range of sensing applications. They are also reported to be used as acoustic wave sensors in different gas sensing applications [9][10][29][30]. These sensors employ different piezoelectric materials to generate an acoustic wave which travels through or along their surface [29][30]. The nature of travel for the acoustic wave is used to classify the sensors as surface acoustic wave sensors (SAW) or bulk acoustic wave sensor (BAW), also known as Quartz crystal microbalance (QCM) [10][30][31]. When used in gas sensing applications, the acoustic wave sensors use a thin coating of different gas sensitive materials on piezoelectric structures. Upon exposure to a vapour analyte, the gas sensitive layer interacts with vapour molecules of the analyte to produce a change in its physical properties which is reflected as a resultant change in the resonant frequency of the sensor [9][30][32]. The first acoustic wave based sensor for vapour detection was developed as a sorption detector by applying coatings of different vapour sensitive materials to a quartz crystal microbalance in 1964 [33]. The SAW sensors can operate at much larger frequencies as compared to the QCM devices. The higher frequency of operation results in greater frequency variations upon analyte exposure. This leads to the higher sensitivity of SAW sensors over the QCM [34].

A typical design for a two port SAW gas sensor is shown in Fig. 1.2. The design is based on a piezoelectric substrate on top of which two interdigital transducers (IDT) are patterned. These metallic IDTs form a delay line structure where the propagation delay of the wave travelling from the input to the output IDT is determined by the distance between the two IDTs. For gas sensing applications, a gas sensitive layer is deposited in-between the two IDTs. The input IDT is supplied with a suitable electrical signal to generate an acoustic wave, the wavelength of which

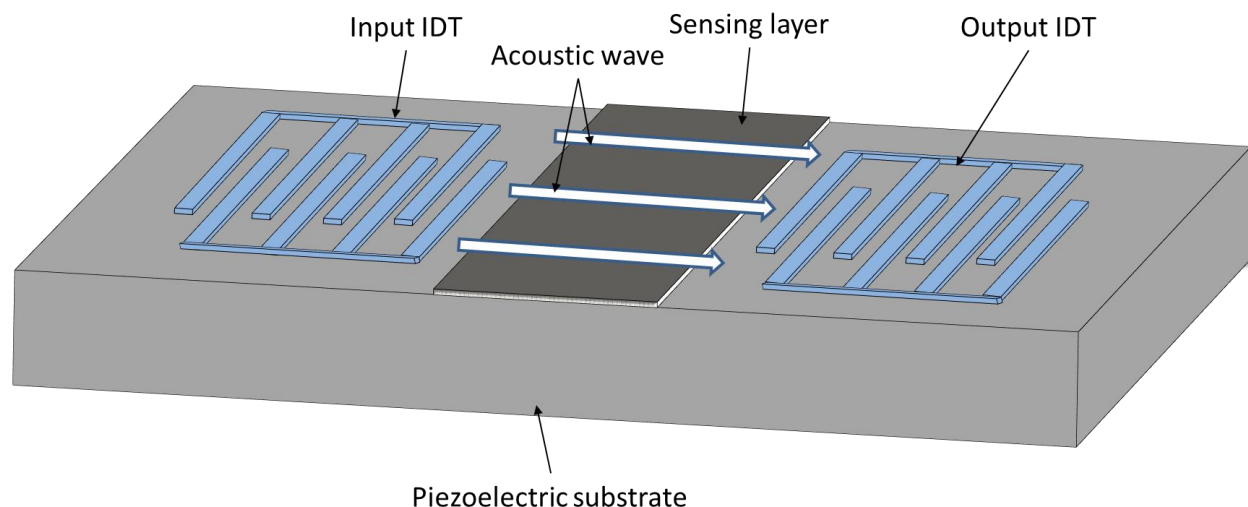


Fig. 1.2 A typical design of two port surface acoustic wave (SAW) gas sensor

primarily depends upon the dimensions of the IDT structure. The surface wave has a substrate penetration depth of the order of the wavelength. When the sensor is exposed to an analyte, any change in the properties of the sensing layer produce a change in the frequency of the wave received at the output IDT [35][36]. Different electrical instruments and/or processing circuits may be used at the output IDT to detect frequency variations and hence for the purpose of vapour detection. The silicon compatible designs give these sensors advantages of small size, low power operation and lower cost. For olfactory applications, they are reported to have advantages of high sensitivity and fast response time. Reproducibility of results and higher dependency on environment variables like temperature or humidity are primary causes of concern for these systems [9][10][30][36].

There are also olfactory systems based on optical sensors for vapour detection which work based on the interaction of gas molecules with electromagnetic light waves. Many different vapour molecules show strong absorption characteristics for light which is dependent on the light wavelength. The unique absorption bands shown by these analytes to the electromagnetic

light waves form the basis of detection and measurement of the analyte vapours [37][38]. For the optical gas sensors based on absorption properties, the mid-infrared (MIR) region of the light spectrum is of particular interest. In this region, the light absorption is based on energy state transitions owing to the fundamental mode of molecular vibrations or rotations. This leads to the MIR region having narrow and isolated absorption bands for many of the analytes of industrial interest [37][38][39]. The optical sensors for olfactory systems offer multiple possibilities for extraction of information, like measurement of reflection, refraction, luminance, fluorescence, wavelength or absorbance [10][37][38][40]. This can be very helpful in designing a higher sensitivity system with lesser number of sensors in the array. Different research groups have worked on developing vapour sensors using different types of optical fibers [41]. A general design of an optical olfactory sensor array is incorporated with a group of multimode optical fibers with their tips coated with different gas sensitive materials, generally polymers [10][41]. The optical olfactory systems have a fast response time, good sensitivity and good selectivity for many analytes but are complex and expensive. Packaging of these systems is an important limiting factor that needs to be addressed well in order to overcome the noise generated because of optical interference [37][39][41].

Conducting polymers, after their evolution in the late 1970's, became a well-researched class of materials in the field of olfactory sensors. Polypyrrole, Polyaniline, Polystyrene, Polythiophene, Poly(3,4-ethylenedioxythiophene) (PEDOT) and their chemical derivatives are some of the more frequently used conducting polymers for the gas sensor applications [42]–[46]. Since the year 2000, when the joint Nobel Prize in chemistry was awarded to Heeger, MacDiarmid and Shirakawa "for the discovery and development of conductive polymers", the research in this domain has intensified [47]. The conducting polymers operate at

room temperature and can be easily deposited using electrochemical deposition techniques. The electrochemical process using the three-electrode setup for electrodeposition of conducting polymers provides better control over the polymerization process and is a preferred method for polymer synthesis for different sensor applications [8][46]. The flexible nature of conducting polymers make them a suitable material for printable electronics that has huge demand in the application of wearable electronics [48]. The conducting polymers offer a fast response time and high sensitivity towards many analytes [44][45][49]. The sensitivity of polymers is based on a number of possible mechanisms such as oxidation or reduction of polymer, mobility variation of charge carriers in polymer chains, change in the energy band structure of polymer or possible physical change such as swelling or shrinking of polymer on interaction with analyte particles [8][47][50]. The high sensitivity of the conducting polymers results in their lower selectivity for different analytes [50]. A major feature of conducting polymers is their tunable physical and chemical properties using different dopants in the polymer film [7][46][51][52]. The dopants can be easily introduced into the polymer films by adding them in the electrolytic solution used for the electropolymerization process.

To improve selectivity and synthesise multiple chemically diverse conducting polymers, Dr. Freund's group, a collaboration from the chemistry department at Dalhousie University, have reported many techniques for polymer deposition including the use of different monomer units for polymer synthesis, co-deposition of different monomer units to create a copolymer, polymerisation at different oxidation potentials and the use of different dopants for polymer depositions [7][8][53][54]. In the thesis of one of Dr. Freund's past Ph.D. students 81 chemically diverse conducting polymer derivatives were reported [54]. These polymers were used for chemical identification of 12 different analytes by analysing the change in their resistivity with

exposure to analyte vapours. The statistical method of principal component analysis was used for processing the measurement results [54]. These findings indicated a modification in the electrical properties (resistivity) of the conducting polymer upon exposure to different analytes. In past work, in collaboration with colleagues in the Chemistry department, the Floating Gate Metal Oxide Semiconductor (FGMOS) transistor with polypyrrole (PPy) as the sensing polymer was successfully tested for sensitivity to different analytes [55][56].

1.2 Thesis outline

In this thesis, the design, development, and electrical characterization of an olfactory sensor system using array of the FGMOS sensors, integrated to different chemically diverse conducting polymers is presented. This research was focused on improving the performance of the FGMOS sensor from previous work, design and fabricate the electrical circuits around the sensor to develop a multiple sensor system, develop an optimal method and flow for the integration of gas sensitive polymers to the sensors, electrical characterization of the sensor system and finally develop the advanced data processing required. The thesis is organised in 5 chapters. In Chapter 1, a brief overview of several different popular techniques used for the design of gas sensors is given.

The FGMOS is a dual-gate transistor (control gate and floating gate) in which a change in the charge density on the floating gate causes a shift in its normal electrical characteristics. Chapter 2 contains a description of the tunnelling mechanism observed in the FGMOS transistors when used in the electrical flash memory. The extended floating gate structure of the FGMOS sensor, designed in this work, is also explained. In the design of these olfactory sensors, the floating gate terminal is extended to a contact pad surface designed using the topmost metal layer of the given semiconductor technology, which is used for deposition of sensing

polymer like polypyrrole. This chapter continues with an explanation of the designs of different electrical circuits that were used in the development of an FGMOS sensor array-based system. The chip in this research is designed to act as a “sensing platform” where multiple sensing polymers can be used with an array of FGMOS sensors to generate a unique electrical response for many tested analytes.

Unfortunately, the top metal layer of this silicon technology is not compatible with the polymer electrodeposition process. The top metal compatibility issue was resolved using a selective electroless deposition process of a noble metal onto the top metal surface. A process of selective encapsulation of the bond wires was developed to address the other electrodeposition problems. In Chapter 3, the details of these post fabrication processing steps, developed to resolve the chip compatibility problems encountered during the polymer electrodeposition process, is discussed. The chemical recipes used for the synthesis of the polymers and the three-electrode electrochemical cell apparatus is also explained.

Interaction of analyte vapour molecules with the polymer-integrated sensor produces a change in the electrical characteristics of the sensor. Different experiments were performed to study the sensor behaviour in presence of many different vapour analytes. These experiments were performed for sensors having multiple chemically diverse polymers and the responses were measured and compared. The electrical setup for all such experiments and the measured sensor responses are given in Chapter 4. A dataset was developed from multiple random order exposures of different analytes and a statistical technique, principal component analysis, was used for data processing. The results of the statistical analysis were found to be very useful to enable selectivity and sensitivity, about the detected analyte. A demonstration of this approach using principal component analysis for the detection of unknown vapour analytes is discussed in

this chapter.

Discussions on some of the analyte interaction mechanisms with the polymers and their effect on electrical characteristics of the sensor are presented in Chapter 5. The discussions are followed by conclusions from the experimental observations and suggestions to lay a possible direction for the future work in this project. This type of sensing platform would be useful in a wide variety of applications such as the automobile, food, cosmetic, packaging, drug, analytical chemistry and biomedical industries. In such industries, these sensors could be used for a broad and diverse range of purposes including quality control of raw and manufactured products, process design, freshness and maturity (ripeness) monitoring, shelf-life investigations, authenticity assessments etc.

Chapter 2 – Design of sensor chip

The objective of this research was to develop a small, inexpensive programmable olfactory sensor platform using the commercially available silicon technologies. The Complementary Metal Oxide Semiconductor (CMOS) devices on the silicon substrate are used as the fundamental building blocks for many integrated circuits in the present-day electronics. The CMOS technology has many advantages that include high speed of operation, low power consumption and well-established mass production technology which makes it an obvious choice for many researchers for the development of designs ideas. For the research in this study, the “*cmosp35*” silicon technology available through Taiwan Semiconductor Manufacturing Company (TSMC) was used for the fabrication of the integrated circuit design.

2.1 Floating Gate Metal Oxide Semiconductor transistor

The Floating Gate Metal Oxide Semiconductor (FGMOS) transistor is a well-known device that had been used extensively in flash semiconductor memories [57]. It also has been used as a sensor in other electronic systems [58][59]. The structure of the FGMOS transistor is different from that of conventional CMOS transistors in terms of the number of gate terminals. The FGMOS transistor has two gate terminals, referred as control gate and floating gate. These transistor gate structures are designed with a silicon technology that has two distinct polysilicon layers. The *cmosp35* (from TSMC) technology used for this design is one of the few available that offers two polysilicon layers. In Fig. 2.1 a schematic view of an n-type FGMOS transistor is shown.

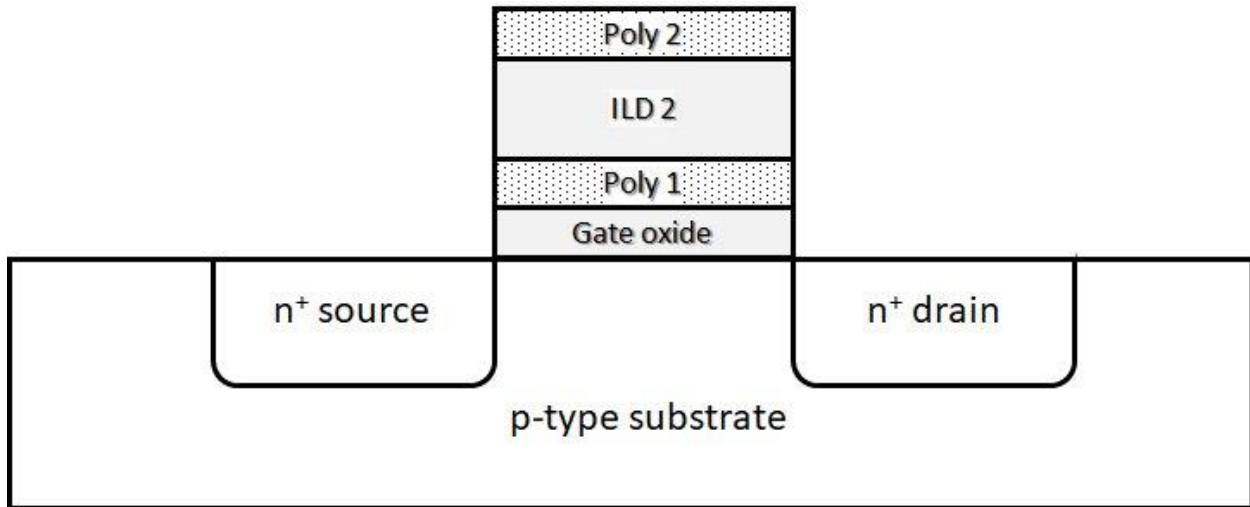


Fig. 2.1 Schematic diagram of an n type FGMOS transistor

The lower polysilicon layer (*poly1*) is the “floating gate” and is isolated from the silicon substrate by a thin insulating layer of silicon dioxide. The upper polysilicon layer (*poly2*) forms the control gate, which overlaps the floating gate (*poly1*) in sandwiched between a thick layer of dielectric (ILD2) and the thin gate oxide. For the given *cmosp35* technology, the thickness of gate oxide is ~7 nm and the ILD2 is ~36 nm. The gate terminals in the FGMOS structure are capacitively coupled to each other. In the normal mode of operation of a FGMOS transistor, the charge carriers from the substrate are tunnelled through the thin layer of gate oxide onto the floating gate layer of the device by applying a suitable electrical bias condition. As the floating gate structure is electrically isolated from the substrate as well as the control gate, the charge on floating gate gets trapped. The trapped charge on the floating gate layer modifies the electrical characteristics of the FGMOS structure with respect to its operation from the control gate [60]. The magnitude of the change in the device characteristics is dependent on the density of trapped charge on to the floating gate layer [56]. The trapped charge can also be removed from the floating gate using a reverse bias on the gate potential which returns the device to its original electrical

characteristics. This mechanism is the principle of write/erase operation in flash semiconductor memories.

There are two different tunneling mechanisms responsible for the charge transfer to and from the floating gate in the FGMOS devices. One mechanism is based on Fowler Nordheim (FN) tunnelling [61]–[63]. The energy band diagram of the FGMOS is shown in Fig. 2.2 demonstrating the gate oxide tunneling effect when large control gate voltages are applied [57]. The Fowler Nordheim tunneling mechanism is a field dependent tunneling phenomenon that can occur when a large electric field is generated across the gate oxide with the application of a very high gate voltage. When the control gate terminal (*poly2* layer) is kept at a positive potential with respect to substrate, the generated electric field excites an accumulation of minority charge carriers (electrons) from the substrate close to the oxide substrate interface. For very high electric fields, some of these electrons from conduction band of the substrate may acquire enough energy to tunnel through the triangular portion of the potential barrier of thin gate oxide layer. The thick inter layer dielectric (ILD2) represents a large potential barrier for these electrons to travel through to the control gate and as such the tunnelled electrons become trapped on the floating gate layer of *poly1*.

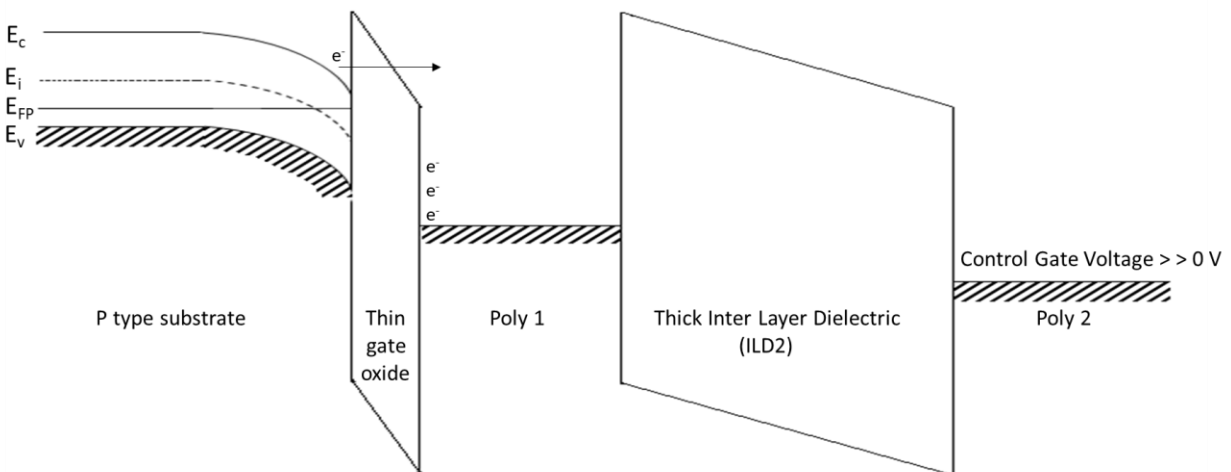


Fig. 2.2 Energy Band diagram of n type FGMOS at Fowler Nordheim tunneling

The trapped charge of the floating gate also produces an image charge at the oxide/semiconductor interface which results in a lowering of barrier height [64]. Due to this trapped charge, a shift in the normal FGMOS electrical characteristics is observed. The process of removal of charge also results from the FN tunneling mechanism where a large reverse gate potential excites the trapped electrons to tunnel through the thin oxide barrier back to the substrate.

For the sensor application of this work, a modification in the basic structure of the FGMOS transistor was required to allow easy accessibility to the floating gate terminal [65][55]. Usually, the floating gate *poly1* layer is buried under the ILD2 layer, the control gate *poly2* layer and all of the 4 metal and inter-dielectric layers. To create an electrical connection to the *poly1* layer, a series of complicated and difficult selective etching steps would be required on the already fabricated chips. To avoid these difficult post processing steps, the FGMOS structure was designed with an electrical extension of the floating gate layer connected to the topmost metal layer (M4). A 3D representation of the FGMOS sensor structure is shown in Fig 2.3.

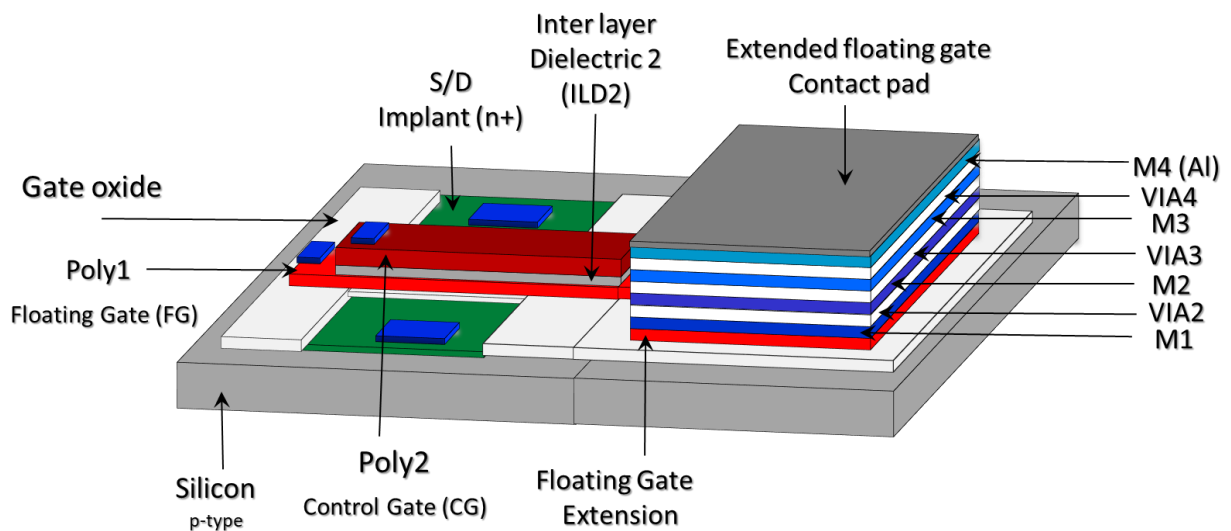


Fig. 2.3 An extended floating gate design for n type FGMOS sensor

The top metal layer (M4) from the *cmosp35* technology was used as an extension to the floating gate *poly1* layer of the sensor. To create the floating gate layer connectivity to the topmost metal layer, a stacked structure was created that connected all of the intermediate metal and via layers. For example, M1 was connected to the floating gate using a “contact” hole through the first inter-layer-dielectric (ILD). M2 was then connected to M1 through a “VIA1” hole in the second ILD2 layer and so on through to M4. The floating gate extension is the surface onto which the conducting polymers were electrochemically deposited, effectively functionalizing the active sensing area these devices. Unfortunately, all metal layers in the *cmosp35* technology are made mostly from aluminum, which oxidizes and inhibits the electrodeposition of the polymers. To overcome this problem, a layer of gold was selectively electrodeposited onto the floating gate extensions using several post processing steps. In a cleanroom environment, a process for the selective electroless deposition of gold onto the aluminium extensions was developed. The now gold coated surface of the floating gate extensions was used as the working electrode for the electrodeposition of the desired conducting polymers. A diagrammatic representation of the

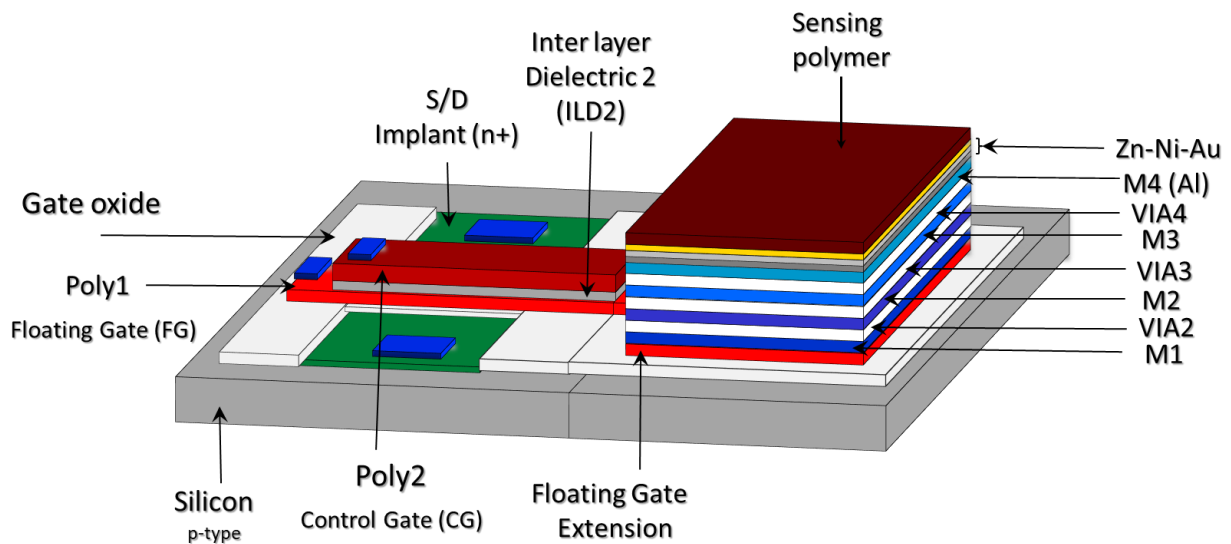


Fig. 2.4 An extended floating gate design of the FGMOS sensor functionalized using a sensing polymer

FGMOS sensor functionalized with the sensing polymer is shown in Fig. 2.4. After successfully depositing the polymers onto the extensions, characterization of the sensor system was conducted in a controlled electrical and analyte environment.

The operation of the FGMOS sensor is dependent upon the applied electrical bias to the gates, source, drain and substrate terminals, as well as any charge that has been induced onto the floating gate when the conducting polymers on extensions interact with an analyte vapor. In Fig. 2.5, a schematic of the typical electrical bias setup used for testing the FGMOS sensors is shown. A scenario representing the interaction of different analytes with the conducting polymer causing a change in sensor current is also shown. The FGMOS sensor is biased with a positive (with respect to the source and substrate) DC bias applied to the drain and control gate terminals, V_{DS} and V_{CG} , respectively. Under these bias conditions, a constant drain current of I_{DS0} flows through the sensor as shown schematically in Fig. 2.5. Each of the conducting polymers responds

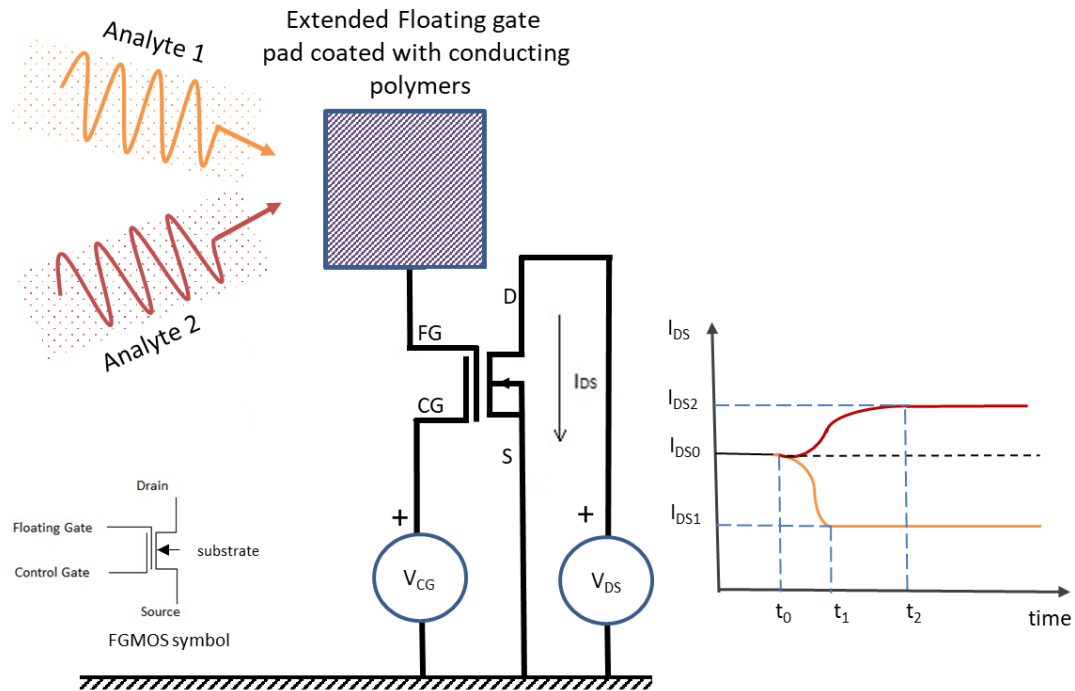


Fig. 2.5 Schematic representation of FGMOS bias setup and expected change in sensor current on exposure to different vapor analytes

in a unique way to the different vapour analytes. A figurative example of the anticipated time dependence of the drain current (I_{DS}) is shown in Fig. 2.5, demonstrating the change in sensor current (I_{DS0}) when an analyte vapour interacts with the polymer film. Depending on the type of interaction, the variation in drain current can be positive (increasing) or negative (decreasing) as demonstrated in Fig. 2.5. Two different scenarios are presented where the initial drain current of I_{DS0} decreased to I_{DS1} or increased to I_{DS2} . The response time of the sensor is also dependent on the sensitivity of an individual polymer reaction to a specific vapour analyte.

The electrical operation of a sensor resembles a typical nMOS transistor when operated using any one of the gate terminals. The drain current (I_{DS}) flowing through a nMOS transistor biased in the subthreshold region of operation can be given as [66],

$$I_{DS} = \mu_n C_{ox} \cdot \frac{W}{L} [(V_{GS} - V_{THN}) V_{DS} - \frac{V_{DS}^2}{2}] \quad (2.1)$$

where, μ_n is the average electron mobility through the channel, C_{ox} is the gate oxide capacitance, W is the width and L is the length of the channel. The transistor, having a threshold voltage of V_{THN} , is biased using a gate voltage of V_{GS} and drain voltage of V_{DS} with respect to the source and the substrate. The channel width to length ratio, $\frac{W}{L}$, with all the other parameters of the given Eqn. (2.1) is kept constant and has a linear relationship with the I_{DS} . Different $\frac{W}{L}$ ratio of the sensors in an array will introduce unique amplification factors in the I_{DS} for a given electrical biasing setup. For the sensor array in this work, sensors having multiple different $\frac{W}{L}$ ratios were designed and characterized. The idea was to use the $\frac{W}{L}$ multiplication factors of the sensors to amplify the sensor responses in cases where an analyte interaction causes a very small change in the sensor response. The most recent iteration of the chip had sensors with a fixed gate length of 1 μm and the width of sensors was kept as a variable at 10 μm , 20 μm , 30 μm and 40 μm . A comparative plot of the

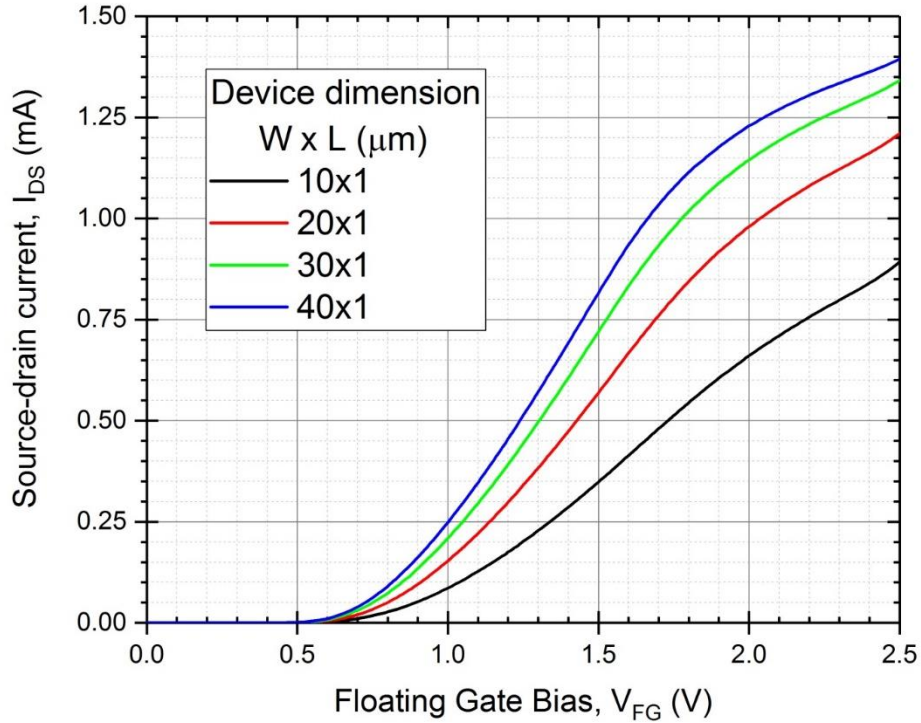


Fig. 2.6 Transfer characteristic of the FGMOS sensors having different $\frac{W}{L}$ ratios

transfer characteristics for the sensors having different $\frac{W}{L}$ ratios is shown in Fig.2.6. The sensors were biased at a constant V_{DS} of 1V and the V_{FG} potential was applied with a voltage sweep. It can be observed that for a given gate potential, the sensor current scales with the $\frac{W}{L}$ ratio.

The basic feasibility of this type of sensor idea had been verified in the work of a previous graduate student [55]. However, to develop a chemically diverse olfactory sensor system, a new chip, having an array of FGMOS sensors and the required electronic circuits, needed to be integrated onto a single silicon substrate. The chip was designed using the Cadence integrated circuit electronic design automation tools using the TSMC *cmosp35* technology parameters. These chips were fabricated using the multiple project wafer (MPW) prototyping services offered by TSMC and availed through the CMC Microsystems. A Cadence Virtuoso layout view of one of the recent iterations of the designed chip is shown in Fig.2.7. The given chip contains, arrays of

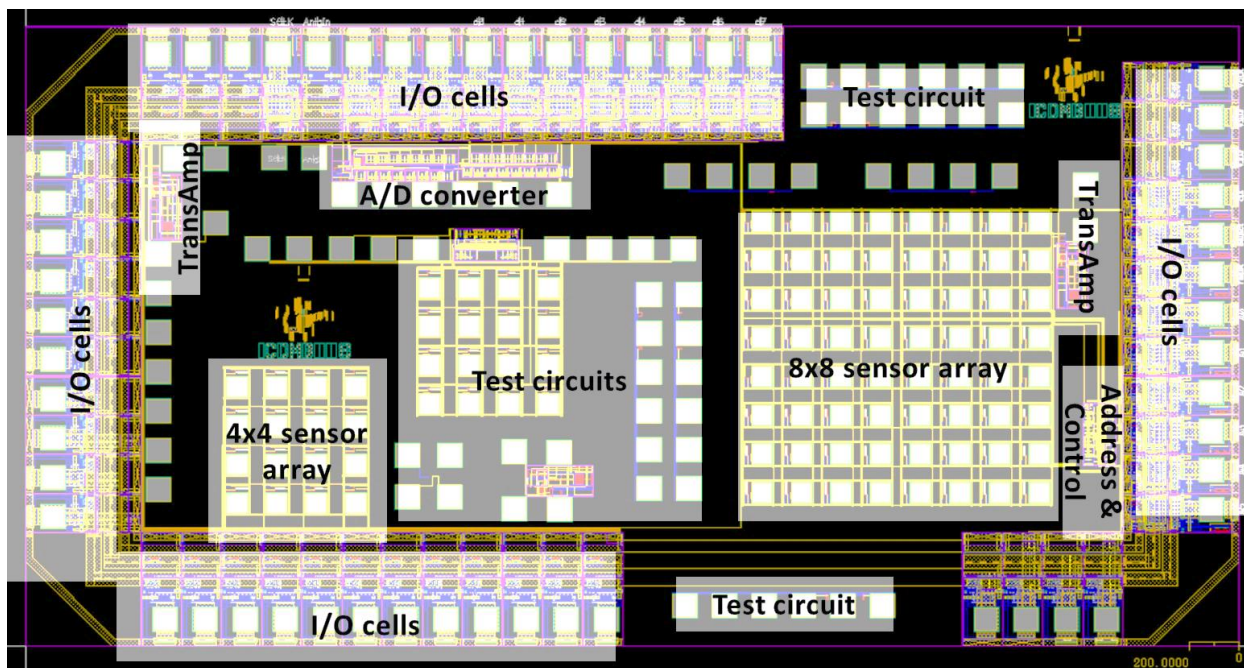


Fig. 2.7 Cadence virtuoso layout view of the Chip (scale in micrometer)

sensors (4x4 and 8x8) where each individual sensor is accessible using a specially designed addressing circuit, transimpedance amplifier (TransAmp), an analog to digital converter (A/D), the input/output (I/O) cells for enabling external access to the given circuits and multiple other devices and circuits under tests. The blocks indicated as test circuits included the new designs or optimized version of some of the existing circuits. These were the circuits under consideration to be included in the system for the next iteration to improve in the system performance. Test circuits were first electrically characterized using the semiconductor probing station. After successful performance analysis, the test circuits were employed in the array system designs and were connected to the input/output (I/O) cells of the chip. The I/O cells were wire bonded to the chip package which enabled the connections to the external electrical equipment.

Of the two arrays of sensors on the chip, one of the 4x4 arrays was designed to monitor the sensor current variations upon exposure to analytes and was not connected to other

sensor current processing circuits. This array had a structure of row and column buses that were designed to gain controlled electrical access to the sensors through the analog buffer circuits. The addresses for the 4x4 sensor array were generated by applying suitable electric potentials to the row and column bus terminals connected to the external electrical circuits through the I/O cells. The 8x8 sensor array was accessed using a specially designed address and control circuit. This array was integrated with the other on-chip processing circuits to develop a complete olfactory sensor system. A schematic diagram of this olfactory sensor system using an 8x8 array of sensors is shown in Fig. 2.8. The change in the electrical response of a sensor, upon interaction with different vapour analytes, can be very small and range from a few picoamperes (pA) to 10's of microamperes (μA); some 6-7 orders of magnitude. To accommodate this large “exponential” change in current, a novel logarithmic transimpedance amplifier was designed, the linear voltage output of which was then converted to an 8-bit digital signal using the A/D converter to produce a digital output. Multiple iterations of the chip were useful to do the functional verification of the addressing, amplifying and conversion circuits. These results were used to develop an optimized

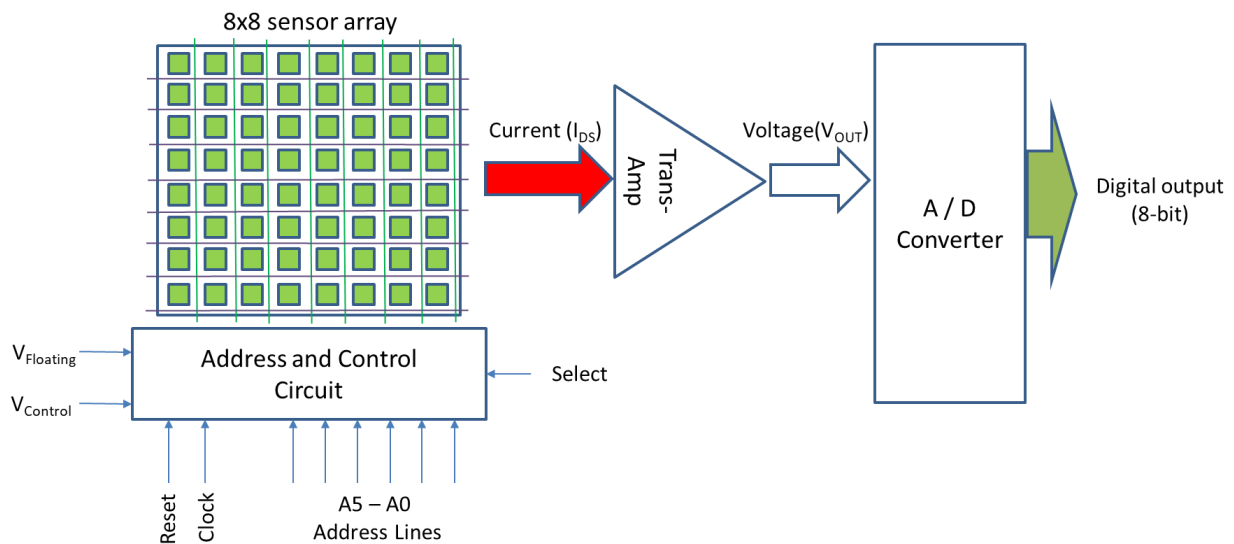


Fig. 2.8 A block schematic for the designed Olfactory Sensor system chip

version of the system. The designs of different circuits used in this system are explained in the next section.

2.2 Address and Control circuits

The sensors in the array required suitable electrical signals to bias them in a favourable operating region. Access to each extended floating gate sensor pad individually was required for the selective electrodeposition of the polymers. An automated addressing scheme would be very convenient for system testing. To meet these requirements a special address and control circuit was designed using counters, multiplexers, decoders and analog buffers as shown

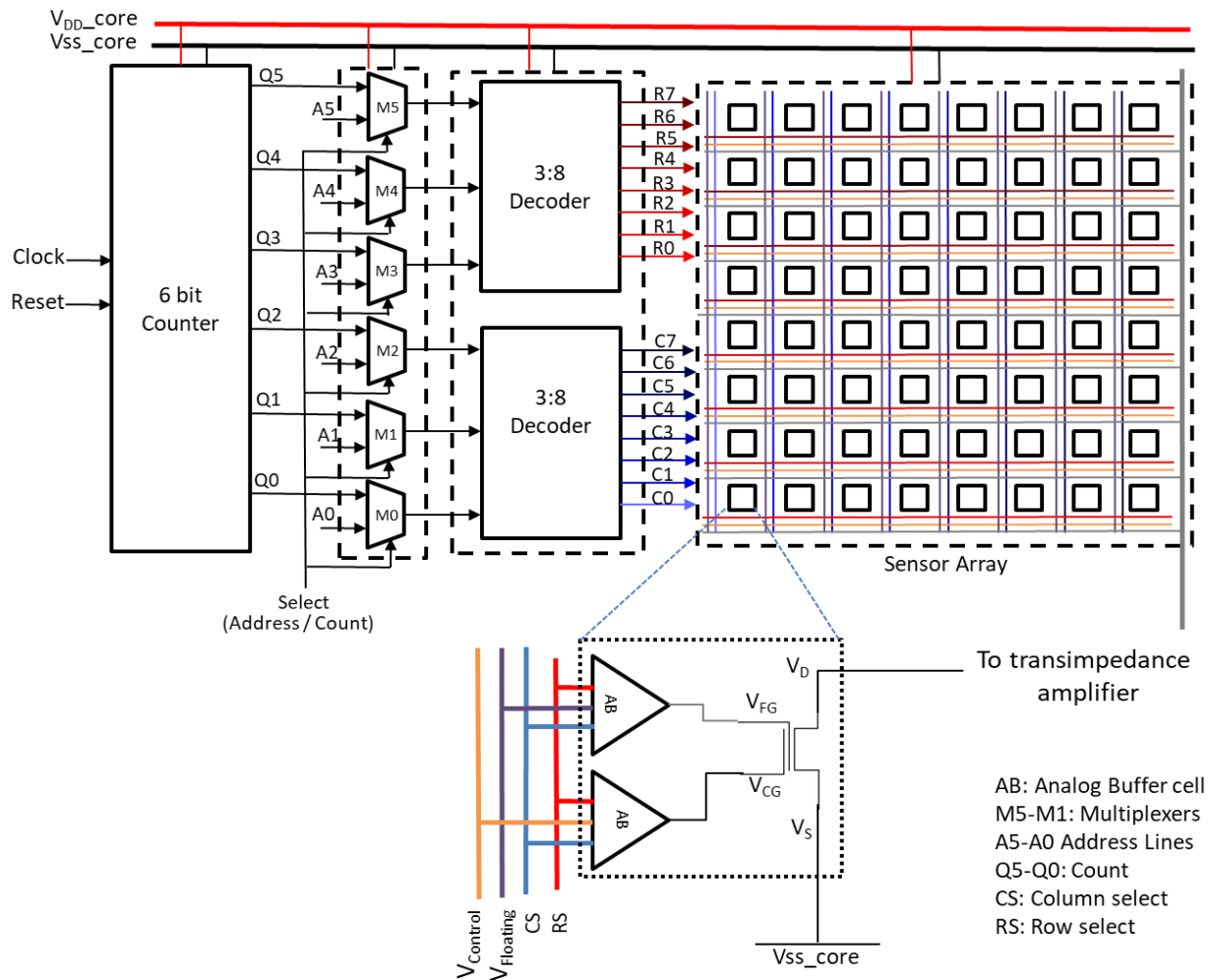


Fig. 2.9 The address and control signal generation logic for 8 x 8 sensor array

in Fig. 2.9. All of the circuits were designed using the Cadence Virtuoso schematic composer tool. The address and control circuit has two operational modes. One where the sensors in the array can be addressed manually using the address lines A5-A0 to generate a 6-bit address for all 64 sensors. In the automated mode of address generation, a clock signal was used to trigger the 6-bit counter circuit which counts through all addresses automatically. An array of six multiplexer circuits was used to switch in-between these two modes. The 6-bit address generated by the counter was used to control 8 rows and 8 columns buses that run through the array of sensors. The signals for these row and column buses were generated by decoding a 3-bit address signal to 8-bit using two 3:8 decoder circuits. Every one of the row and column bus combinations was used to excite an individual array cell which has one FGMOS sensor, digital gates and two specially designed analog buffer circuits.

The array cell with analog buffer circuits used to transmit the floating gate and control gate voltages to the FGMOS sensor of the cell are shown in Fig. 2.10. The digital AND gate uses inputs from the row and column select bus to generate an output which is used to enable

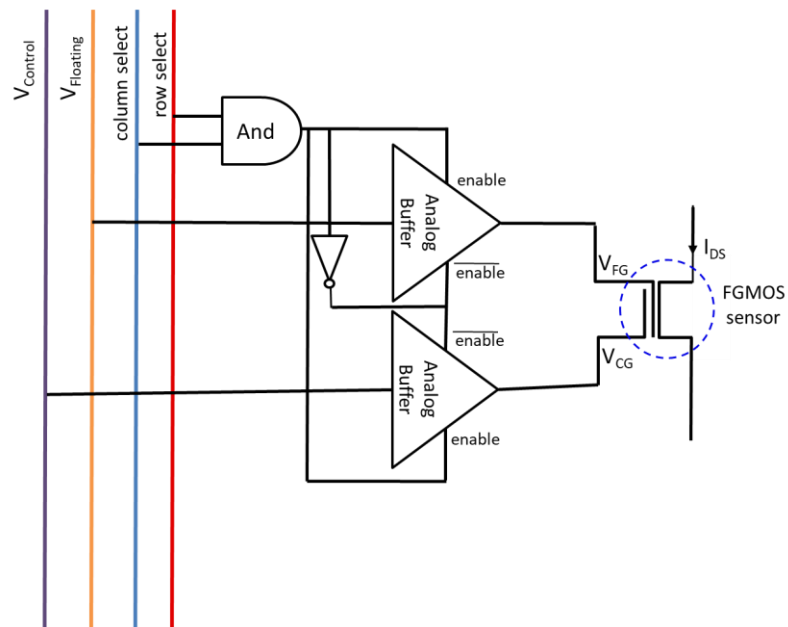


Fig. 2.10 Schematic representing FGMOS addressing scheme in an array cell

the analog buffer circuits. An ON-state buffer connects the gate terminals of the FGMOS sensor to external pins which were used to pass electrical signals for the polymer electrodeposition or analyte detection process. A Cadence Virtuoso layout view, showing the design of the array cell structure, is given in Fig. 2.11. The given layout view shows two different sizes (W/L) of the FGMOS sensors, W/L ratios of 10:1 and 20:1, connected to individual array cells. The array cell is surrounded by multiple parallel metal lines functioning as buses for different electrical signals. Different metal levels, from the four-metal stack of the *cmosp35* technology, were used to create a horizontal and vertical signal bus structure as observed in the different colors of the bus lines in the given layout view. The floating gate terminal was normally left electrically open and was biased only during the process of electrodeposition of the polymers. The drain current of sensors was controlled with a suitable control gate bias. The sensor current was fed into a transimpedance amplifier to convert the exponential change of the sensor current to linear output voltages.

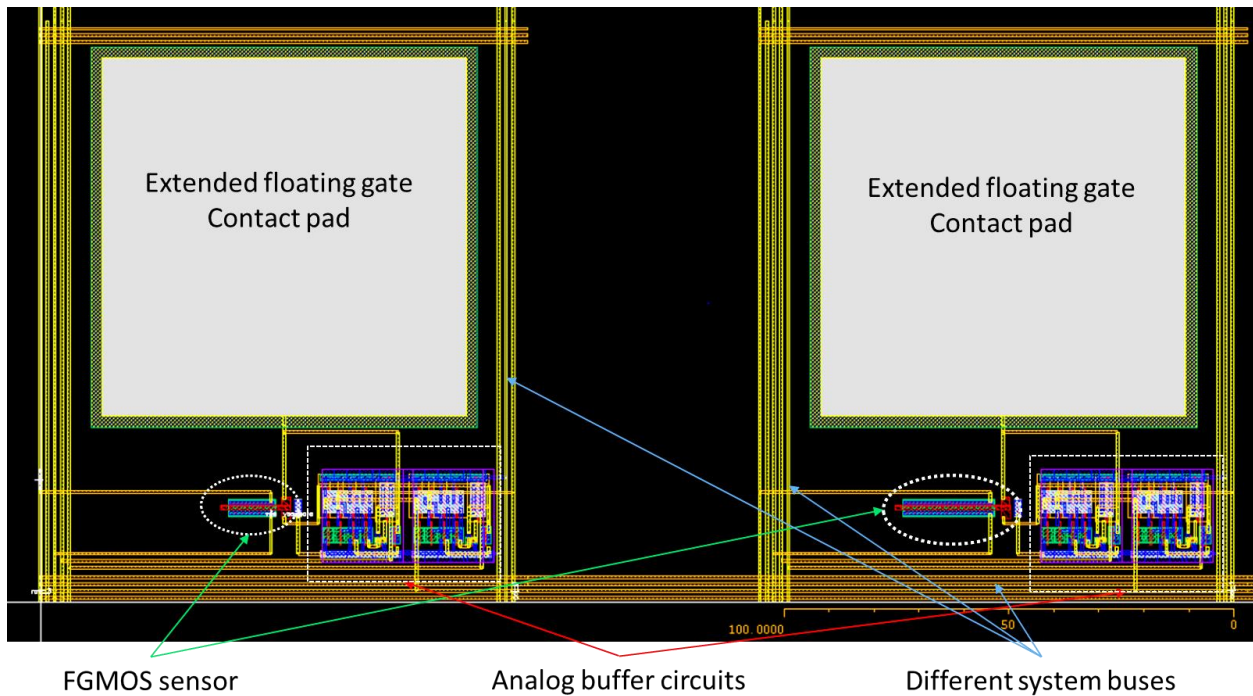


Fig. 2.11 Cadence virtuoso layout view of the array cells (scale in micrometer)

2.3 Transimpedance Amplifier

To create the greatest sensitivity, the FGMOS sensors should be biased in the subthreshold or weak inversion region of operation where a slight change in the floating gate voltage produces a substantial change in sensor drain current. For a linear change in the control gate voltage, the drain current changes exponentially and its magnitude can range from a few nanoamperes (nA) to microamperes (μA). To rescale this exponential response onto a linear voltage scale, a transimpedance amplifier circuit was designed. A schematic of this circuit is shown in Fig. 2.12.

The first stage for the transimpedance amplifier circuits is a logarithmic amplifier which converts the exponential input current to a linear output voltage. However, the voltage at the output of the first stage is low, inverted and not scaled to the supply voltage limits. The amplifier should have maximum possible output voltage swing within the supply limits, from 0-3.3 V. To achieve output voltage swing, two high gain operational amplifier stages were added to rescale the output voltage from the first stage. The first stage of this amplifier had an inverting

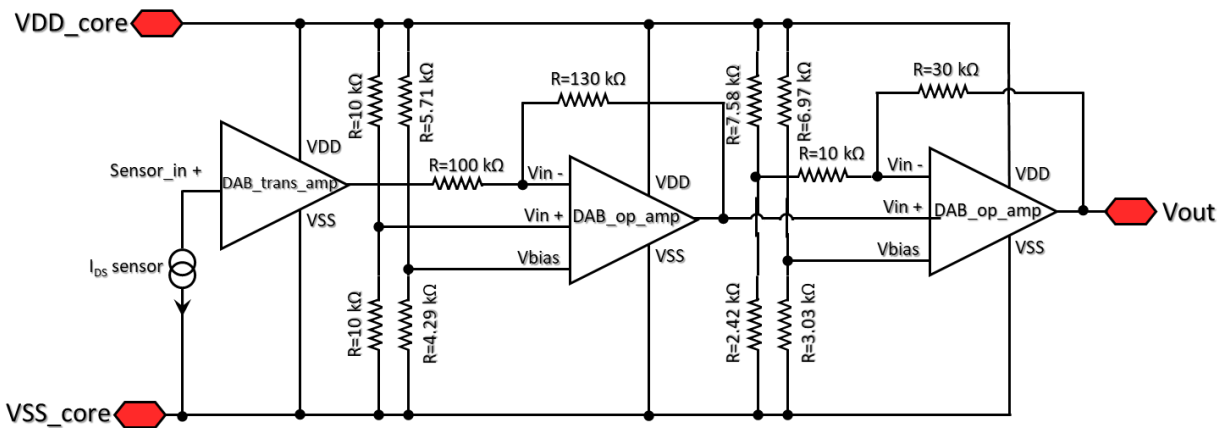


Fig. 2.12 A schematic diagram for the transimpedance amplifier circuit (the annotations inside the amplifier blocks indicates the names used for the cadence schematic circuits)

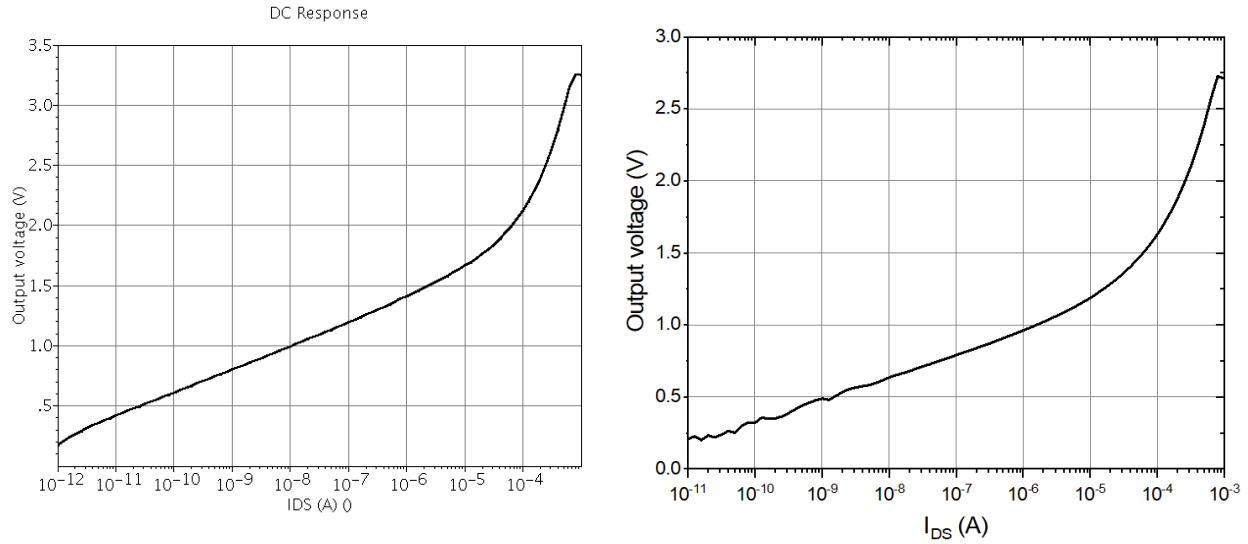


Fig. 2.13 (a) Simulated electrical response (b) actual electrical characteristics of the transimpedance amplifier

mode of operation. The gain of these stages was designed to achieve linear output voltage swing of around 90% of the supply voltage. The transimpedance amplifier output voltage from cadence simulation is shown in Fig.2.13(a) and from the characterization of an on-chip circuit in the Fig.2.13(b). The simulation result shows that for input current change from 1pA to 1mA, the transimpedance amplifier would be able to produce a wide voltage swing from 200 mV to 3.2 V which slightly less than the voltage limits, 0-3.3 V. The sensor drain current, in the subthreshold regime of operation, was observed to be in the range of tens of microampere. The transimpedance amplifier was designed considering that the subthreshold regime current range to be biased at the midpoint of the amplifier operation. This was to ensure optimal tracking of the bidirectional changes of the sensor current. The electrical characteristic of the on-chip transimpedance amplifier was observed to follow the simulated response (0-3.3V) although it had a slightly reduced range (0.2 - 2.8V) of operation. This effect was due to the contact resistances introduced in the circuit from the measurement setup and any possible process variations during the manufacturing of the chips. During initial testing of one of the previous designs on earlier iterations of the chip, a loading

effect of the transimpedance amplifier on the sensor current was discovered. To overcome this problem, a current mirror circuit was added in-between the sensor and transimpedance amplifier which removed the direct connection between the sensor and the amplifier and resulted in a more stable operation.

2.4 Analog to Digital converter

The final stage of this sensor array system is an analog to digital (A/D) converter designed to produce an 8-bit digital result from the amplifier output. The 8-bit A/D converter yields a voltage resolution of 13 mV ($3.3 \text{ V} / 2^8$) which means the sensor can discriminate (a 1-bit change) between voltages having a difference of more than 13 mV. The digital data from the entire array, given that each of the sensors could contain a different polymer and therefore react differently to a given group of analytes, can collectively produce a “digital” fingerprint or 2D “image” for a given analyte. The digital information is easier to store and process. Therefore, the A/D converter is an important circuit on the chip which is expected to decrease the complexities in the development of processing algorithms by representing information in more convenient digital form. A block schematic for the A/D converter implemented on-chip is shown in Fig. 2.14.

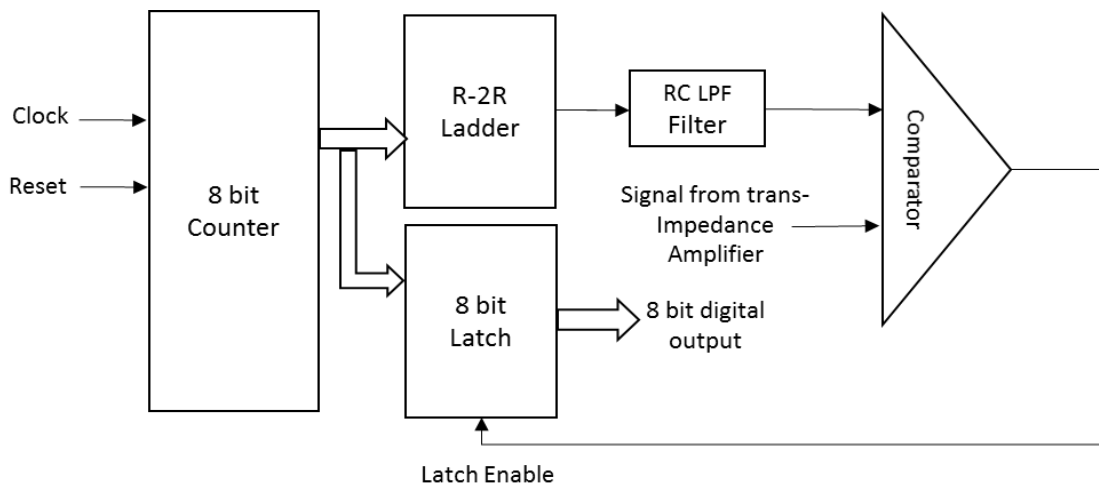


Fig. 2.14 Block schematic representation of the analog to digital converter

The 8-bit counter is synchronized to the clock signal which is incremented on the positive edge of the clock. The output bus of the counter is connected to an R-2R ladder circuit which converts the 8-bit binary number generated by the counter to its equivalent voltage level. For a counter counting up, the R-2R circuit will generate a ramp signal of voltages for every cycle of the count. The analog ramp signal generated with R-2R circuit has high frequency components from the clock superimposed on the voltage ramp. To minimize these high frequency components and its effect on circuit operation, a low pass filter is used between the R-2R ladder circuit and the comparator. The filtered voltage ramp signal is then compared with the output voltage of the trans-impedance amplifier using a comparator circuit. Once the ramp signal voltage exceeds the trans-impedance amplifier output, the comparator generates a trigger signal which is used as a latch enable control signal for an 8-bit latch circuit which stores the data. Hence an 8-bit digital number, equivalent to the voltage generated by trans-impedance amplifier output is latched at the output of the A/D converter.

Several simulations were performed to evaluate the performance of the A/D converter circuit. The simulation results showed good linearity between the analog input and the digital output of the A/D converter. The primary limitation of the A/D converter was the long response time as it could require it to run through all possible 256 digital states (i.e. 256 clock cycles) to find a match with the input signal. The response time of the polymers to detect the presence of any vapour analyte is usually much longer than this response time (256/clock), therefore this A/D circuit was considered suitable for this application. However, when an operational circuit of the given A/D converter was tested on one of the earlier iterations of the chip, the A/D converter was observed to produce a high level of noise on the digital output lines. The observed noise was in phase with the clock signal to the counter and was observed to couple with

the operating signals of other circuits and cause instability of the system operation. This issue required optimization of the low pass filter circuit of the A/D converter which was completed and added to the circuit.

Considering the sensitive nature of the application, the A/D converter on the chip was replaced with a new Flash-type A/D converter. This design was simple, fast and did not require a high frequency clock signal for its operation. The given flash type A/D converter circuit was built around a priority encoder design. This A/D converter has a bank of series connected resistances applied with the supply voltage at the ends of the series connections. The resistance bank is used as a potential divider network of the supply voltage and the taps of resistance connections are used to generate weighted reference points for voltage comparison. In the next stage, a bank of comparators is used that compares the given weighted tap potentials to the analog input voltage. The comparator bank outputs are used to drive a priority encoder circuit (2^n lines to n lines). The priority encoder circuit has a priority for the highest active input line and produces an n -bit digital output based on the highest successful active comparison operation. A schematic of a 3-bit prototype for the flash type A/D converter is given in the Fig. 2.15. This schematic represents the methodology used for the design of the given 8-bit A/D converter. The enable (en), group select (gs) and output enable (oe) signals of the priority encoder are very important for cascading and design of a higher order priority encoder.

For the given A/D converter circuit, a resistor bank of 2^8 (256) series connected resistors was designed and supply voltage, 0-3.3V, was applied to the bank terminals. The tap points of the series connected resistors were used to drive an equal number of comparator circuits where these potential values were compared with the analog input voltage. A 256-line to 8-line priority encoder circuit was designed. The outputs of the comparator bank were used to drive the

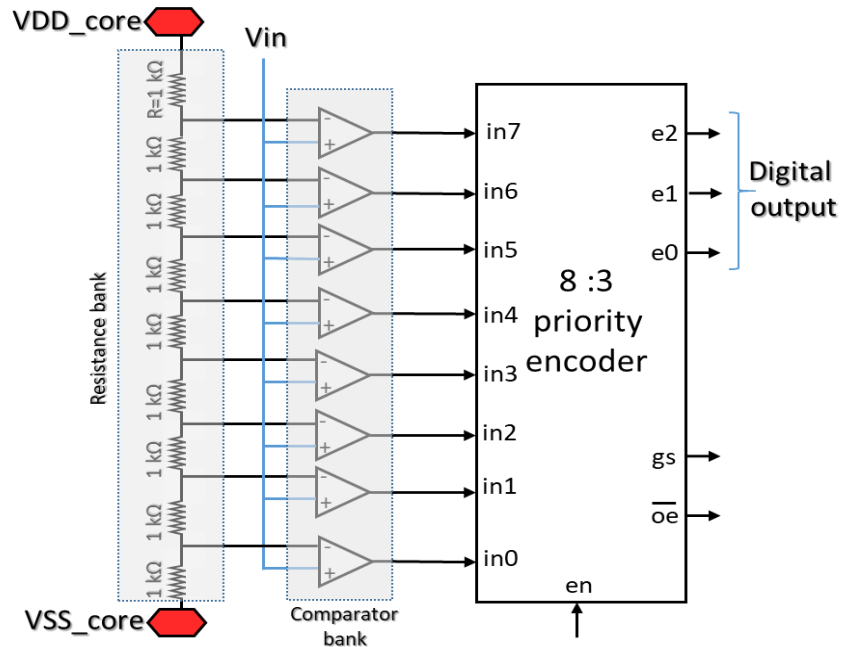


Fig. 2.15 Block schematic representation of a 3-bit flash type analog to digital converter

designed priority encoder circuit and the digital 8-bit output was produced at the output lines of the encoder. A priority encoder circuit with the given large number of input lines has a very complex design. The design complexity was handled by first designing an 8-line to 3-line priority encoder circuit and then cascading multiple such encoder stages to get the desired large size of the given encoder circuit.

The chips from multiple different fabrication runs were tested for electrical performance of this system. The information from these characterization results was used to redesign the sensor and some of the circuits to achieve a more optimized system response. The circuits present on the present iteration of the chip worked to the design specification. The next task was to post process the chips for selective electrodeposition of the polymers and design setups for the post processing and analyte testing experiments. These details are discussed in the following chapters.

Chapter 3 – Post processing and Polymer deposition

Under ideal circumstances, the integration of the polymers with the extended floating gate pad of the sensor should require only one process of electrodeposition of a given polymer. However, past experiences were that the polymers do not deposit well on the as-received aluminum surface of extended floating gate pads. In fact, it was observed that instead of polymer deposition, an etching of the aluminium layer was observed [56]. An ideal solution is to coat the surface of extended floating gate pads with some non-oxidizing, non-reactive noble metal. Gold (Au) is often used in a thin form for the deposition of organic polymers using the electrochemical process [67]. It was believed and subsequently discovered that gold would be a suitable metal to work with these chips.

The process of selective deposition of gold onto the contact pad surface using a standard lithography technique would be difficult to perform due to the size of this silicon chip (~3×4mm). Coating the contact pad surface using electroplating is promising but the conventional electroplating process would require a series of electrical connections which would be very complex. An electroless deposition technique for plating has been shown to be an easy and reproducible process with the compatibility of electrodeposition on a micron scale [68]. The electroless plating process simply requires only an aqueous solution of the target material and works without the need of any external electrical connections. The aqueous solution used for electroless plating contains a reducing agent for the target material which triggers a chemical reaction when the substrate electrode is immersed into the solution, resulting in the reduction of target material onto the substrate, effectively coating it.

3.1 Electroless Gold Plating

Aluminium is very reactive to the presence of oxygen and forms a thin native oxide layer on its surface soon after it comes in contact with any oxygen environment. This native oxide layer prevents direct contact with the aluminium surface which makes the electroplating of gold onto the aluminium contact pads very difficult. A well-known industrial solution to this problem includes a three-stage plating process for electroplating gold on an aluminum surface. The process requires sequential plating of zinc, nickel and then gold layers onto a clean aluminium surface. Some researchers [68] have reported that this process is compatible with microelectronics applications.

Before the plating process has begun, it is very important to clean the surface of the chips to ensure a homogenous deposition. The chips were rinsed thoroughly in organic solvents (methanol and acetone) followed by a deionised water rinse to remove any organic contaminants. The chips were then immersed into a room temperature aqueous solution of “Zincate” a zinc compound from Casewell Inc. The zincate solution first etches the thin aluminium oxide layer present on the surface and immediately follows it up with the deposition of zinc onto the surface which prevents re-oxidation of the aluminium until the next plating process is initiated. The zincate solution is alkaline in nature and can generate complex intermetallic compounds of aluminium which are found to be insoluble in the zincate solution [69]. These insoluble compounds are known as ‘smut’ which can adversely affect the uniformity of the following electroplated layers. To achieve uniformly electroplated surfaces, a process of “desmutting” with a dilute nitric acid solution followed by one more zincate bath is required. This combined process is called as a double zincate process. Desmutting after first zinc bath helps in stripping of undesired smut and nucleated zinc depositions onto the surface of aluminium which helps achieve a homogenous, thin zinc layer

on the aluminium surface [69]. The presence of zinc layer on top of the aluminium surface was confirmed with optical microscope images and energy dispersive x-ray spectroscopy (EDS) using a FEI Quanta 650 scanning electron microscope available through the Manitoba Institute of Materials at the University of Manitoba. The zinc coated samples were processed for electroless nickel growth using another plating solution purchased from Casewell Inc.

The nickel bath requires a proportionate mixing of three nickel concentrates to prepare the final plating solution. The electroless deposition of nickel is an autocatalytic process where the product of an initial chemical reaction act as the catalyst for the next chemical reactions. The process required a bath temperature of 90°C to trigger the autocatalytic process. When the zincated samples were immersed in the heated nickel bath, uniform deposition of nickel onto the zinc at the plating rate of 400 nm/minute instigates.

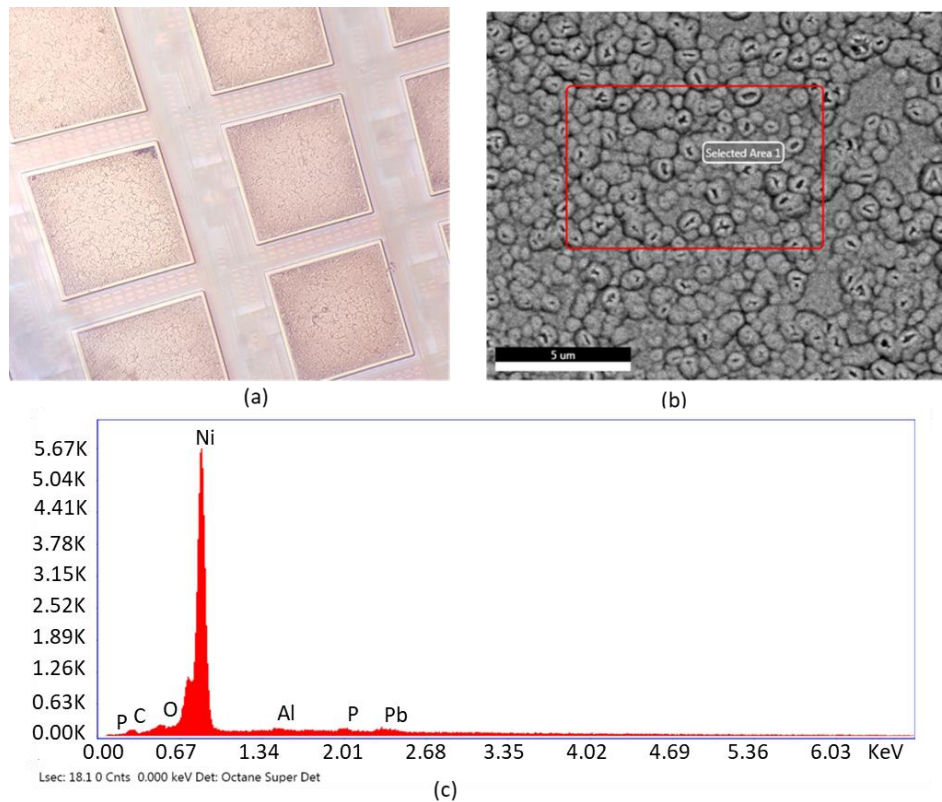


Fig. 3.1 (a) Nickel coated extended floating gate pads (b) SEM image for nickel surface and (c) EDS analysis for the surface to confirm presence of nickel layer

The thickness of the plated nickel layer was controlled using the immersion time of the samples in the heated nickel bath. An immersion time of 75 seconds with constant agitation of 100 rpm should give approximately a 500 nm thick nickel layer. To confirm the successful deposition of uniform nickel films on the extended floating gate pad surface, optical microscope images were taken. A uniform metallic appearance of the surface, as seen in Fig. 3.1 (a), was observed to be different from the previously deposited zincate layer. The color of the aluminum surface was very similar to the observed layer which raised some concern whether the zincate surface was coated with nickel or etched away in nickel bath exposing underlying aluminium layer. The EDS was then used on a selected area of the electroplated surface as shown in Fig. 3.1 (b). The element composition map (Fig. 3.1(c)) showed that nickel was the primary component on the surface of extended floating gate pads. The final process in this sequence was the electroless gold deposition as described below.

A cyanide free immersion gold solution was ordered from Transene Company Inc., Canada. The process required a bath temperature of 75°C to initiate electroless gold depositions which had a typical deposition rate of ~25 nm/minute. This solution was agitated at 100 rpm to ensure uniform depositions. The nickel coated samples were immersed in the heated gold bath for 2 minutes. A bright gold appearance of extended floating gate pads surface was easily visible using the microscope and was again verified using the EDS analysis. The electroless plating technique gave an easy and efficient process of producing a gold coated surface for the extended floating gate pads. The next stage was the electrodeposition of the polymers onto these gold coated surfaces. For simplicity, the initial polymer deposition experiments were limited to polypyrrole films. The details of the polypyrrole electrodeposition are given in Section 3.2 below.

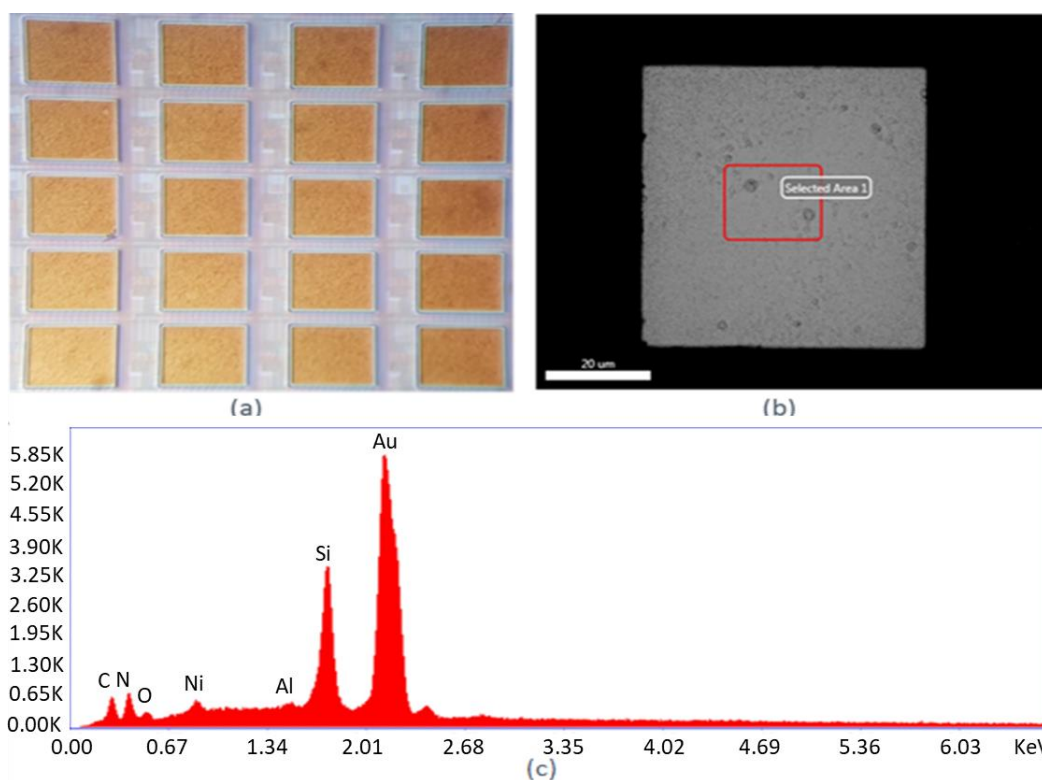


Fig. 3.2 (a) Gold coated extended floating gate pads (b) SEM image for gold surface and (c) EDS analysis for the surface to confirm presence of gold layer

3.2 Electrodeposition setup

The chemicals used in this work includes monomer compounds of pyrrole, aniline and styrene. These monomers and other dopant compounds which includes p-toluenesulfonic acid (pTSA), tetrabutylammonium tetrafluoroborate (Bu_4NBF_4), sodium dodecyl sulphate (SDS) and oxalic acid ($\text{C}_2\text{H}_2\text{O}_4$) were ordered from Sigma-Aldrich. All other chemicals mentioned in this work were availed from the inventory of Nano-Systems Fabrication Laboratory (NSFL), University of Manitoba. The purchased chemicals were analytical grade and were used as received. The platinum (Pt) and the silver/silver chloride (Ag/AgCl) electrodes were purchased from CH Instruments, Inc.

For the process of electrodeposition of the conducting polymers, a three-electrode electrochemical cell was used. In this cell, a platinum electrode was used as the counter electrode,

a silver-silver chloride (Ag/AgCl) electrode as the reference electrode and the surface to be electroplated acted as the working electrode. Every electrode potential was measured with respect to the standard potential of the Ag/AgCl reference electrode. The process of electromigration occurs in-between working and counter electrode where the working electrode acts as a site for the Oxidation-Reduction (Redox) reactions for polymer deposition. The counter electrode acted as the source or sink of the charge carriers [70]. Redox potentials for the polymer depositions were selected from the analysis of the cyclic voltammetry experiments where working electrode potential was ramped linearly in time while the current was measured. The initial electrodeposition experiments were performed using large (~3mm x 8mm) interdigitated electrodes (IDE) as the working electrodes. Any electrodeposition of polymer onto these electrodes was visible without the requirement of using a microscope. The experiments were useful to analyse different useful parameters of the electrodeposition process such as the electrode current, time required for electrodepositions and any adverse reaction of the electrolytic solution to the working electrode surface. The findings of these experiments were very useful to setup the electrodeposition process for the much smaller sized electrodes on the chip.

The electrolytic solutions used in the electrodeposition of polymer films were prepared by adding the monomer and the dopant compounds into a solvent. Twenty, 20 ml of the solvent was used for all the electrodeposition experiments. This volume was used for calculation of the desired concentrations of the monomer and dopant compounds. A breakout board mounted with an appropriate 69 pin PGA (Pin grid array) socket was used for setting up the packaged chip connections to different electrical instruments. The breakout board is a printed circuit board that breaks out electrical connections from the chip socket pins to the multiple pin connectors for the ease of making electrical connections. The complete electrical assembly was bulky, and it was not

feasible to exclusively immerse the chip into the electrodeposition solution without exposing the other components of this assembly to the given electrolytic solution. Different salts and acids were used as dopants for the preparation of these solutions. These chemical compounds are known to cause corrosion of conductors and can cause degradation of other materials of the assembly. A special setup was designed to ensure that only the silicon chip inside the package cavity was immersed into the electrolytic deposition solution.

The designed setup was a mechanical clamp arrangement which held a syringe barrel on top of the chip to act as a container of the electrolytic solution. The plunger of a 25 ml syringe was removed, and an O-ring was carefully glued to the flange of the syringe barrel. The top of the syringe barrel was carefully cut just below the needle adapter to create a bigger opening to insert the electrodes. The breakout board with a chip mounted on the socket was placed on the mechanical clamp setup and the syringe barrel was clamped to the upper surface of the chip package. The barrel flange acted as mechanical support to push the barrel against the chip package. The O-rings effectively made a sealed contact and the clamp was tightened using nut and bolt

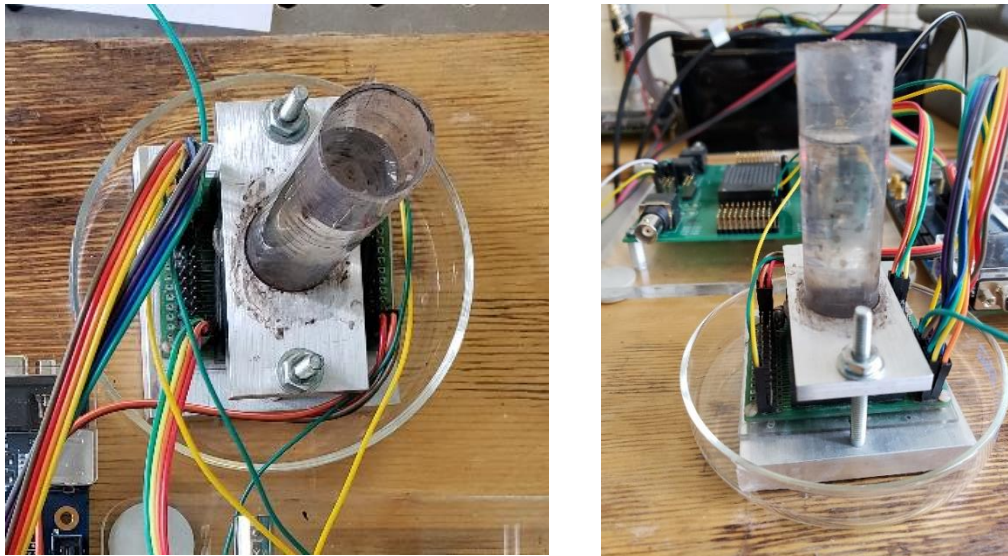


Fig. 3.3 Mechanical clamp setup used for the electrodeposition process

arrangement. A picture of the designed setup is shown in Fig. 3.3. The syringe material, polypropylene, is resistant to many different chemicals. This ensured an inert environment for holding the electrolyte during the deposition process. The clamp arrangement was easy to setup and remove which helped to reduce the effort required for changing the electrolytes and cleaning the chip in-between electrodepositions using different chemical recipes.

3.3 Selective encapsulation and electrochemical cell setup

The chips packaged in the CPGA 69 (Ceramic Pin Grid Array) packages had Au bond wires which were to connect the electrical terminals from the chip to external pins of the package. The bond wires used are very delicate ($\sim 25 \mu\text{m}$ diameter) and require very careful handling. In the process of electrodepositing the conducting polymers, the bond wires were exposed to the electrolytic deposition solution. These bond wires carrying the electrical potentials as applied to the external pins acted as a favourable surface for polymer growth. This created a very undesirable scenario resulting in polymer depositions in undesired places and, in some cases, created an electrical short between the adjacent terminals. To protect the bond wires during processing and have them electrically isolated from the electroplating solution, SU-8 was used as an insulating photoresist to do a selective encapsulation of the bond wires. The photoresist, SU-8, is a common negative photoresist used in patterning of the microelectronics circuits. The SU-8 resist can be cured with exposure to controlled ultraviolet radiation and temperature which renders it inert to many different chemicals and as well as adding mechanical strength.

The packaged chips were kept in a heating oven at 75°C for 30 minutes to remove any water molecules from the package cavity and chip surface. The SU-8 was carefully injected onto the bond wire areas surrounding the chip using a medical syringe to achieve selective encapsulation as shown in Fig. 3.4. The SU-8 encapsulated chips were again placed into the heating

oven at room temperature (20°C). The oven temperature was set to 60°C. The oven temperature ramps up at a rate of 10°C in every 50 second interval. The chips were kept inside the oven for 1 hour for a post deposition soft bake. The oven was turned off past 1 hour and allowed to cool down to the room temperature before taking out the samples. The soft baking process helps to evaporate the resist solvent and densifies the coating. This step was followed by exposure of the encapsulated chip to the ultraviolet radiation. Ultraviolet light wavelength of 350-400 nm was required to polymerize the SU-8 resist. The encapsulated chips were again placed into an oven at room temperature for post exposure bake. The oven temperature was set to 70°C and the chips were kept in the oven for 1 hour to develop the mechanical strength and chemically inert properties of the encapsulation layer. The oven was turned off and the chips were taken out when the oven temperature ramps down to the room temperature. As the SU-8 resist was only injected at the desired places and all of it was to be developed, no lithographic masks were required. The SU-8 coating successfully provided the required physical support to wirebonds but also kept them

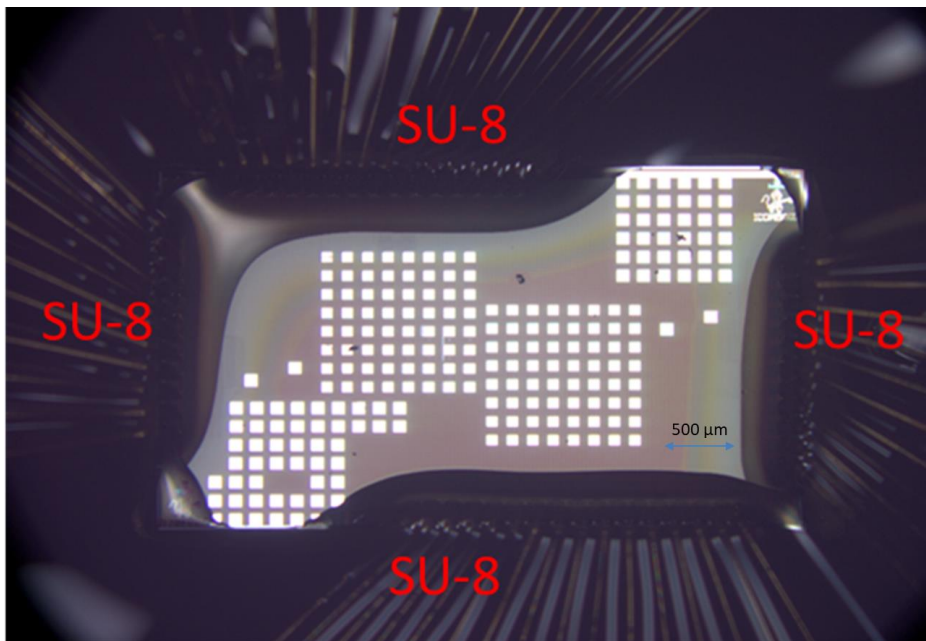


Fig. 3.4 The packaged chip with selective Encapsulation of wirebonds using SU-8

electrically isolated from the electrodeposition solution. A chip processed with this selective encapsulation of wirebonds is shown in Fig. 3.4.

The encapsulated chip with the gold coated extended floating gate pads was used for the electrodeposition of the polymers. The chip would require suitable electrical signals for the designed address and control circuit. Verilog code, running on an FPGA board, was used for the generation of the required electrical signals for the address and control logic. The code was implemented on an Altera DE2-115 development board. The general-purpose input/output (GPIO) pins on the board were configured to pass the required electrical signals to the chip. As the signals were passed to the chip, the polymer was deposited on individual sensors in the array.

An Agilent 4156C Precision Semiconductor Parameter Analyzer was configured and used as a potentiostat to generate the required electric potentials for the three-electrode electrodeposition cell setup. The 4156C parameter analyser has four high resolution source/measure units (SMU). To setup a cyclic voltammetry measurement, SMU1 of the parameter analyser was setup as an adjustable voltage source. The SMU1 was used to generate a voltage sweep on the working electrode (WE) and at the same time measure the current flowing through this terminal and the counter electrode (CE). The SMU2 was used to maintain a constant potential

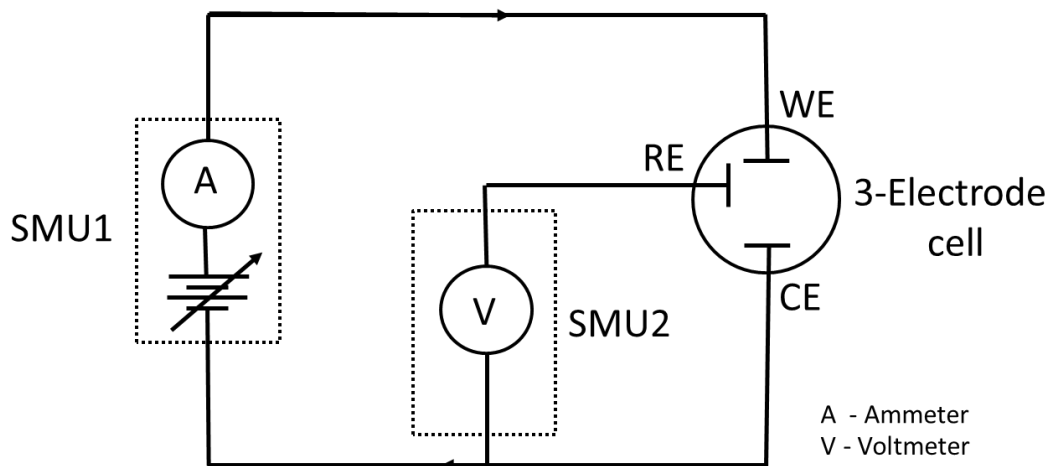


Fig. 3.5 Schematic diagram of the 3- electrode cell setup

at the reference electrode (RE). A schematic diagram of this three-electrode cell setup is shown in Fig. 3.5. Cyclic voltammetry was conducted to observe the electroactivity of the pyrrole monomer in the solution and find out the available redox potentials suitable for deposition of the polymer.

An aqueous solution used for the electrodeposition of polypyrrole was prepared with a 0.2 M pyrrole solution and 0.1 M p toluenesulfonic acid (pTSA) in 20 ml of DI water. The results from previous polymer electrodeposition experiments performed using interdigitated electrodes (IDE) were used for calculation of the current density through the working electrode. This current density number was used for calculation of the current flowing through the surface area of the much smaller on-chip working electrode; it was expected to be in the range of tens of microamperes. Fig. 3.6 shows the cyclic voltammetry (CV) results of the given aqueous solution using the 3-electrode cell setup. The working electrode current at the time of electrodeposition was observed to be larger than the estimated values from the IDE experiments. The chip was removed from the electrolytic solution to observe the PPy electrodeposition. The SU-8 photoresist shrunk in the process of curing and resulted in the formation of micro cracks in the encapsulation layer

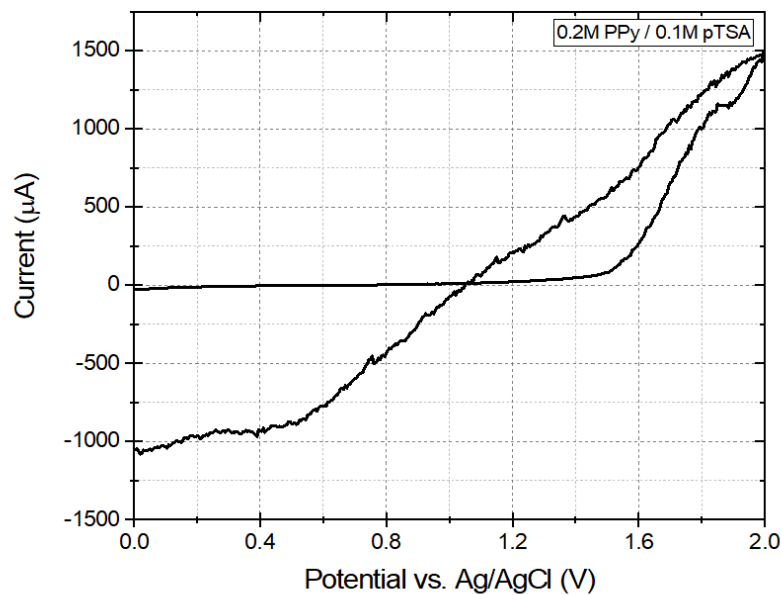


Fig. 3.6 Cycling behavior of 0.2 M Pyrrole, 0.1 M pTSA solution in DI water measured at gold plated floating gate electrode

which were not visible to the naked eyes. These micro-openings exposed certain areas of the bond wires to the electrolytic solution. Different terminals of the chip were applied suitable electric potentials to ensure the functioning of the on-chip address and control circuits. These gold coated bond wires at their given electrical potentials acted as a favorable area for the electrodeposition of the PPy films and contributed to the total current flowing in the electrochemical cell. This was the reason that the observed working electrode current was much higher as compared to the calculated values. Undesired growth of PPy was observed on the bond wires which electrically shorted the adjacent bond wires and affected the normal operation of the chip. A picture highlighting the undesired growth of the polymer on bond wires of the chip package is shown in Fig. 3.7.

To resolve this issue of polymer growth on the desired areas of the chip package, a double coating of SU-8 photoresist was employed. The wire bonds of the chip package were selectively encapsulated with an initial coat of the SU-8 photoresist. After curing this first layer of



Fig. 3.7 Undesired polymer growth on the wire bonds exposed to the electrolytic solution

SU-8, the resist coating process was repeated to ensure effective encapsulation of the chip package. The second layer of SU-8 encapsulation required very less volume of the SU-8 resist liquid. This process was difficult to control, as any excessive volume of liquid would flow onto the surface of the chip, effectively causing the process to fail. With great care, the yield of this process was high and most of the chip packages would have insulated wire bonds. In Fig. 3.8(a), a post electrodeposition picture of a chip package with the given double encapsulation approach is shown. The encapsulated chips were observed to have better insulation to the electrolytic solution. There were very few micro-openings in the encapsulation layer of some of the encapsulated chips, but these had a minimal effect on the chip operation. The encapsulation process was further improved by the application of a layer of “nail polish” on top of the second layer of SU-8 resist. In Fig. 3.8(b) a post electrodeposition picture of a SU-8 encapsulated chip package with an additional nail polish coat is shown. The 3-stage encapsulation process provided the required electrical isolation and mechanical support towards the forces experienced during the multiple

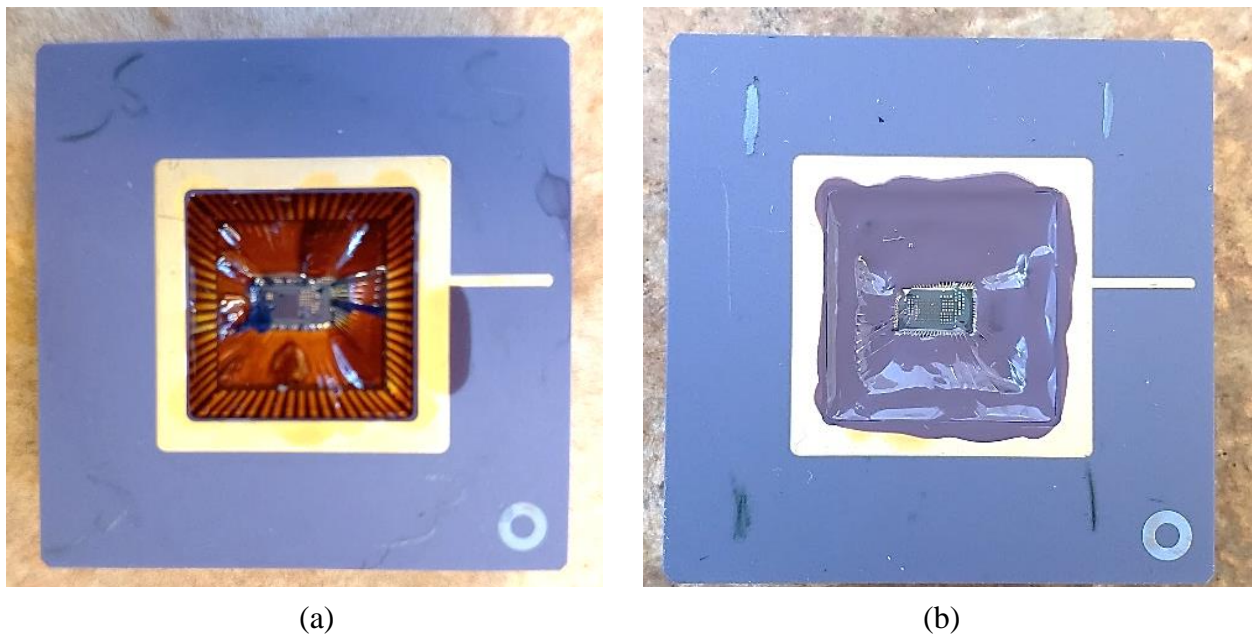


Fig. 3.8 (a) Chip package with double layer of SU-8 encapsulation (b) A chip package with encapsulation and an additional coating of nail polish

deposition and cleaning processes. The encapsulated chips were ready for electrodeposition of polymers using different chemical recipes.

3.4 Polymer depositions

A typical electrodeposition experiment can be summarised as follows. An encapsulated chip was mounted onto the chip socket of the breakout board. This assembly was clamped to the mechanical clamp arrangement in order to prepare the chip integrated container of the electrolyte. The required electrical connections to the chip addressing and control circuits were made. The counter, reference and the working electrodes and the gold coated floating gate extension surface electrodes were connected to the electrochemical cell setup. The electrolytic solution of monomer and the dopant chemicals dissolved in a solvent was prepared and poured into the syringe barrel container. One of the sensors from the array was addressed and selected for the cyclic voltammogram study. In this study, the working electrode was supplied with a sweep of a known potential range and the working electrode current was monitored. The cyclic voltammogram obtained by plotting the working electrode potential vs. current for this study was useful to analyse the electroactivity of the monomer inside the electrolytic solution and determine the suitable redox potentials (V_{REDOX}) for electrodeposition of conducting polymers. The given V_{REDOX} potentials were used for deposition of polymer films.

Several different cyclic voltammogram studies were performed. A few different cyclic voltammogram plots involving the pyrrole, aniline and styrene monomer-based electrolytes are shown in Fig. 3.9. Suitable redox potentials identified from the observed electroactivity of the monomer using the cyclic voltammogram plots are highlighted on the plots by the green arrows. The application of given redox potential to the working electrode immersed into the electrolytic solution for a given time interval resulted in the electrodeposition of the polymer films onto the

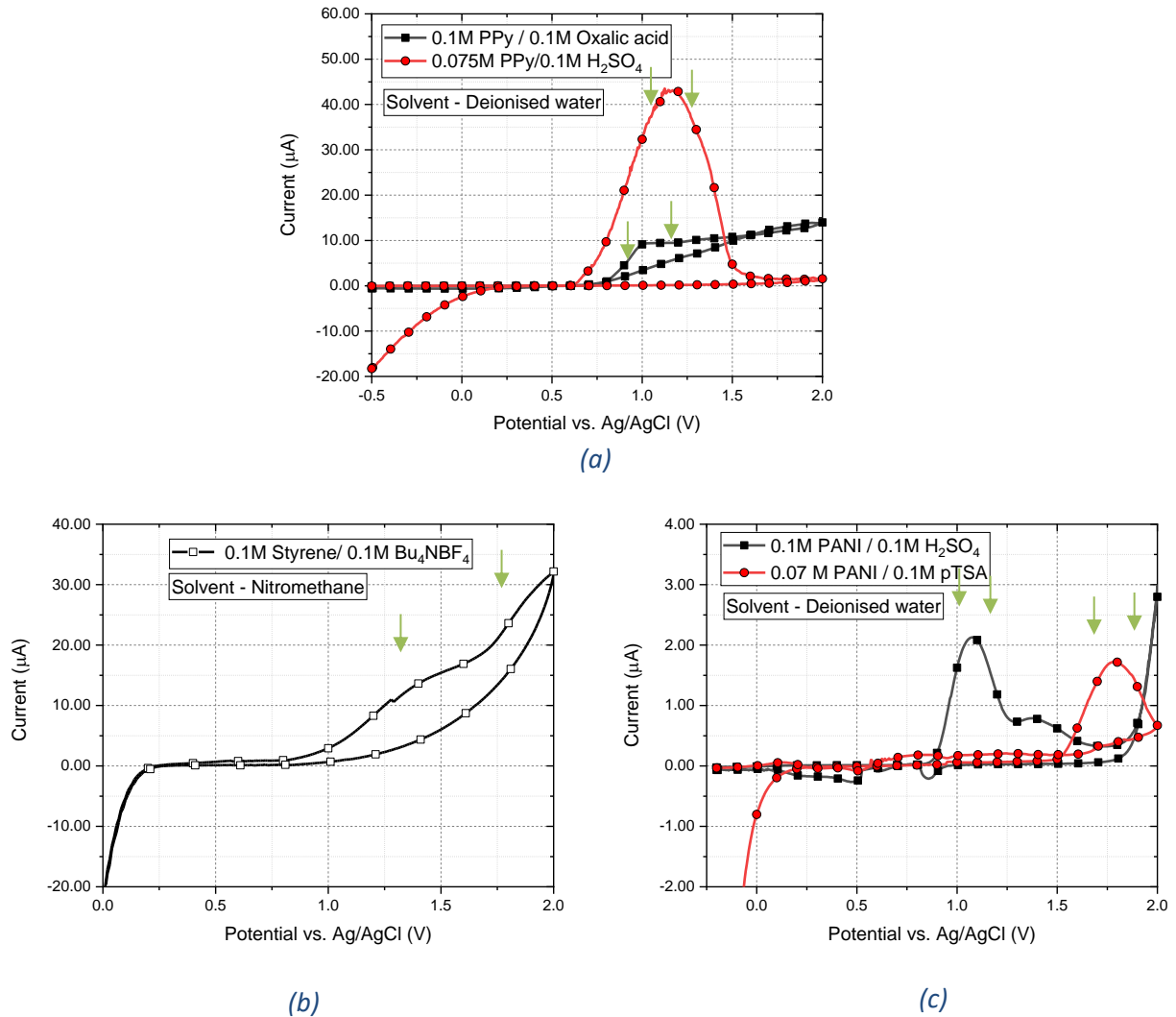


Fig. 3. 9 Cyclic voltammograms of (a) pyrrole monomer with sulfuric acid (red) and oxalic acid (black) (b) styrene monomer doped with Bu₄NBF₄ and (c) aniline monomer with pTSA (red) and sulfuric acid (black) showing different electrodeposition potentials available to grow the polymer films

working electrode surface. It is very important to control the time window used for the electrodeposition process to avoid over deposition of the polymer films. The polymer deposition experiments performed with the IDEs were useful to record the time required for the polymer growth to be visually observable. This was helpful to make a primary estimate of the amount of time required to coat the micro scoping extension pad surfaces.

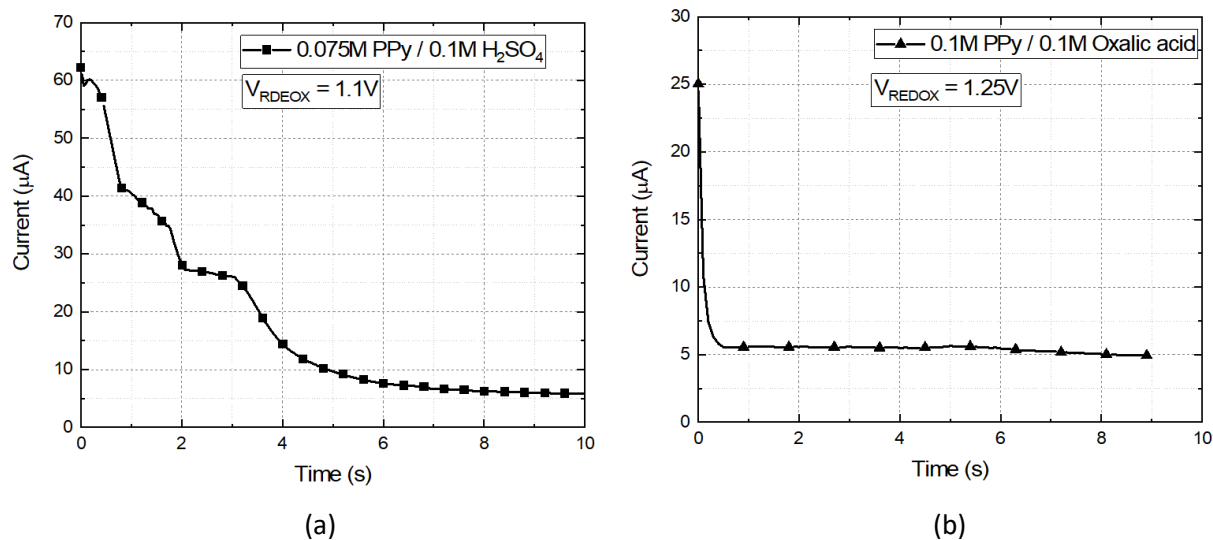


Fig. 3.10 The current measured at the floating gate terminal as a function of time during electrodeposition of pyrrole films using (a) 0.075M pyrrole monomer with 0.1M sulfuric acid and (b) 0.1 M pyrrole monomer with 0.1M oxalic acid

The plots, shown in Fig. 3.10(a) and (b), show the current flowing through the floating gate extension pad surface when a suitable redox potential was applied. The pyrrole monomer was doped with sulfuric and oxalic acid in separate 20 ml DI water solutions for preparation of the electrolytic solutions. The deposition time interval for the polypyrrole films doped with sulfuric acid was set to 10 seconds and for the oxalic acid doped film, the time interval used was 9 seconds. A V_{REDOX} potential of 1.1 V and 1.25 V were used, as identified from the cyclic voltammogram shown in Fig. 3.9(a). These two potentials used for electrodeposition of conducting polymers were applied to the extended floating gate pads of selectively addressed sensors of the 4x4 sensor array. In Fig. 3.11 a microscope image of an electrochemically deposited and compositionally different conducting polymer is shown after depositions onto the surface of extended floating gate pad. The success of selective electrodeposition of conducting polymers on the sensor array was one of the most important achievements towards the development of this olfaction system.

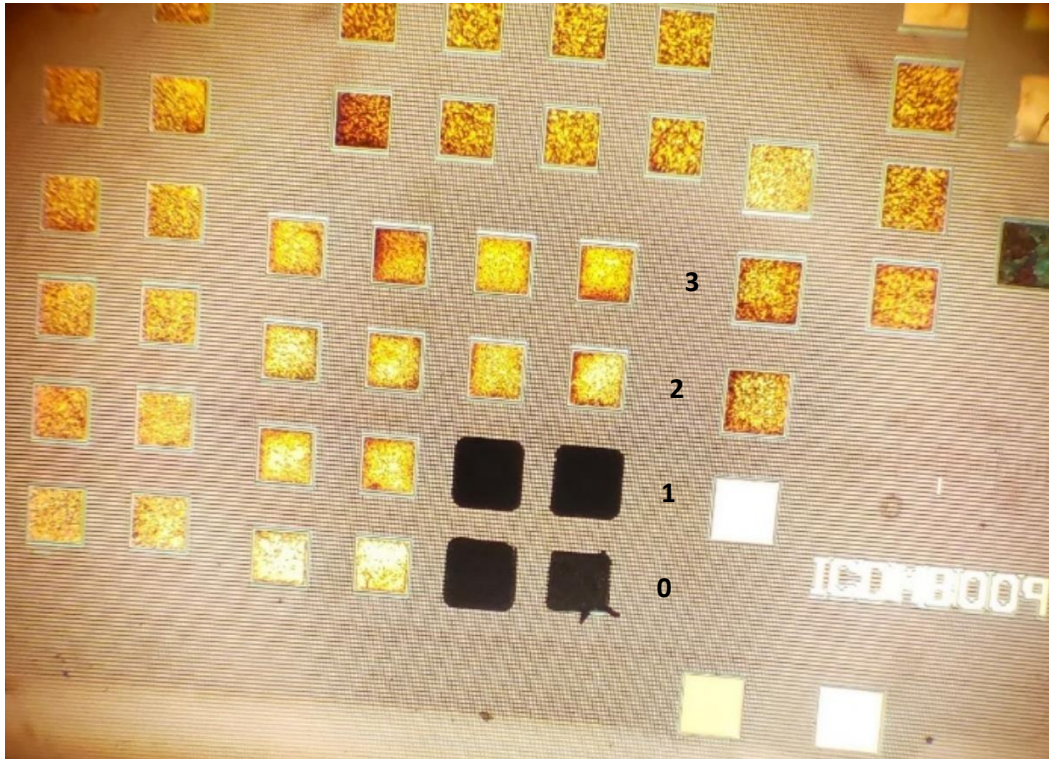
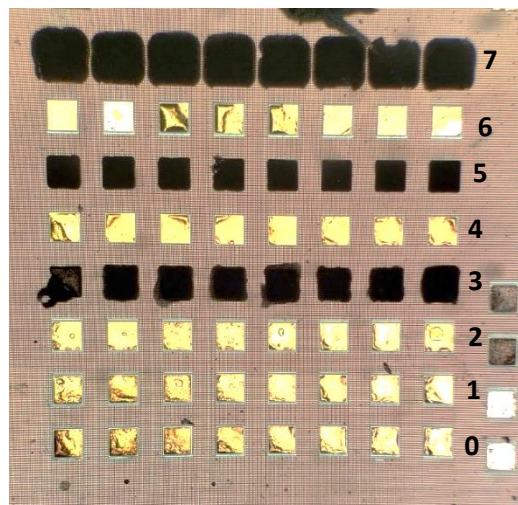
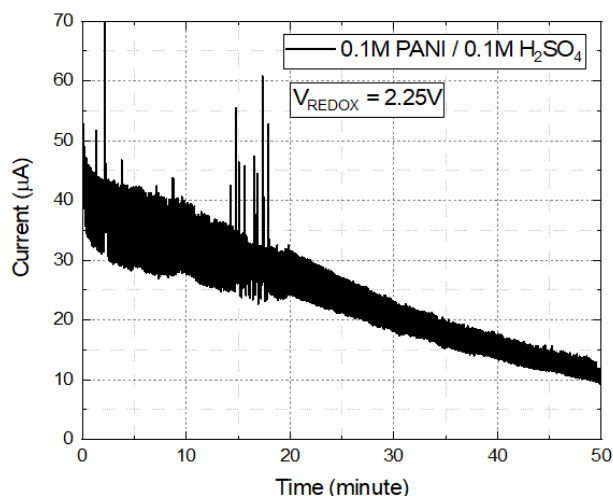


Fig. 3.11 Chemically diverse Conducting Polymer films grown on the extended floating gate pads of the 4x4 sensor array, PPy/H₂SO₄ films on row 0, PPy/oxalic acid films on row 1 and clean gold coated extension pads in row 3 and 4

Using a similar set up and the automated address generation Verilog code, the Altera DE2-115 development board was used to address different rows of the sensor array and coat the extended floating gate pads. This experiment was performed using an electrolytic solution prepared from 0.1M aniline monomer and 0.1M sulfuric acid mixed in 20 ml DI water. A clock frequency of 1 Hz was used to generate different sensor addresses. In Fig. 3.12(b), the 8x8 sensor array with the given row numbers that were used in this experiment. The electrodeposition process at $V_{\text{REDOX}} = 2.25 \text{ V}$ was first performed on row-7 of the 8x8 sensor array. A time interval of 500 seconds per sensor (total time 4000 seconds) was used for the given row of 8 sensors. Excessive deposition of polymer films onto the extension pad surface was observed. The experiment was



(a)

(b)

Fig. 3.12 (a) The current measured at the floating gate terminal of row-5 sensors as a function of time during electrodeposition of PANI film using 0.1M aniline monomer with 0.1M sulfuric acid and (b) PANI films grown on the extended floating gate pads of the 8x8 sensor array

performed again using automated addressing of the sensors on row-3 with an average deposition time now reduced to 400 seconds per sensor. The polymer growth for this row was better controlled but still was not a clean deposition. The time interval was reduced to 375 seconds per sensor and the process was repeated on row-5. The electrodeposition current as a function of time for this deposition process is shown in Fig. 3.12(a). The calibration of the electrodeposition time interval was successful in achieving clean polyaniline (PANI) films deposited onto the given row of the sensor array. Electrodeposition of many more chemically diverse conducting polymers onto the sensor array was performed using a similar approach as explained in this section. Testing of the sensors and sensor array system under the controlled influence of many different vapour analytes is explained in the next chapter.

Chapter 4 – Sensor characterization for analyte exposure

A very specific system is required for testing of the floating gate sensor chips. This system was designed to contain the chips in a controlled environment of analyte vapours. This vapour flow system also provided easy access to all necessary electrical connections to the external electrical instruments. The cables to the external electrical instruments were used to test the electrical behavior of the chips in different analyte environments. The polymers are very sensitive to any change in their environment [54]. A nitrogen flow is used as a reference environment under which the sensors are initially calibrated.

4.1 The vapour flow setup

To test the electrical properties of the polymer coupled sensor in an analyte environment, a vapour flow setup was designed using mass flow controllers. A schematic diagram of the designed vapour flow setup is shown in Fig. 4.1. The concentration of the analyte

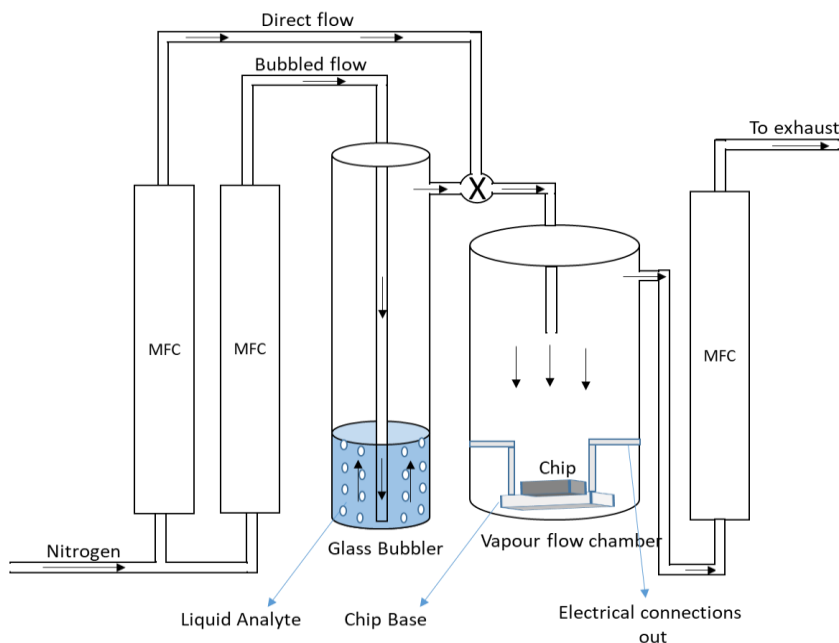


Fig. 4.1 Vapour flow setup for characterization of system in controlled analyte vapour environment (MFC : Mass flow controller)

vapour in the flow chamber was controlled using a mixture of direct nitrogen and bubbled nitrogen flow through a glass bubbler that was filled with a liquid analyte.

For setting up the desired vapor concentration, first, the glass bubbler was filled with 20 ml of the liquid analyte under test. Next, a controlled flow of nitrogen, that works as a carrier of the analyte vapour, was bubbled through the analyte into the flow chamber. The vapour flow chamber has a base where the chips can be easily mounted and replaced whenever required. The chip base has electrical “pass-through” connectors to the external world, that were used to enable external connection for the required electrical signals. In these experiments, the concentration of analyte vapour in the flow chamber was kept to simple percentage numbers, calculated from the ratio of bubbled nitrogen flow through the analyte to total nitrogen flow in the chamber. For example, a mix of the direct flow of nitrogen at 2140 ml/min and a bubbled nitrogen flow through the analyte filled bubbler unit at 176 ml/min, which is calculated to be $100 * [176/(176 + 2140)] = 7.60 \%$ analyte vapour flow.

Before the polymer deposition and system characterization, it was very important to test the individual FGMOS sensors to establish their electrical performance in absence of polymers on their floating gate. These electrical operating parameters were very helpful in optimizing the designs of the other processing circuits on the chip, such as the transimpedance amplifier. The operation of the FGMOS sensor, using either the control or floating gate to control the FET channel in the substrate was expected to resemble a normal MOS transistor. The effective dielectric thickness for the control gate is $\sim 5 \times$ that of the gate oxide thickness between the floating gate layer and the substrate. The thickness of the dielectric layer between the gate and substrate has an inverse relationship with the magnitude of the field produced in the dielectric. Therefore, it was expected that the control gate terminal to require a higher voltage compared to

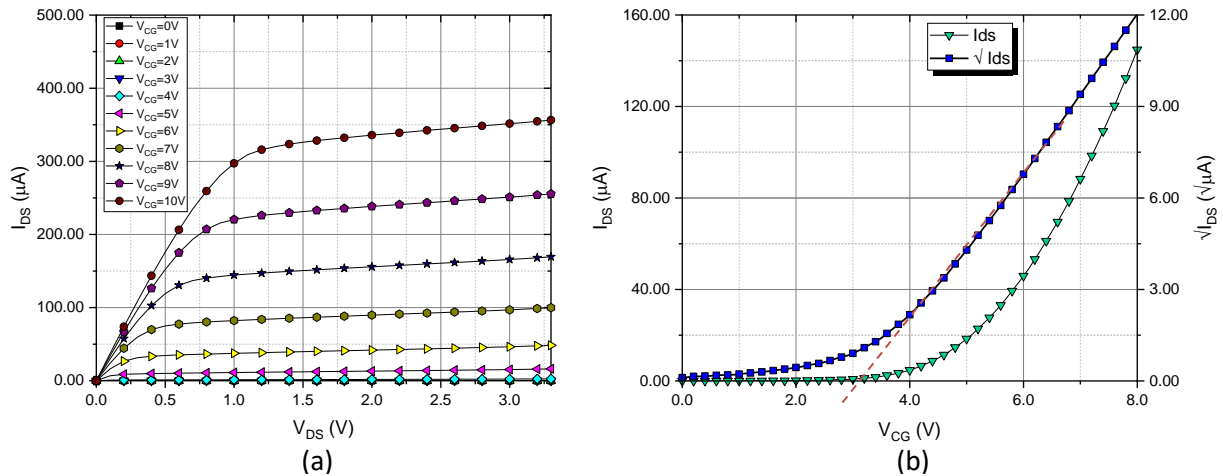


Fig. 4.2 Electrical characteristics of the FGMOS sensor (a) Drain characteristics (b) Transfer characteristics

the floating gate, for the same equivalent drain current in the channel. In Fig. 4.2(a), the drain characteristics of one of the FGMOS sensors is shown. This device had a gate width of $10 \mu m$ and a gate length of $1 \mu m$. The measurements show the responses for different control gate voltages (V_{CG}) as a function of the drain voltage (V_{DS}), from 0-3.3 V. From these drain current characteristics it can be observed that the operation of the sensor resembles that of a typical n-MOS transistor.

The magnitude of drain current was observed to be few microamperes or less for control gate voltages of less than 3 V. To gain a better insight into the effect of the control gate control (V_{CG}) operation on the drain current (I_{ds}), the transfer characteristic of the sensor was studied. The sensor was biased with a constant drain voltage, $V_{DS} = 1$ V, and the V_{CG} was swept from 0-3.3 V. The resultant drain current was measured and plotted against the V_{CG} as shown in Fig. 4.2(b). From multiple such measurements, it was observed that the sensor subthreshold region operation begins for V_{CG} in the range of 2.5 V - 3 V. Analysis of data from this measurement revealed that the threshold voltage, with respect to control gate operation, is very close to 3 V. The subthreshold region of operation may shift a little for different sensors on the same or different

chip because of silicon process variations. This study was very useful to determine the biasing points where the sensor has maximum sensitivity.

4.2 Polymer coated sensor transfer characteristics

The floating gate extension pad of a sensor was coated with polypyrrole (PPy) film from a solution of 0.1 M pyrrole monomer and 0.1 M sulfuric acid (H_2SO_4) in 20 ml deionised water (DI) at a redox potential of 1.65 V. This polymer coated sensor was initially tested for transfer characteristics in a nitrogen environment at a constant V_{DS} of 1 V. An Agilent 4156C precision semiconductor parameter analyzer was used for this measurement processes. The nitrogen flow conditions were maintained for several hours and the measurements were repeated. During this time, no noticeable change in the sensor drain current was observed.

To observe the effect of exposure of a given analyte vapor on the sensor operation, the chip was kept in a 7.60% relative flow of the analyte for 1 hour. The vapour concentration, as mentioned previously, was generated using a mixture of 2140 ml/min of nitrogen with 176 ml/min of bubbled nitrogen through the analyte. The measurements were performed under unchanged electrical conditions. This was repeated after exposing the sensor to 6 different analyte vapors each

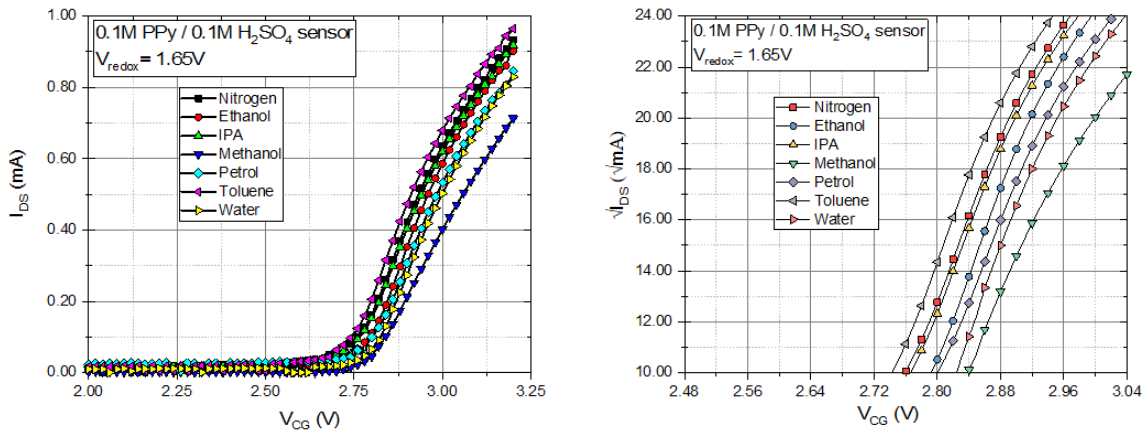
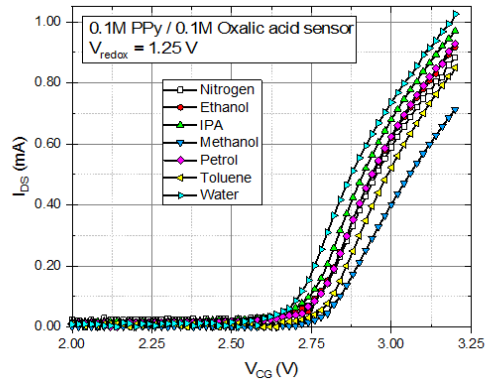


Fig. 4.3 (a) Transfer characteristics of the PPy/H₂SO₄ coated sensor in 6 different analytes after 1 hour of exposure and (b) rescaled plot of it on a linear scale of drain current

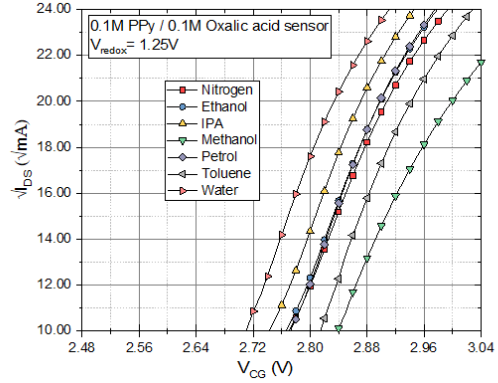
for a period of one hour. The analytes tested were ethanol, methanol, IPA, petrol (gasoline), toluene and water. The measurement data, (I_{DS} vs V_{CG}) is shown in Fig. 4.3 for all of these analyte exposures.

The measurement plot shows 6 visibly distinct drain current traces corresponding to the exposure to each of the analyte compared after the initially calibrated nitrogen exposure. The drain current (I_{DS}) scales with the square of the gate voltage (V_{CG}) in the subthreshold regime. The square root of the sensor current (shown in Fig. 4.3(b)) shows this effect much more dramatically especially for control gate voltages in the range of 2-4 V. The different x-axis intersection points of these traces represent the new threshold voltage of the sensor under influence of a particular analyte. This experiment shows that a measurable shift in sensor characteristics is evident after exposure to these different analytes. After each analyte exposure cycle, the sensor was exposed to pure nitrogen flow for a duration of at least 30 minutes. The nitrogen exposure was able to refresh the device characteristics to the initial status. Further experiments and analysis were required to develop a fuller understanding of the observed threshold voltage shift. This will enable an estimation of the equivalent charge coupled to the floating gate under an analyte influence.

Five other monomer/dopant combinations were used for the synthesis of a new set of polymers. The dopants, oxalic acid ($C_2H_2O_4$), potassium chloride (KCl) and p-toluenesulfonic acid ($C_7H_8O_3S$) were used in a 0.1M concentration in 20ml DI water with a 0.1M concentration of pyrrole monomer to synthesise three new polypyrrole films. The other chemical monomer unit used for the polymerization process was aniline. A 0.1M concentration of aniline monomer was used to synthesise two chemically diverse polyaniline films using dopant of 0.1M concentrated sulfuric acid and p-toluenesulfonic acid (pTSA). It is very important to perform a cyclic voltammetry measurement study of the new polymer recipe. This study indicates suitable redox

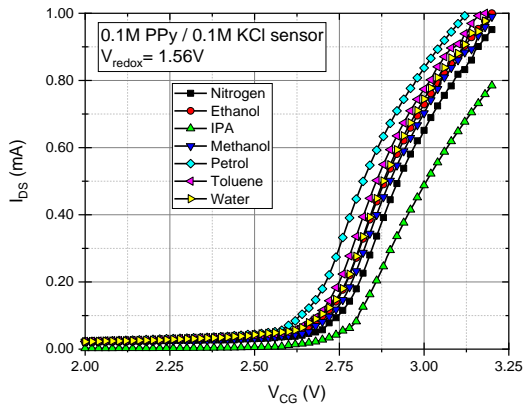


(a)

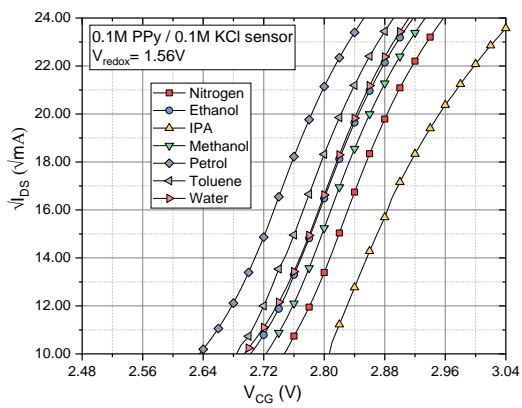


(b)

Fig. 4.4 (a) Transfer characteristics of the PPy/Oxalic acid coated sensor in 6 different analytes after 1 hour of exposure and (b) rescaled plot of it on a linear scale of drain current

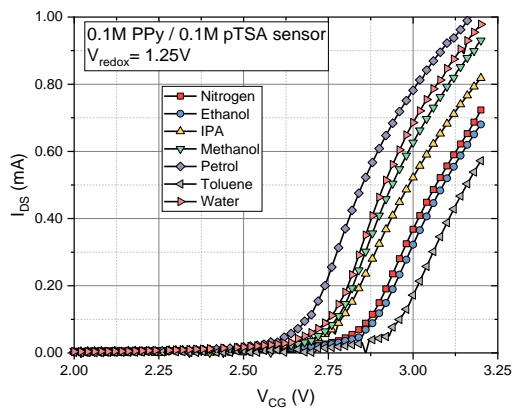


(a)

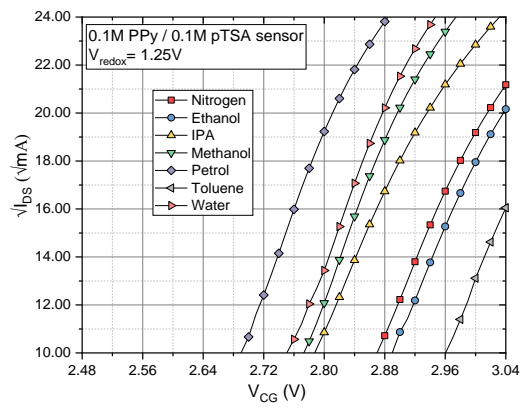


(b)

Fig. 4.5 (a) Transfer characteristics of the PPy/KCl coated sensor in 6 different analytes after 1 hour of exposure and (b) rescaled plot of it on a linear scale of drain current



(a)



(b)

Fig. 4.6 (a) Transfer characteristics of the PPy/pTSA coated sensor in 6 different analytes after 1 hour of exposure and (b) rescaled plot of it on a linear scale of drain current

potentials for electrodeposition of each polymer film. For all the polymers discussed in this chapter, the redox potential used to grow the polymer film is mentioned on the measurement data plots. The five new polymer film, integrated sensors were used to repeat the above discussed transfer characteristics experiment. All of the pyrrole-based polymers were integrated with sensors having a width to length ratio of 10:1. The Figs. 4.4-4.6, the effect of analyte exposure on these pyrrole-based sensors are shown.

The polyaniline films were integrated to sensors having a width to length ratio of

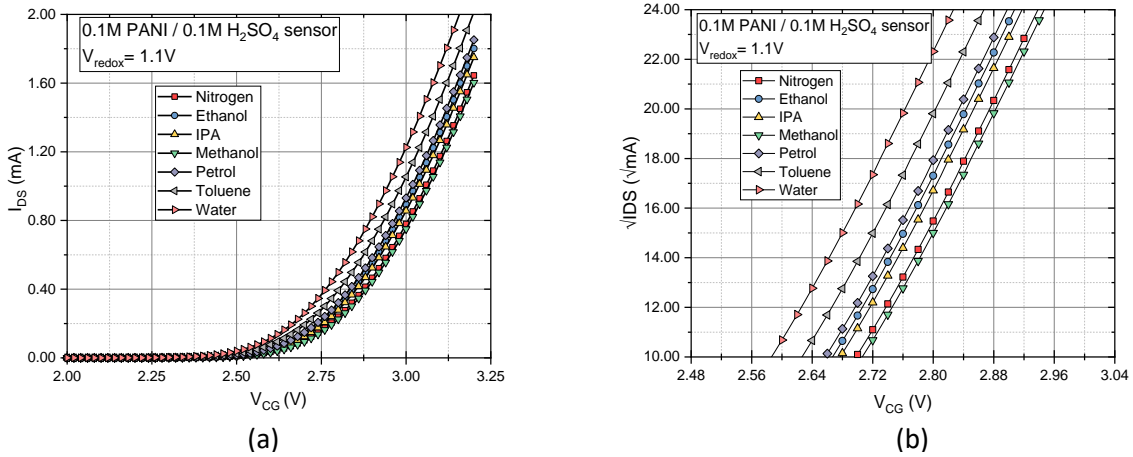


Fig. 4.7 (a) Transfer characteristics of the PANI/H₂SO₄ coated sensor in 6 different analytes after 1 hour of exposure and (b) rescaled plot of it on a linear scale of drain current

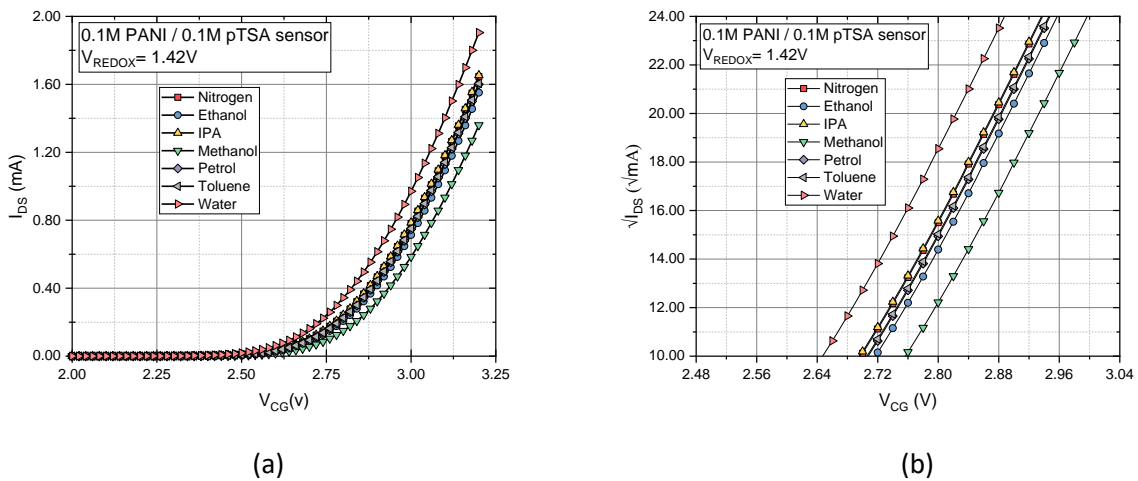


Fig. 4.8 (a) Transfer characteristics of the PANI/pTSA coated sensor in 6 different analytes after 1 hour of exposure and (b) rescaled plot of it on a linear scale of drain current

20:1. The width to length ratio of a sensor is directly proportional to the sensor current. Just like the PPy integrated sensors, the polyaniline-based sensors also had a sensitivity to the vapour analytes. In Fig. 4.7 and Fig. 4.8, these data plots from this experiment are shown. As seen from the experiments shown in for all of these devices (Fig. 4.3 - 4.8), each of the sensor/polymer combination has a distinct response to the tested analytes. Exposure to these analytes has shown to cause a very distinct shift in the threshold voltage of the sensors. This observation can be mapped to an effective charge on the floating gate that would cause an equivalent change in the threshold voltage. After the analyte exposure, the nitrogen refreshing of the sensors was observed for most of the above discussed polymer integrated sensors. In a very few exposure experiments, the pure nitrogen driven recovery was not able to return the current to the pre-exposure level and a hysteresis of sensor current was observed. In such cases, a negative gate voltage of -3.3 V was applied to the control gate terminal for a short duration of time (typically 30 second in the given experiment set) which was helpful to regain the sensor characteristics to the baseline.

4.3 Coupled charge analysis

To better understand the shift of threshold voltage during analyte exposure, further analysis of the experimental results was required. The data from Figs. 4.3(b) - 4.8(b) was used to calculate the threshold voltage using a linear extrapolation method [71]. The control gate had a precision of $\pm 1\text{mV}$ for all of these experiments. The threshold voltage values, as calculated using this linear extrapolation method are given in Table 4.1. The observed change in threshold voltage (ΔV_{THN}) was calculated as the change in the threshold voltage under the influence of an analyte relative to its magnitude under the nitrogen environment. The observed ΔV_{THN} value for these experiments is given in Table 4.2. In Fig. 4.9, a graphical representation of this change is shown in the form of a bar chart. In this figure, it can be observed that the electrical response of the

sensor/polymer combination is quite unique for each of the tested analytes. Collective information set from each group of sensor/polymer pairs would then be able to produce unique ‘fingerprint’ for a given tested analyte.

Polymer	Threshold Voltage (V)						
	Nitrogen	Ethanol	IPA	Methanol	Petrol	Toluene	Water
PPy / H ₂ SO ₄	2.76	2.79	2.765	2.84	2.8	2.74	2.82
PPy / Oxalic	2.77	2.765	2.74	2.84	2.77	2.81	2.71
PPy / pTSA	2.87	2.89	2.79	2.77	2.69	2.96	2.75
PPy / KCl	2.75	2.70	2.81	2.72	2.63	2.68	2.69
PANI / H ₂ SO ₄	2.70	2.67	2.68	2.71	2.66	2.63	2.59
PANI / pTSA	2.70	2.72	2.70	2.76	2.70	2.71	2.65

Table 4.1 The observed threshold voltage at control gate under influence of vapour analytes

Polymer	Observed change in threshold voltage (ΔV_{THN} , mV) relative to nitrogen exposure					
	Ethanol	IPA	Methanol	Petrol	Toluene	Water
PPy / H ₂ SO ₄	30	5	80	40	-20	60
PPy / Oxalic	-5	-30	70	0	40	-60
PPy / pTSA	20	-80	-100	-180	90	-120
PPy / KCl	-50	60	-30	-120	-70	-60
PANI / H ₂ SO ₄	-30	-20	10	-40	-70	-110
PANI / pTSA	20	0	60	0	10	-50

Table 4.2 The Observed change in threshold voltage (ΔV_{THN}) relative to Nitrogen

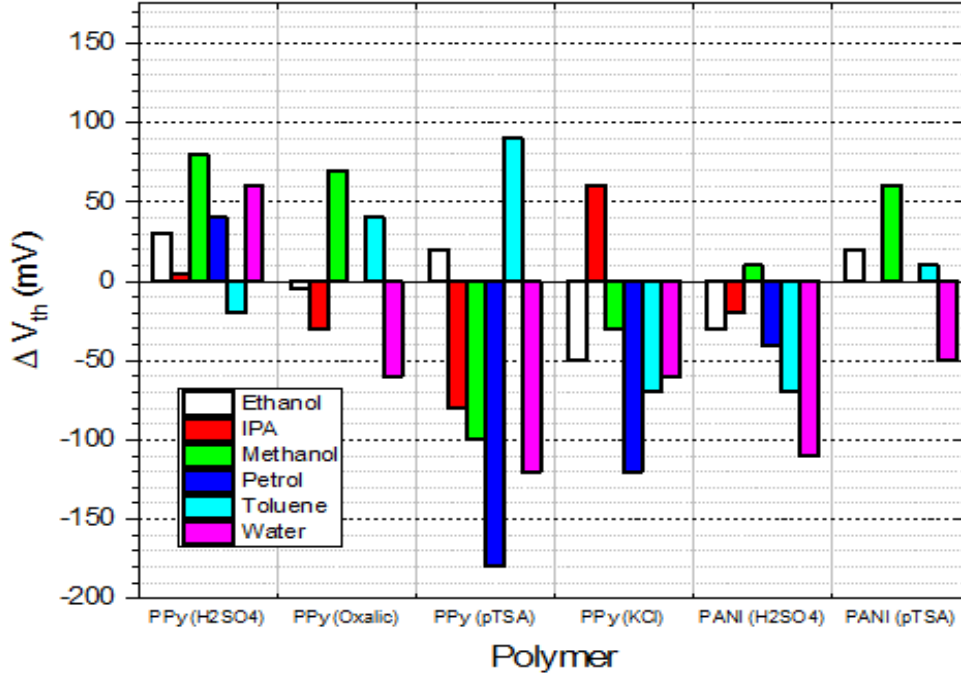


Fig. 4.9 Normalised threshold voltage (ΔV_{th}) relative to nitrogen for 4 PPy and 2 PANI based sensors doped with variable dopants for their exposure to 6 analytes

For an nMOS transistor operating with the source and substrate grounded, the charge per unit area in the depletion region is given by[66],

$$Q_b = \sqrt{2 q N_A \epsilon_{Si} |\phi_S - \phi_F|} \quad (4.1)$$

where q is the electron charge, N_A is the substrate doping concentration (p type), ϵ_{Si} is the permittivity of silicon, ϕ_S is the electrostatic potential at oxide silicon interface and ϕ_F is the electrostatic potential of the substrate. For a p-type substrate, ϕ_F is a negative number and in absence of an external gate potential, ϕ_S , is also a negative number. An external positive potential applied to the polysilicon gate increases the ϕ_S potential. When the external gate potential becomes large enough to make $\phi_S = -\phi_F$; a channel is formed at the substrate oxide interface. The charge in the channel at inversion is given by[66]

$$Q_b^{inv} = \sqrt{2 q N_A \epsilon_{Si} |-2\phi_F|} \quad (4.2)$$

The externally applied gate potential to cause channel formation by inversion of the substrate close to the gate oxide interface is the threshold voltage for the nMOS device, given as[66],

$$V_{THN} = -\phi_{ms} - 2\phi_F + \frac{Q_b^{inv} - Q_{ss}}{C_{ox}} \quad (4.3)$$

where, V_{THN} is the threshold voltage of the n-type MOSFET, ϕ_{ms} is the surface potential between the substrate and the polysilicon gate, Q_b^{inv} is the charge per unit area in the depletion region at inversion, C_{ox} is the gate-oxide capacitance per unit area. Assuming a perfect gate oxide in the nMOS, there would be no fixed charge due to gate oxide imperfections, and therefore, Q_{ss} , initially would be zero.

As stated earlier, the operation of a FGMOS sensor resembles normal field effect transistor and the previously given equations can be used to understand the sensor behaviour. It was observed that the sensors, upon integration to different polymers, showed a small change in the sensor threshold voltage during measurements made under the nitrogen environment. This change was assumed to be due to the change in the gate - substrate surface potential (ϕ_{ms}) because of the new polymer material coated on the extended floating gate surface. The surface potential should remain constant once the sensor gets integrated with a polymer film. The electrostatic potential of the substrate (ϕ_F) depends on substrate doping and as such, it should not be affected by the exposure to analytes. The doping concentration of substrate is determined by the CMOS technology and remains constant for all of the post fabrication processes.

Given that all of the parameters affecting the threshold voltage of the sensor are technology dependent and remain constant during post fabrication, the observed changes of the threshold voltage upon exposure of the sensors to vapour analytes must be due to introduction of the additional charge in the system. The sensors were operated with an electrical bias on the control gate. This electrical bias sets up an electric field in the ILD2-*poly1*-gate oxide-substrate region to

initiate a channel formation in the substrate. The *polyI* layer, in this gate stack region, is electrically conductive and is connected to an analyte sensitive polymer. In a case where the analyte/sensor interaction produces charge on (or in) the polymer layer, the charge will be electrically coupled to the electrical field generated by the control gate bias. Any charge on the floating gate layer of the sensor will add up to the control gate generated field and produce an equivalent image charge in the channel. This image charge will modify the total charge present at the channel under the influence of the applied gate potential, effectively modifying the device operating points such as the threshold voltage. A mathematical analysis was developed to map the ΔV_{THN} to the likely change of charge in the inversion region.

To calculate the quantity of the effective charge responsible for each of the observed threshold voltage variations, assuming that the net charge in the channel under influence of nitrogen is termed Q_b^{inv} and when the sensor is under influence of any analyte, the charge is modified to a new value, $Q_b^{inv'}$. As such the difference, $Q_b^{inv'} - Q_b^{inv}$, should represent the change in the effective charge causing the observed threshold voltage shifts. Using the expression of threshold voltage given in Eqn.4.3, the net change in charge can be calculated using

$$(Q_b^{inv'} - Q_b^{inv}) = (V_{THN(Analyte)} - V_{THN(Nitrogen)}) * Cox \quad (4.4)$$

This equation (Eqn. 4.4) actually represents the net change in the charge density in the channel. To calculate the change in the number of charge carriers (electrons) in the channel, the channel area and the electron charge need to be included. The channel area can be easily calculated as a product of sensor width and length. The mathematical equations (Eqns. 4.1-4.3) were coded as a MATLAB program along with the process parameters from the *cmosp35* technology. In Table 4.3 the calculated change in the number of charge carriers is given.

Polymer	Calculated change in the number of electrons in the channel					
	Ethanol	IPA	Methanol	Petrol	Toluene	Water
PPy / H ₂ SO ₄	-1033	-172	-2756	-1378	689	-2067
PPy / Oxalic	172	1033	-2412	0	-1378	2067
PPy / pTSA	-689	2756	3446	6203	-3101	4135
PPy / KCl	1723	-2067	1033	4135	2412	2067
PANI / H ₂ SO ₄	1033	689	-344	1378	2412	3790
PANI / pTSA	-689	0	-2067	-344	-344	1723

Table 4.3 The calculated numbers for change in electron count in the channel

The data shown in Table 4.3 show that the numbers representing the change of charge in the channel can be of either polarity. The interaction of analyte vapors to the polymer on the floating gate of the sensors, in this case, can be linked to the availability of additional charge carriers or trapping of some of the existing charge carriers depending on the direction of the change of threshold voltage. When the calculated number is positive, it indicates the sensor analyte interaction has produced additional charge carriers in the substrate and thus the corresponding threshold voltage is seen to be increased. The reverse effect is seen with the reduction of threshold voltage upon exposure of an analyte which is seen when the net change in the charge is calculated to be a negative number. This negative sign is an effective indication of the reduction of a number of charge carriers in the substrate.

The olfactory system of this work was designed to operate in the subthreshold regime. In the subthreshold regime, a small change in the gate bias is able to produce orders of magnitude changes in the sensor current. It was very important to first analyze the performance of

this system in the subthreshold regime. For the experimental data shown in the previous Figs. 4.3-4.8, it can be observed that the maximum change of drain current for a sensor was not confined to a single voltage point for all of the sensors. Given that a common applied voltage for all the sensors would make the comparative analysis more convenient, a voltage of 3 V in the subthreshold regime is selected for analysis of the change in sensor current response upon exposure to the analytes. The sensor drain current (I_{DS}), with a control gate voltage of 3 V, for all the sensor/polymer groups, has been logged into a single table. This data was then processed to calculate the percentage change in the analyte modulated sensor current normalized to a nitrogen flow in that device, under the same conditions. In Fig. 4.10 a bar diagram, useful for a comparative analysis of the sensor response to the different analytes, is shown. It can be observed that the response of the sensor/polymer combination was quite unique for most of the test analytes. A change of 10% or

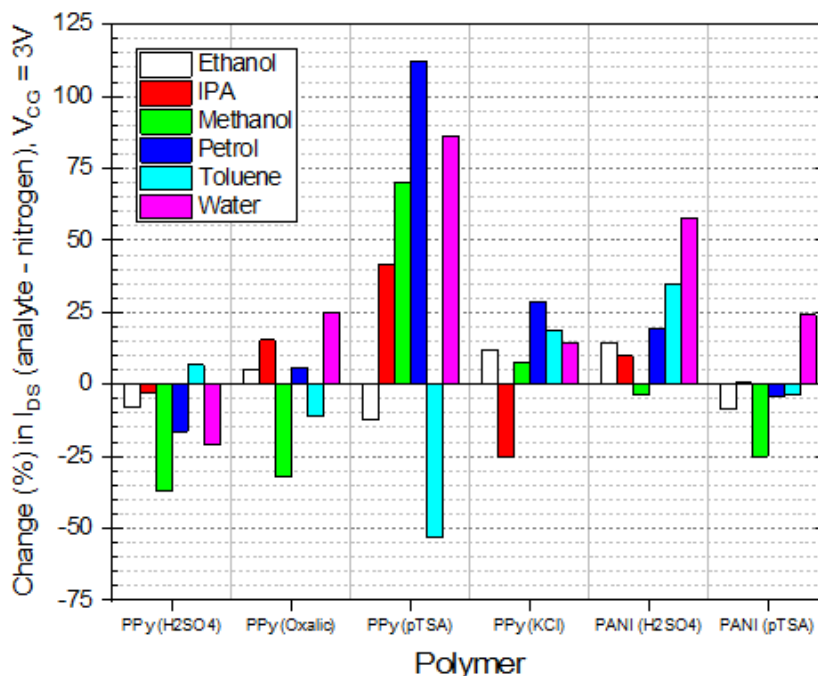


Fig. 4.10 Normalised change in sensor current of 4 PPy and 2 PANI based sensors doped with variable dopants for their exposure to 6 analytes

higher was frequently observed. The results motivated a study of the sensor biased at constant voltages in the subthreshold regime for prolonged exposure to different analytes.

4.4 Sensor transient response

A set of experiments were designed in an effort to test the transient performance of the sensors and analyse the final steady state equilibrium response upon exposure to any given analyte. In this set of experiments, the polymer coated sensor was initially kept in the nitrogen environment at a constant drain current I_{DS} ($> 10^{-6}$ A) using a constant electrical biasing condition. The nitrogen flow conditions were maintained for several hours during which no noticeable change in the sensor drain current was observed. After the nitrogen measurements, the sensors were subjected to analyte exposure at a known flow ratio. The sensor current was measured continuously throughout the nitrogen and analyte exposure cycles.

4.4.1 Polypyrrole based sensors

A pTSA doped PPy based sensor was tested for transient response to four different analytes. The sensor was initially kept in a saturated nitrogen environment by maintaining a constant flow of 2140 ml/min of nitrogen in the vapour chamber. The experiment began with the application of 3 V DC bias to control gate of the sensor and the sensor current was measured. A glass bubbler was prepared for an analyte test by filling it with 20 ml of analyte liquid. After 30 minutes, 176 ml/min of nitrogen was bubbled through the glass bubbler while the direct flow of nitrogen was maintained at 2140 ml/min. As stated previously, the flow ratio was described as 7.60% of the total analyte containing flow. The bubbled nitrogen, acting as a carrier gas, carries analyte particles into the test chamber. The measurements were concluded after 90 minutes. The

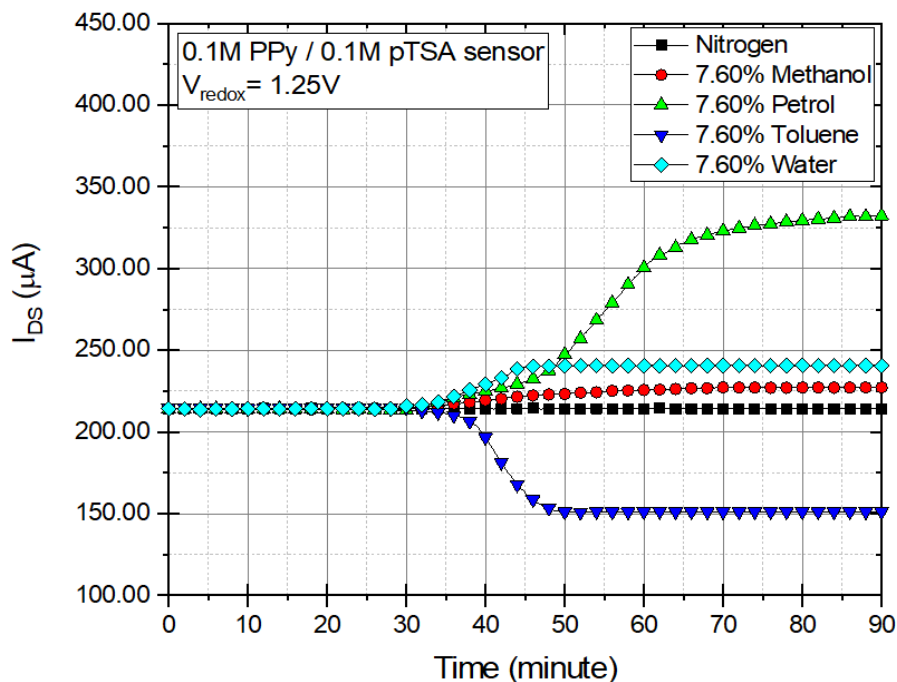


Fig. 4.11 Transient response of PPy/pTSA based sensor for exposure to 4 analytes

sequence was repeated for four different analytes: methane, petrol, toluene and water. The measured data of the experiment is plotted in Fig. 4.11.

It can be observed that the sensor current remains constant under the nitrogen flow while a unique response to every exposed analyte is seen. The response time of the sensor was observed to vary for different analytes. The PPy/pTSA film integrated into this sensor showed its highest sensitivity to petrol. However, this sensor also has the slowest response time for a petrol exposure. The sensor has the fastest response time for water vapours. The water absorption properties of polypyrrole are already known [72]. Toluene was the only one of the four tested analytes to cause a decrease in the sensor current. The experimental results do confirm that the sensor operation was able to produce distinguishable electrical responses upon exposure to these different analytes. In the next experiment, shown in Fig. 4.12, the sensor recovery and repeatability were analysed for an H_2SO_4 doped PPy sensor.

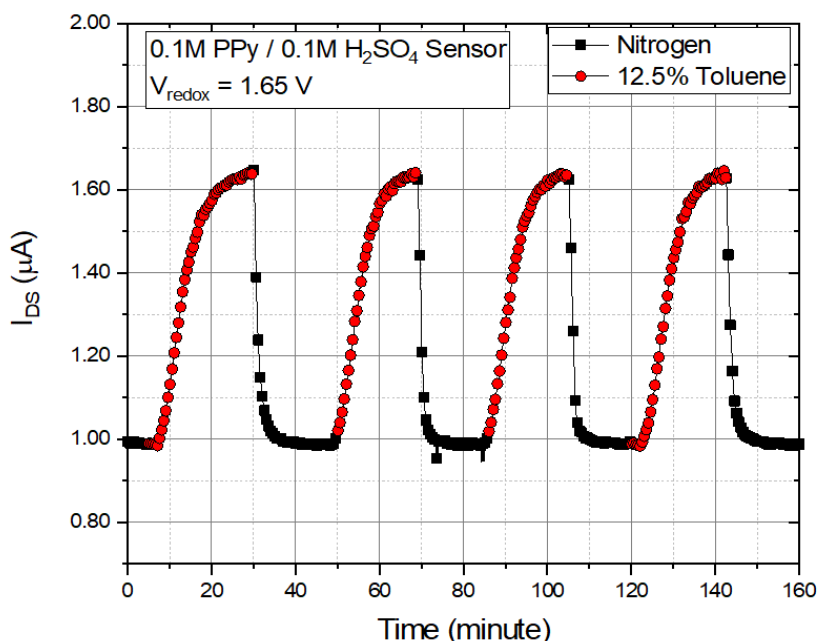


Fig. 4.12 Transient response of PPy/H₂SO₄ based sensor for cyclic exposure to nitrogen and toluene

In this experiment, a sensor integrated with a polypyrrole film, synthesised from 0.1M pyrrole and 0.1M H₂SO₄ solution at a redox potential of 1.65 V, was exposed to alternate cycles of nitrogen and toluene(12.5%). The sensor was biased very low in the subthreshold regime with a current of $\sim 1 \mu\text{A}$ with a control gate potential of 2.74V. The mass flow controller for toluene flow was switched ON and OFF in random intervals between 20-30 minutes. The nitrogen and toluene cycles are color coded with black and red respectively. It can be observed that the sensor operation was very repeatable proving that the nitrogen is very effective in returning the sensor back to its original response. The toluene exposure results in a close to a 60% change in the sensor current, relative to the nitrogen exposure characteristics. For the sensor in the previous experiment (Fig. 4.11), the toluene exposure resulted in a decrease in the sensor current, whereas for the sensor in this experiment, the observations are contrariwise. The sensors in both of these experiments were integrated with polypyrrole as the conducting polymer. However, the dopants used for the

synthesis of these films was different, pTSA in the first case and H₂SO₄ for the second. The polymer films from different dopants would normally be expected to have different physical and chemical properties [54].

The same sensor was subsequently exposed to methanol vapours and the measurement data was plotted in Fig. 4.13. For the methanol exposure experiment, the sensor was biased higher up in the subthreshold region; a greater voltage of 2.88 V. Unlike the other experiments, this time the sensor was initially kept under a saturated flow of methanol vapours (12.5%). After 20 minutes, the methanol flow was turned off. A direct flow of nitrogen was introduced and was seen to increase the current. The sensor current reached a saturated value under nitrogen 20 minutes after the methanol flow was turned off. After 50 minutes total time, the nitrogen bubbled through the methanol was turned back on. The sensor was observed to quickly

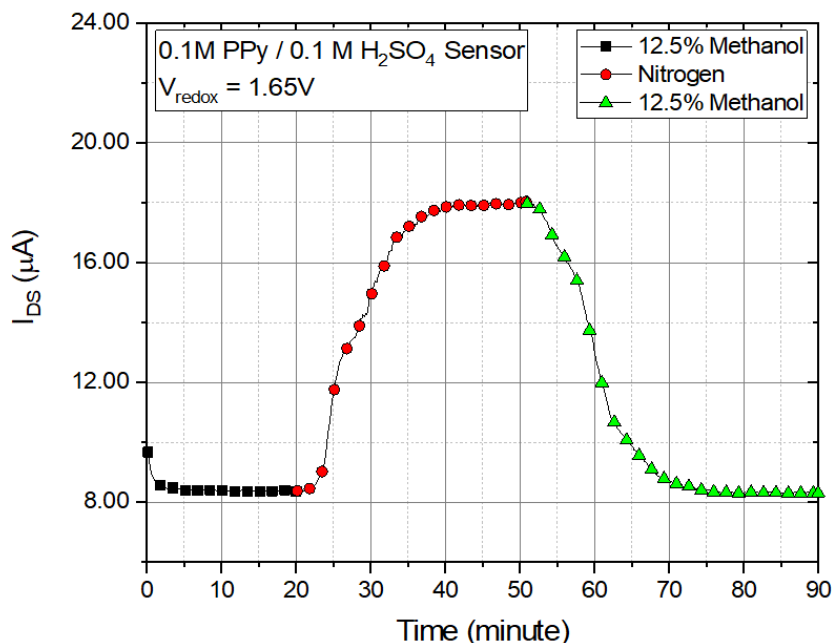


Fig. 4.13 Transient response of PPy/H₂SO₄ based sensor for exposure to methanol

respond to the methanol flow and it took 15 minutes of response time to return to the initial current value.

The PPy/H₂SO₄ integrated sensor was tested for continuous exposure to 4 different analytes with a nitrogen cycle between each of the different exposures. The analytes were exposed for 50 minutes of time followed by 50 minutes of pure nitrogen prior to exposure to a different analyte. For the nitrogen cycle, the bubbled flow of nitrogen through the analyte is turned off. The analyte from bubbler was removed, the bubbler was cleaned with DI water and dried with compressed dry air. The bubbler was now filled in with 20ml of next analyte under test and was carefully refitted into the gas flow setup. In Fig. 4.14 the data from this experiment is shown. It can be observed that the sensor had a unique sensitivity for all 4 analytes. Of the four analyte vapours, the sensor was most sensitive to methanol and least sensitive to ethanol. This experiment verifies that through the

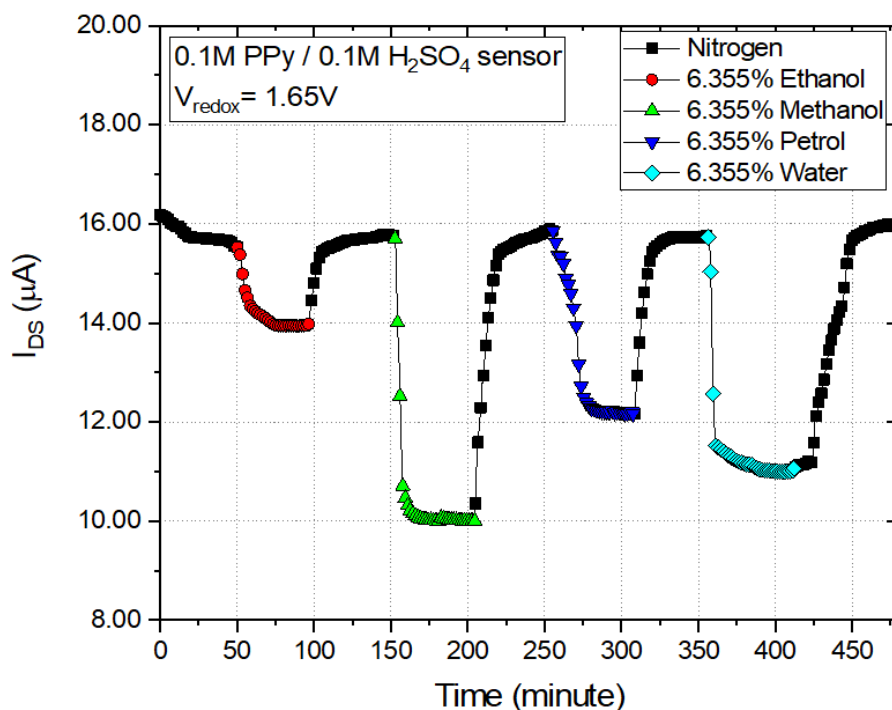


Fig. 4.14 Transient response of PPy/H₂SO₄ based sensor for exposure to 4 analytes

continuous testing of the sensor shows uniquely different responses to each of the analytes and recovering to baseline electrical characteristics upon exposure to nitrogen.

The next dopant that was used for the synthesis of a polypyrrole film was potassium chloride (KCl). The redox potential for the synthesis of this conducting polymer film was 1.56 V. The PPy / KCl polymer, an integrated sensor was tested for sensitivity to different concentrations of petrol. In Fig. 4.15, the data from this experiment is shown. As before, the sensor was initially kept under nitrogen environment for 20 minutes. It was then exposed to ~ 6.3 % relative flow of petrol vapours. This flow was maintained for the next 30 minutes. It was observed that the sensor current increased by almost a factor of 8 in less than 20 minutes where it reached a saturated current value. At the 50 minute mark, the direct nitrogen flow to the bubbled flow of nitrogen through analyte was recalibrated to set the petrol vapour concentration to ~ 5 %. The change in concentration of petrol vapours in the vapour chamber had a direct effect on the sensor current. The sensor current begins to fall as soon as the petrol concentration was lowered.

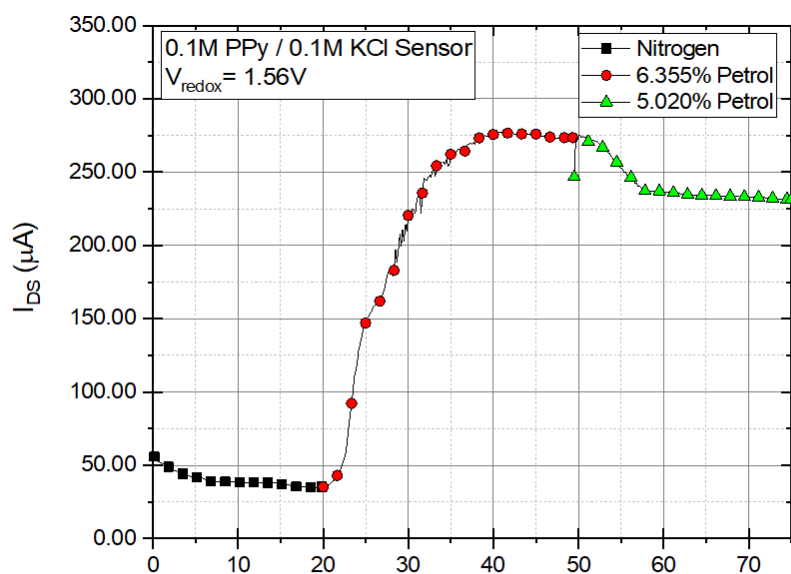


Fig. 4.15 Transient response of PPy/KCl based sensor for exposure to different concentration of petrol vapours

In another experiment involving testing for sensor sensitivity to a change in analyte concentration analyte is shown in Fig. 4.16. For this experiment, the conducting polymer film was synthesised at a redox potential of 1.25 V from an aqueous mixture of 0.1 M pyrrole monomer with 0.1 M oxalic acid in 20 ml DI water. The sensor integrated with this polymer was tested for water exposure at ~ 3 %, 6% and 13 % flow relative to the nitrogen flow giving a relative change in the current of approximately 5%, 9% and 14%, respectively. Once again, pure nitrogen flow was introduced between each change in the concentration. The sensor was also observed to respond significantly to the increasing concentration of water vapours in the test cavity. The polypyrrole film, which was doped with oxalic acid, had shown greater sensitivity to water when compared to the previously demonstrated PPy / pTSA and PPy /H₂SO₄ film-based sensors. In the next section, a similar set of experiments are described using the polyaniline conducting polymer-based sensors.

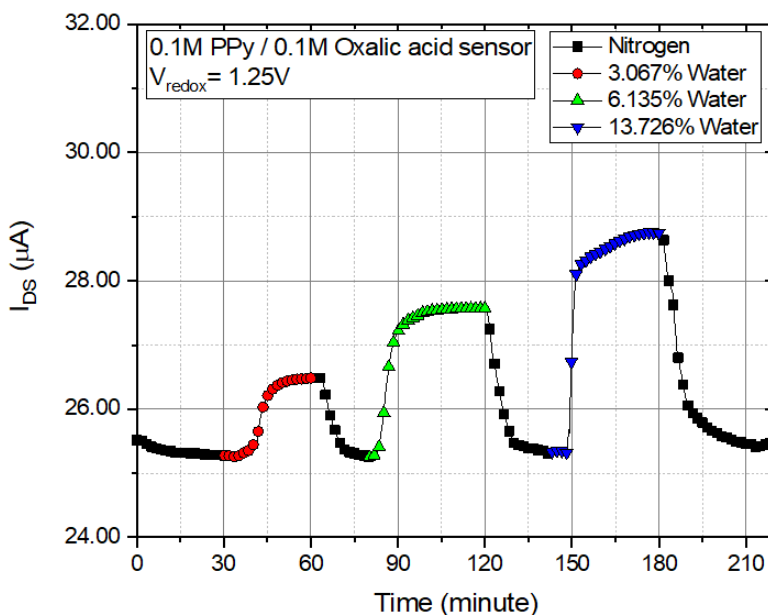


Fig. 4.16 Transient response of PPy/Oxalic acid based sensor for exposure to different concentration of water vapours

4.4.2 The polyaniline-based sensors

Polyaniline is one of the oldest known conjugated polymers which has been explored for a number of sensing applications [73]. The polyaniline (PANI) film for the following experiment was synthesized using 0.1 M aniline monomer doped with 0.1 M pTSA. The sensor was then tested with exposure to petrol and water. The measurements for both the analytes were performed individually. The data shown in Fig. 4.17 gives a summary of this experimental data. The sensor was initially kept under nitrogen flow for 60 minutes prior to exposure to the analytes. At the 60-minute mark of the first measurement cycle, the sensor was exposed to water vapours. As a result of this exposure, the sensor current was observed to increase for the next 18 minutes where it finally saturated. This change of sensor current was $\sim 22\%$. In the next measurement cycle, the sensor was exposed to petrol vapours after the initial nitrogen exposure. The petrol vapours were found to cause a reduction in the sensor current. This change was less, $\sim -6\%$, as compared to the exposure to water $\sim 22\%$.

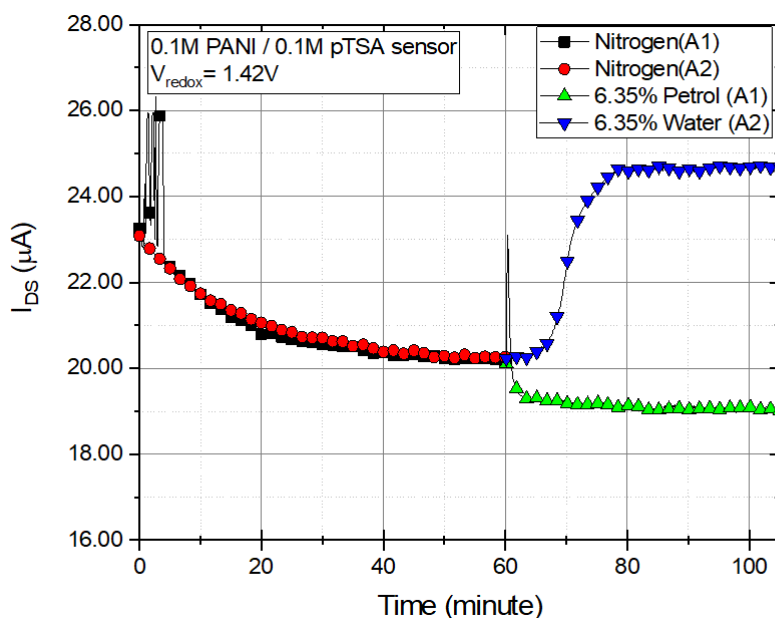


Fig. 4.17 Transient response of PANI/pTSA based sensor for exposure to water and petrol

The water vapour exposure test from the previous experiment was performed once again with different concentrations of water vapour. This data for this measurement is shown in Fig.4.18. The sensor was kept under a constant flow of 3.05% water vapour for 30 minutes. After this initial time interval, the measurements were started. The sensor remained under this flow of water vapour for 15 minutes. After 15 minutes the water vapour flow was increased to 6.35% water and kept constant for the next 40 minutes. This change was observed with a corresponding change in the sensor current of almost 16%. When the water vapour concentration was again increased to 13.72% at 55 minutes, the sensor current responded with a 62% increase. Following this, another experiment was performed using methanol vapours. Three different measurements were performed where the sensor was initially kept under nitrogen for 10 minutes and then exposed to different concentration of methanol vapours.

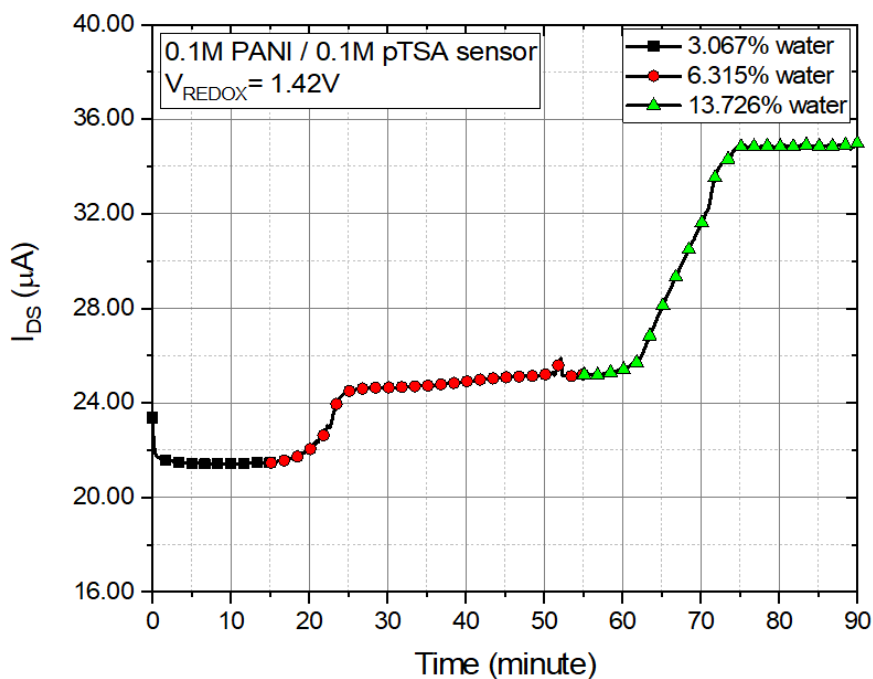


Fig. 4.18 Transient response of PANI/pTSA based sensor for exposure to different concentrations of water vapour

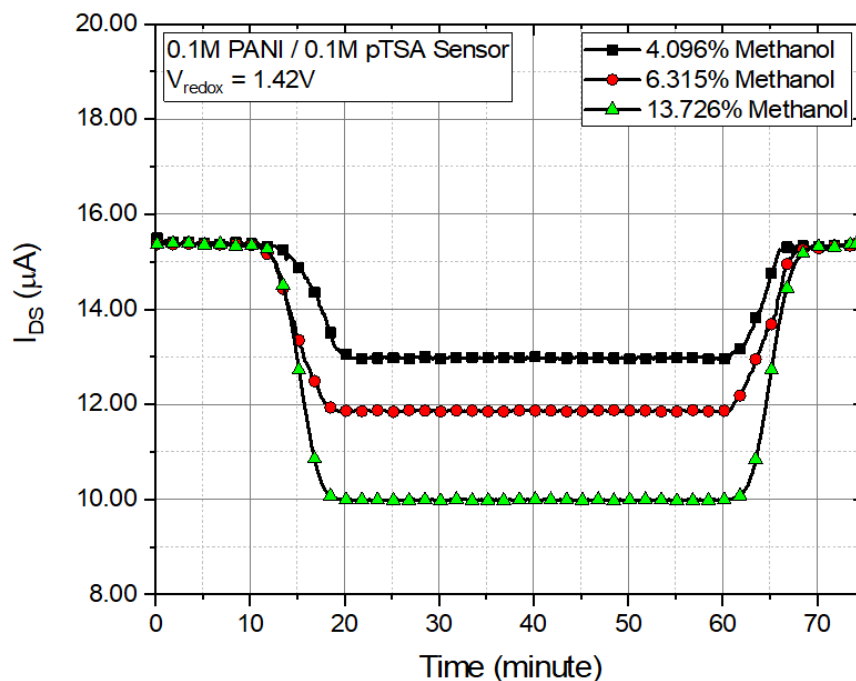


Fig. 4.19 Transient response of PANI/pTSA based sensor for exposure to different concentrations of methanol

The current response data plot for the PANI / pTSA sensor, when exposed to methanol concentration changes is shown in Fig.4.19. It can be observed that the sensor current decreases with increasing concentration of methanol. For concentrations of 4.1%, 6.3% and 13.7% methanol the observed saturated values of sensor current were 13 μA , 11.8 μA and 10 μA respectively while the base value for sensor current under nitrogen was 15.5 μA , giving a 16%, 24% and 36% change, respectively.

From the sensor transfer characteristics, it was observed that the PANI / H_2SO_4 films have the maximum sensitivity to water vapour when compared to the other test analytes. After gaining an understanding of the sensitivity of the different polymers to changes in analyte concentrations, a PANI / H_2SO_4 polymer-based sensor was tested for repeatability in a series of repeated cycles of nitrogen and water vapour, as shown in Fig. 4.20. It can be seen that the sensor

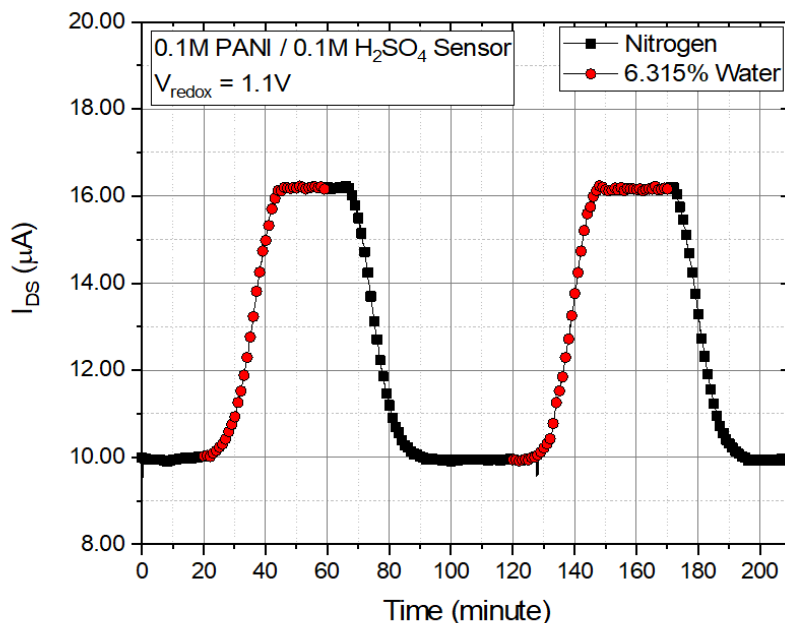


Fig. 4.20 Transient response of PANI/ H2SO4 based sensor for exposure to water vapour

was very sensitive to water vapour and produces a ~62 % rise in sensor current upon exposure. The refreshing effect of nitrogen can also be observed from this plot.

The six different polymer-based sensors have all shown sensitivity for different test analytes. The PPy and PANI films synthesised using different dopants have shown unique selectivity of the sensors for all of the tested analytes. The steady state response of the sensors was observed to be stable under the influence of each vapour analyte. To further understand the sensor repeatability and its ability to identify uniquely the different analytes, a set of experiments were performed where only the final saturated response of the sensors was measured for all of the films and of all of the analytes. As presented in the following section, this will be used for statistical analysis of the sensor data.

4.5 Sensor steady state response

The previous experiments were useful to understand the continuous time response of the sensors. The sensors, when introduced to analyte vapours, show an initial transient change in the sensor current. The sensor current attains a steady state magnitude after a given amount of time. The maximum transient time (response time) for an analyte influenced sensor (PPy/pTSA sensor for exposure to 7.6% petrol vapours) was observed to be ~40 minutes. The absolute change in the steady state sensor current and the response time of the sensor is mostly unique to any given analyte exposure to the sensors. These parameters can be used as the variables for an advanced data analysis study. A set of experiments, discussed in this section, were performed to investigate the steady state magnitude of the sensor response. First, the sensors were calibrated under a nitrogen environment for an hour and the measurements were recorded. In the next step, the sensors were subjected to a known concentration of an analyte vapour. The analyte vapour flow into the vapour chamber was maintained for 1 hour. After 1 hour, the sensor measurements were again recorded. These measurements were used to characterize the steady state, analyte sensing performance relative to nitrogen for each of the sensor/polymer device. The apparatus and measurement method are demonstrated using a specific experiment discussed in the following.

Two different sensors from the 4x4 sensor array of an unused chip were selectively addressed and coated with different PPy recipes. The pyrrole monomer was used in 0.1 M solution for both recipes. The PPy films were synthesised using 0.1 M concentrations of H₂SO₄ and oxalic acid dopants in 20 ml DI water. The polymer coated chip was carefully placed in the vapour chamber and was subjected to a uniform nitrogen flow. After 1 hour, the PPy / H₂SO₄ sensor was selectively addressed in the array and the sensor current was measured ($V_{CG} = 3.1$ V, $V_{DS} = 1$ V) over a 300 second interval using a sampling time of 1 measurement per second.

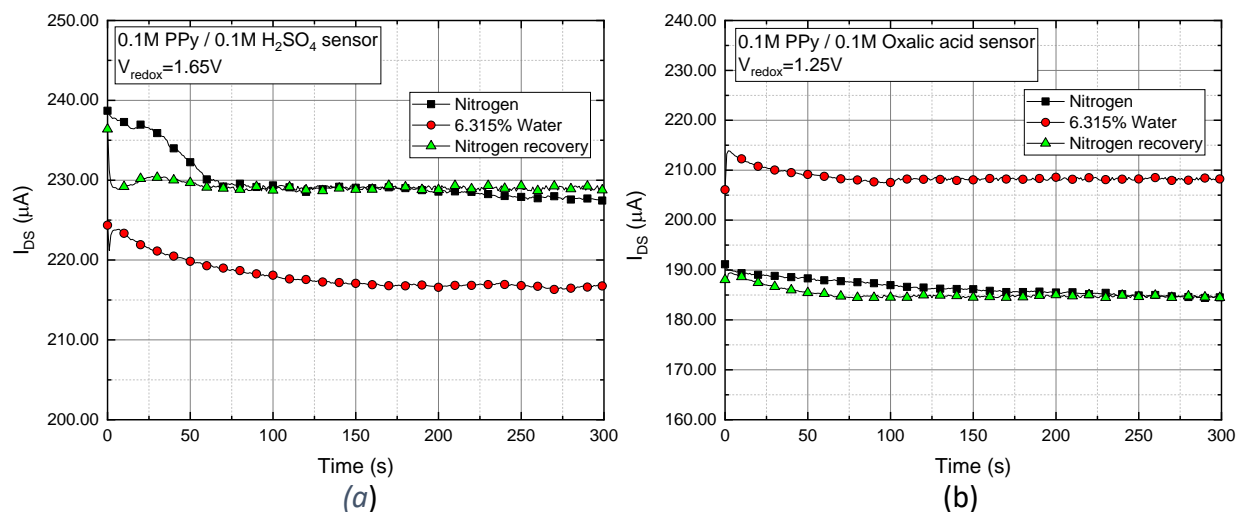


Fig. 4.21 Steady state response of PPy / H₂SO₄ and PPy / Oxalic acid sensor for exposure to water vapour

The same measurement process was repeated for the PPy / Oxalic sensor. After these measurements, the sensors were then exposed to a ~ 6.3 % relative flow of water vapours to nitrogen for 60 minutes. These measurements were then repeated for both of these sensors. The biasing conditions remained the same. The final measurements were performed after exposing the sensors to a nitrogen flow for 1 hour. The plots of Fig. 4.21 show the measured data. The long coaxial/triaxial cables, multiple jumper wires and different cable connectors used for setting up the measurements introduce significant resistive and reactive components to the test setup. These components are known to cause measurement delays. The 300 second time interval of the measurement allows sensors to reach the true steady state magnitude. An average of the last 100 data points of these measurements was used for comparative analysis.

The magnitude of the average sensor current for the PPy/H₂SO₄ sensor under nitrogen environment was observed to be 228 μ A. This average number reduced to a magnitude

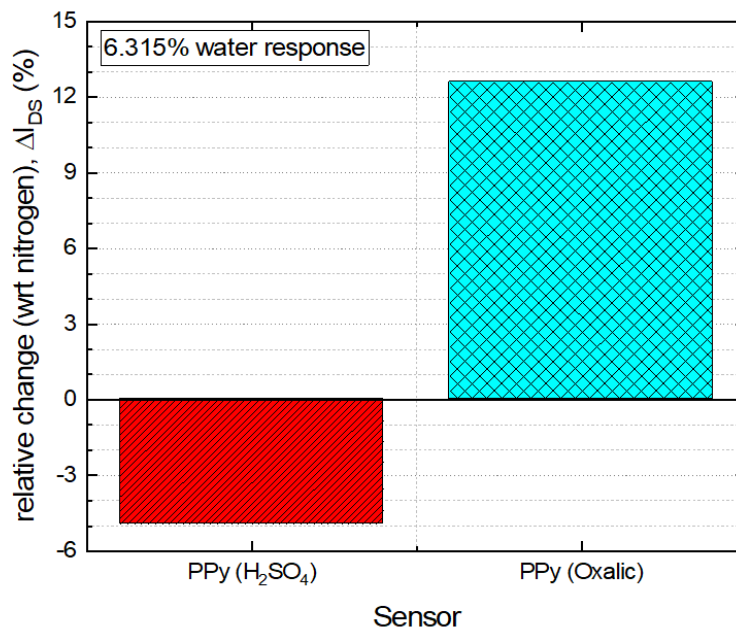


Fig. 4.22 Comparison of PPy/H₂SO₄ and PPy/Oxalic sensor response to 6.315% water vapour relative to nitrogen

of $\sim 216 \mu A$ upon an hour of water vapour exposure. Using these two numbers, the relative change to nitrogen was calculated to be $\sim -5\%$. Similar calculations were performed for the PPy/Oxalic sensor. The column plot shown in Fig. 4.22 gives a comparative view of the relative response of these two sensors. It can be observed that the sensor response was very different from each other at $\sim -5\%$ and 12% . This type of analysis simplified the data logging process which later proved helpful for advanced analysis. The visual distinction provided by the column plots made it easy to search for any pattern in the measurements as the number of sensors on the chip and the analytes under test increased.

Another similar study was performed on a different sensor of the same 4x4 sensor array. The sensor used for this study had a width to length ($\frac{W}{L}$) ratio of 20:1. This sensor was used for selective electrodeposition of PPy using 0.075 M pyrrole monomer and 0.1 M KCl dopant in 20 ml DI water. A 1.30V redox potential was used for electrodeposition of the polymer film. The

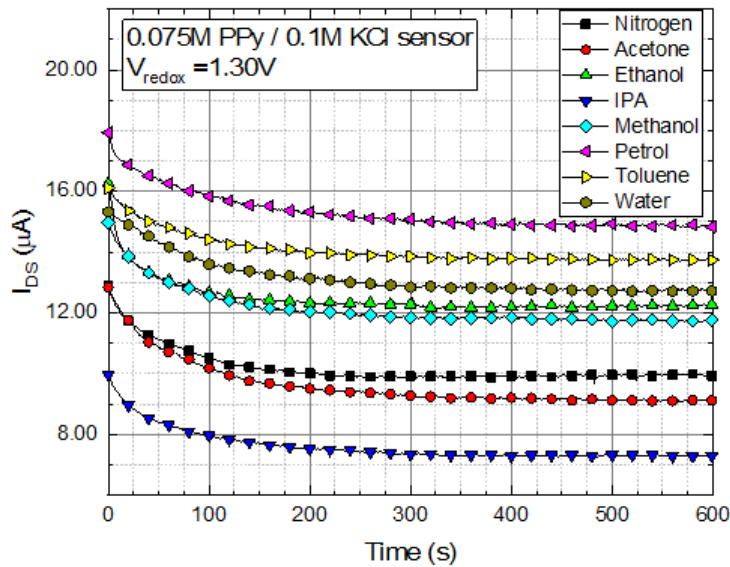


Fig. 4.23 Steady state response of PPy/KCl sensor for exposure to 7 different analytes

sensor was tested for exposure to 7 different analyte vapours; acetone, ethanol, IPA, methanol, petrol, toluene and water. The measurement approach was identical to the previous experiment. The sensor was biased at $V_{CG} = 3\text{ V}$ and $V_{DS} = 1\text{ V}$. An analyte vapour flow rate of 6.315 % was maintained. In Figure 4.23, a plot of the sensor current is shown. In this plot, a distinct sensor response to all the tested analytes can be seen. The data was again simplified by calculating the relative change to nitrogen and plotting them in a column graph, as shown in Fig. 4.24. The column plot presents a visible demonstration of the sensor's unique sensitivity towards the different analytes. The minimum sensitivity for this sensor was observed for acetone and the maximum for petrol vapours.

The previous two experiments verify that the approach adopted for the analyte exposure and measurement sequence was able to generate useful data which can be used to extract advanced information. Using this approach, the sensor response to different analytes can be easily verified and visualized as quantitative numbers on the column graph. It was very

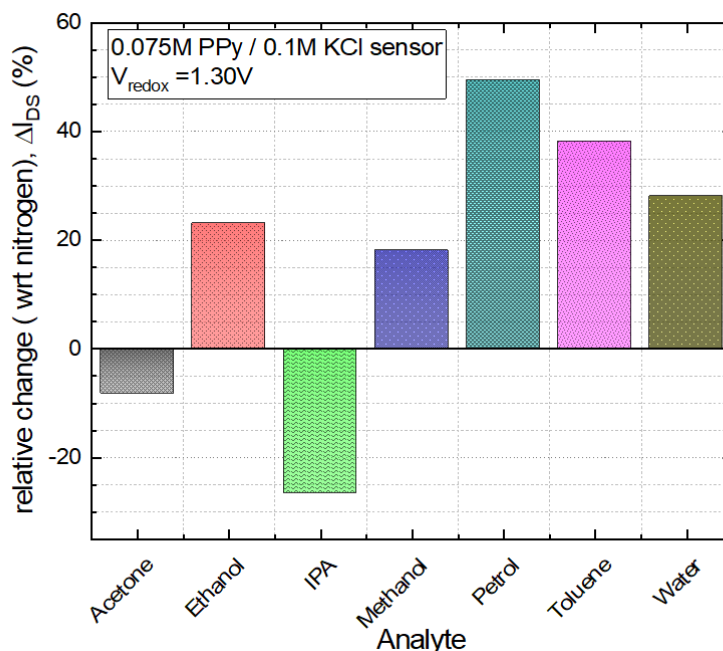


Fig. 4.24 Comparison of PPy/KCl sensor response to 6.315% flow of 7 different analyte vapours relative to nitrogen

important to test the individual sensor characteristics before connecting it to the other processing circuits on the chip.

Now that a reliable sensor operation was confirmed, the sensor was connected to the on-chip transimpedance amplifier. As discussed previously, the transimpedance amplifier on the chip was designed to translate the logarithmic nature of the sensor current to a linear voltage scale. For all the experiments hereafter discussed in this chapter, the system response parameter is the output voltage of the transimpedance amplifier.

The PANI sensors, doped with H_2SO_4 and pTSA, were observed to have a large sensitivity and unique selectivity towards a group of analytes. Two identical sensors from the 8x8 sensor array on the chip were selectively addressed and used for electrodeposition of these two polymer films. A 0.1M monomer and 0.1M dopant concentration in 20 ml DI water were used for the synthesis of both the polymer films. The sensors were kept in a nitrogen environment for 30

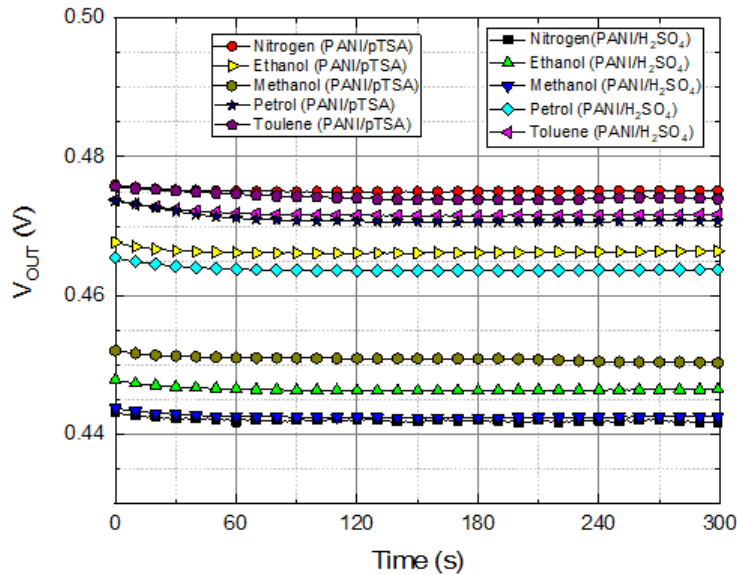


Fig. 4.25 Steady state response of PANI/H₂SO₄ and PANI/pTSA sensor for exposure to 4 different analytes and nitrogen

minutes or more and the transimpedance amplifier output (V_{OUT}) was measured for a control gate voltage, V_{CG} , of 3V. Both the sensors had a stable operation under the nitrogen environment. The sensors were then tested in a 6.3% relative flow of analyte vapours for 1 hour. After this time, the sensors were selectively addressed and the V_{OUT} measurements were performed again. This process was repeated for exposure to four different analyte vapours of ethanol, methanol, petrol and toluene. In Figure 4.25 a comparative plot of all these measurements is shown. An analysis of the plot reveals that the sensors had completely different responses for any of the tested analyte.

The differential calculations of the measurements revealed very useful information. For ethanol vapour exposure, the PANI/H₂SO₄ sensor had a relative average V_{OUT} change of -1.85% whereas, for the PANI/pTSA sensor, this change was observed to be 1.02%. Similar differences were observed for the other 3 analytes as well. Once again, a column graph for all the 4 analyte exposure cycles was plotted to ease the process of visual analysis. The column plot is shown in

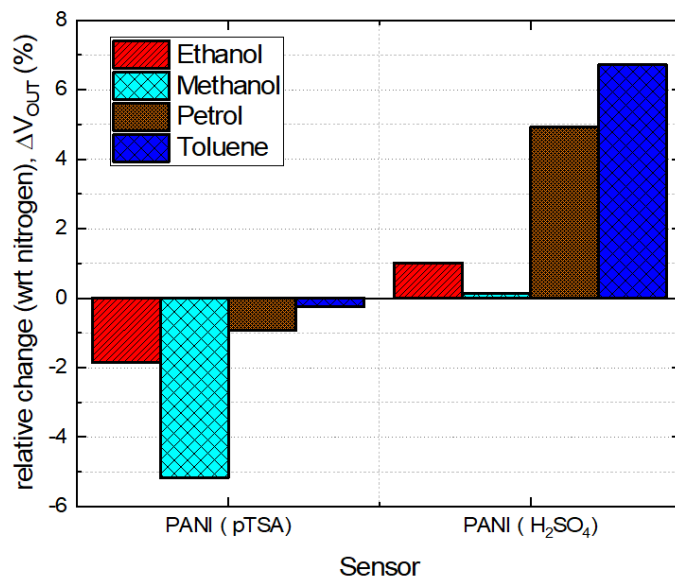


Fig. 4.26 Comparison of PANI/H₂SO₄ and PANI/pTSA sensor response to 6.315% flow of 4 different analyte vapours relative to nitrogen

Fig. 4.26. It can be observed that the PANI/H₂SO₄ sensor had a very weak response (0.13 %) to the methanol vapour and measurements were very close to nitrogen V_{OUT} levels. The PANI/pTSA sensor had a -5.17 % change for methanol vapours. The combination of these two observations was unique in the given set of 4 analyte vapours. Similar patterns can be observed from the column plot for the other three analytes. These combinational patterns highlight the importance of having multiple polymers on a single chip to ensure a reliable olfactory sensing operation. Such analyte influenced combinational patterns can work as a group signature, to enable the detection of an unknown analyte.

To test the true vapour detection capabilities of the system, the experiments required to have a greater number of polymers on the chip and exposure to multiple analytes. The experiments, discussed from hereon, were performed with the chips having at least three different polymer compositions and exposure to 6 or more analytes.

The next experiment was set up to have 3 different pyrrole films on a single chip. On this chip, the PPy films were selectively electrodeposited on 3 different sensors of the 4x4 array. The PPy films were synthesised using a 0.1 M concentration of pyrrole monomer. Sulfuric acid, oxalic acid and KCl were used as dopants in a 0.1 M concentration dissolved in 20ml DI water. The nitrogen and analyte exposure sequence and the measurement procedure were maintained as with the other experiments discussed in this section. The chip was subjected to exposure of 6.3% relative flow of 8 different analyte vapours of acetic acid, ethanol, IPA, methanol, NH₄OH, petrol, toluene and water. The steady state measurement plot of all the tested analytes is shown in Fig. 4.27. The plots show all the already discussed selectivity and sensitivity characteristics. With the increasing number of polymers and analytes, this type of plot becomes very dense and the visual analysis of raw measurement data becomes difficult. A much clearer,

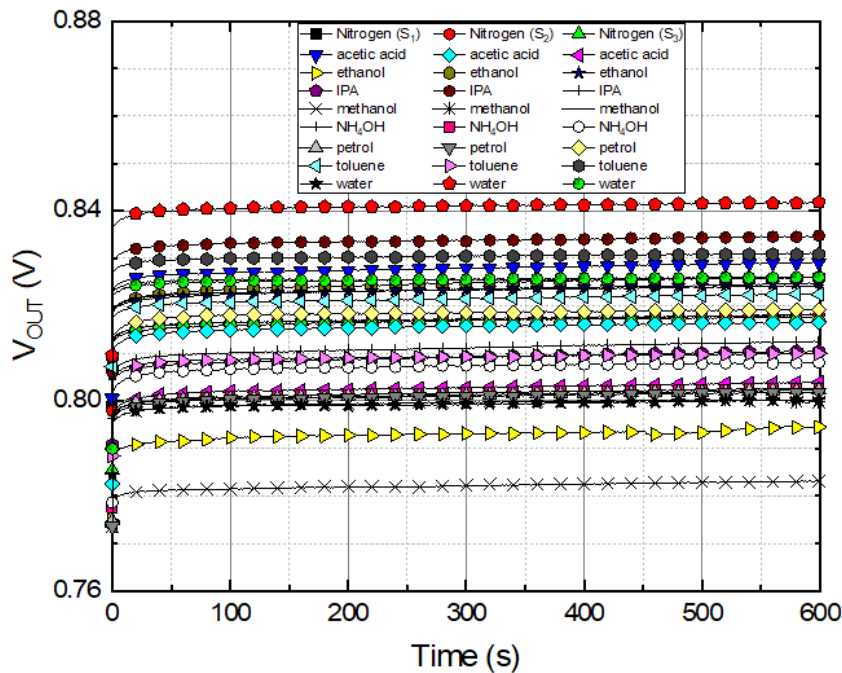


Fig. 4.27 Steady state response of PPy/H₂SO₄ (S₁), PPy/oxalic (S₂) and PPy/KCl (S₃) sensor for exposure to 6.315% flow of 8 different analytes and nitrogen

column plot of the data from this experiment is shown in Fig. 4.28. The column graph offers better readability with the increasing number of comparative measurement and henceforth only such plots are used to represent findings of the larger experiments. The PPy/H₂SO₄, PPy/oxalic and PPy/KCl sensors were represented as sensor S₁, S₂ and S₃ respectively in the plots shown above.

A single measurement cycle reveals the sensor characteristics towards any of the given analyte. When such measurements were repeated, at times, a small degree of error was observed in the measurements. This makes a recorded data log of multiple analyte exposure cycles essential for ‘training’ the chips towards detection of the vapour analytes. To demonstrate this, the given chip was again used for the analyte exposure experiment. All of the 8 analytes were again used for 2 cycles of analyte exposure measurements, where the analytes were exposed in a random sequence. This increases the total number of analyte exposure cycles to 24 and the total number of

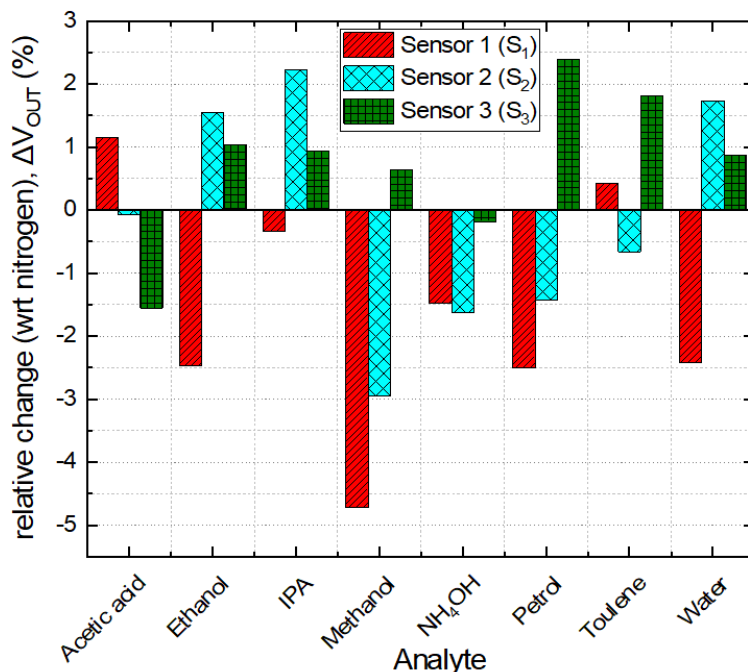


Fig. 4.28 Comparison of PPy/H₂SO₄ (S₁), PPy/oxalic (S₂) and PPy/KCl (S₃) sensor response to 6.315% flow of 8 different analyte vapours relative to nitrogen

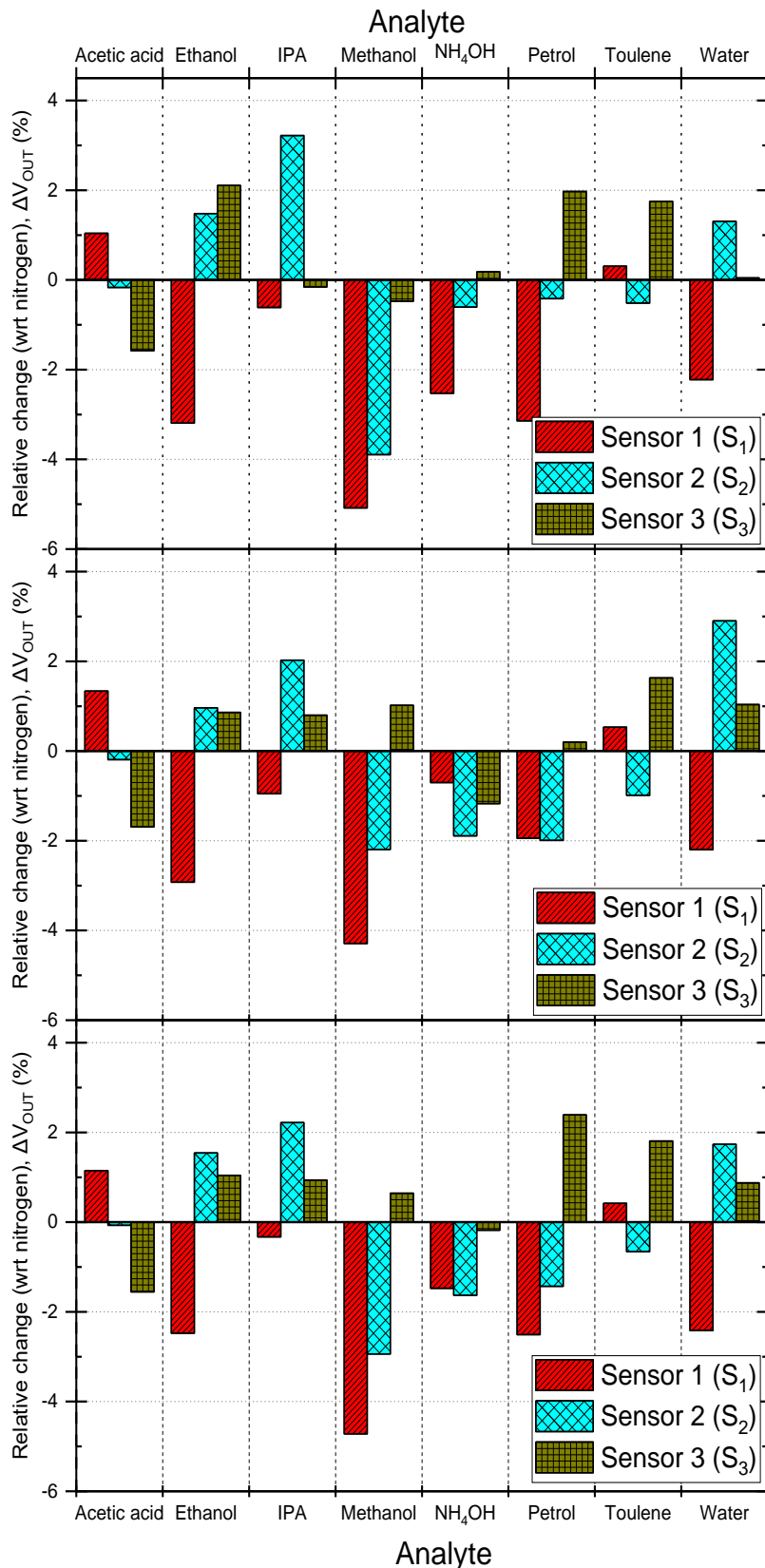


Fig. 4.29 Comparison of PPy/H₂SO₄ (S₁), PPy/oxalic (S₂) and PPy/KCl (S₃) sensor response to 6.315% flow of 8 different analyte vapours relative to nitrogen, 3 different sets of exposure

measurements cycles for the 3 sensors on the chip to 72. This combined information set is plotted in a column graph as shown in Fig. 4.29. The plot, although becoming very complex, can be used for quick initial assessment of the experiments. The information such as maximum and minimum sensitivity, similar response patterns can still be analysed upon close inspection. This method of analysis was effective to some extent but needs to be replaced with a better approach.

The increasing number of polymers, analyte and exposure cycles make the measurement data multidimensional. An advanced statistical analysis was required to extract useful information from the large dataset and represent the findings in a simplified manner. A statistical method of principal component analysis was used as an analysis tool.

The principal component analysis (PCA) technique is used to extract strong patterns in a dataset. This technique replaces the original variables of the dataset by weighed averages and thereby reduces redundancy[74]. The original dataset is transformed into new PCA dimensions called principal components. The newly extracted dimensions of the PCA domain are labelled using increasing integer numbers. The principal component 1 (PC1) holds the maximum information from the original dataset and the information sharing reduces with the increasing PC numbers. This leads to the lowest principal component dimension having the highest variance and so on. This means that a small subset of the lower order PCs contains large information contents of the original data.

The PCA was performed on the data shown in Fig. 4.29. A MATLAB program was developed and used to perform this analysis. The original data was arranged in the form of a numeric matrix, where the rows specified a single instance of exposure of the analyte under test and the columns were used to indicate the differential average response observed from different

sensors used in the given experiment. The present experiment had 8 analytes, each used for 3 different exposure cycles, and 3 different sensors. The numeric matrix of this experiment had a size of 24 rows and 3 columns. The MATLAB code transformed this data on to the principal component domain. The orthogonally projected data from the PCA was plotted on a 2-dimensional scatter plot by using the first 2 principal components, PC1 and PC2, as shown in Fig. 4.30. The measured dataset of the experiment was now projected as clusters of data points in the principal component domain. The analytes of acetic acid (triangle, black), ethanol (circle, red), IPA (square, green), NH_4OH (star, cyan), toluene (pentagon, yellow) and water (hexagon, taupe) were seen to have visibly distinct cluster of data points. The methanol (hexagon, blue) and petrol (inverted triangle, pink) showed overlapping of corresponding clusters. Upon close visual observation of Fig. 4.28, it was noticed that all the three polymer sensors on the chip had significant similarities

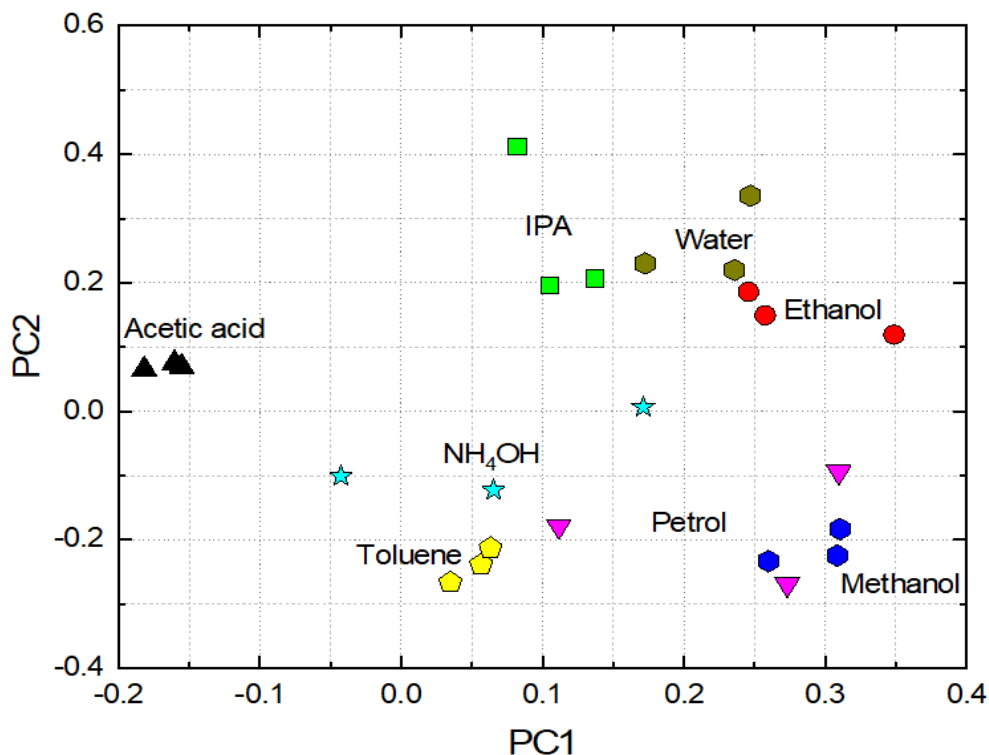


Fig. 4.30 Principal component analysis of PPy/ H_2SO_4 (S1), PPy/oxalic (S2) and PPy/KCl (S3) sensor response to 6.315% flow of 8 different analyte vapours relative to nitrogen, 3 different sets of exposure

in their response to the methanol and petrol analyte vapours. The addition of new diverse polymers onto the chip sensors should be useful to introduce a greater variance in the dataset and may also help to isolate the overlapping clusters.

A similar experiment was performed using PPy/H₂SO₄ (S₁), PPy/pTSA (S₂), PANI/H₂SO₄ (S₃) and PANI/pTSA (S₄) polymers, each integrated to a different sensor. The polymers were selectively electrodeposited onto 4 sensors of the 8x8 array. The sensors were initially calibrated under a nitrogen environment. Six different analytes were used for the exposure experiment. Each of these analytes was used for 3 random exposure cycles. The calculated V_{OUT} change relative to nitrogen, for all the 18 analyte exposure cycles, recorded individually for the 4 sensors under test is shown in the column graph of Fig. 4.31. The maximum change in the sensor response in both the positive and negative directions was observed for the PPy/pTSA (S₂) and PANI/pTSA (S₄) sensors when introduced to vapour analytes of petrol and methanol respectively. Several of these sensor response columns were observed to be very similar and were within 1% of the relative change parameter.

Once again, the statistical PCA was used to extract the signature patterns from this large dataset. The first two principal component domain variables, PC1 and PC2, were extracted using the MATLAB code. The data from this analysis is shown in the Fig. 4.32 wherein six (6) spatially separated, visibly distinct clusters are seen for all the six analytes. This confirms the differential sensitivity of the sensors to the given analytes. The first principal component successfully captures the spatial separation of four cluster groups. The range of $-0.4 < PC1 < -0.1$ highlights toluene, $-0.1 < PC1 < 0.05$ isolates ethanol, $0.05 < PC1 < 0.2$, IPA and $0.2 < PC1 < 0.45$ contains other remaining analytes. A similar analysis of the PC2 reveals three

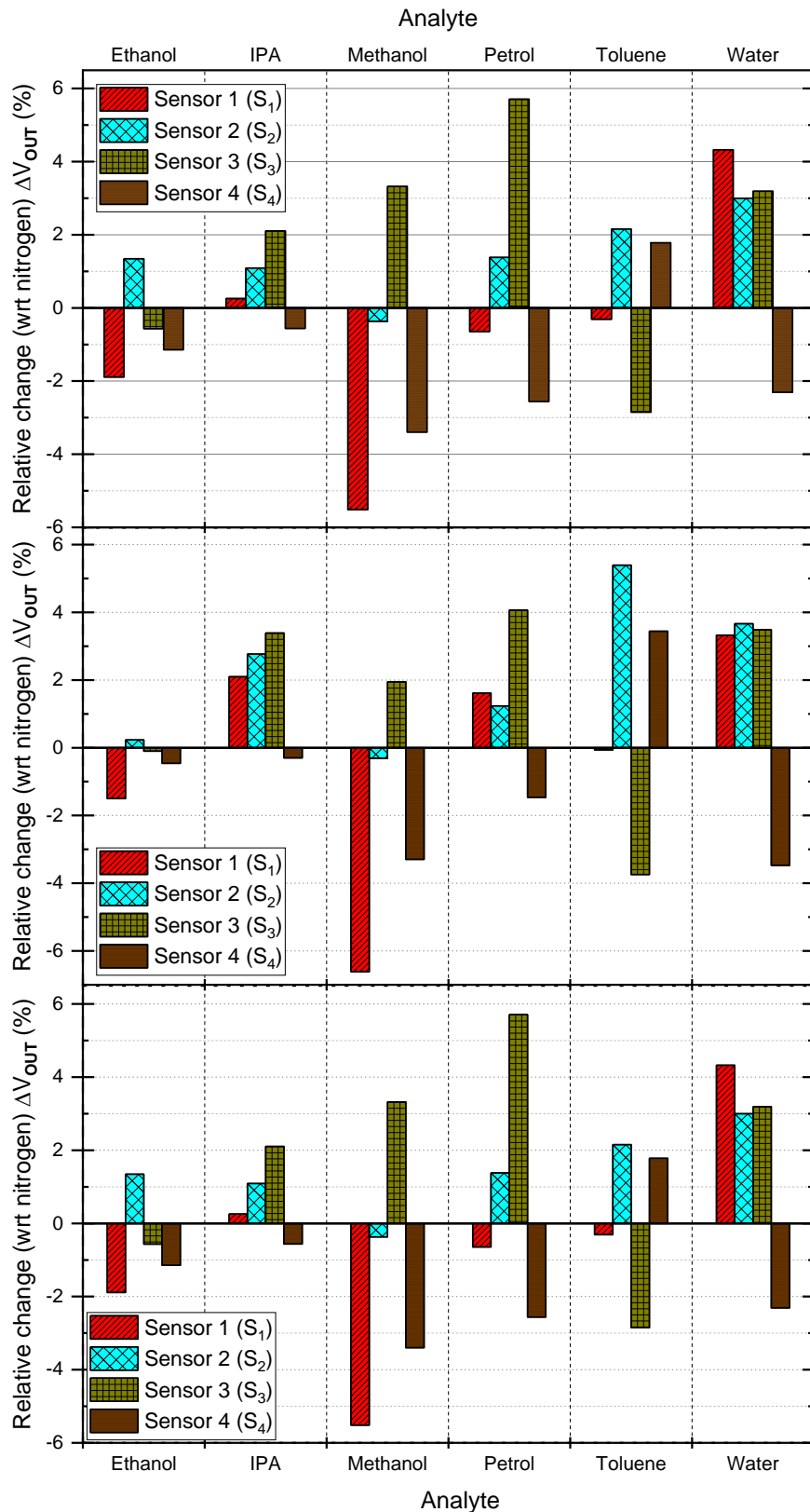


Fig. 4.31 Comparison of PPy/H₂SO₄ (S₁), PPy/pTSA (S₂), PANI/ H₂SO₄ (S₃) and PANI/pTSA (S₄) sensor response to 6.315% flow of 6 different analyte vapours relative to nitrogen, 3 different sets of exposure

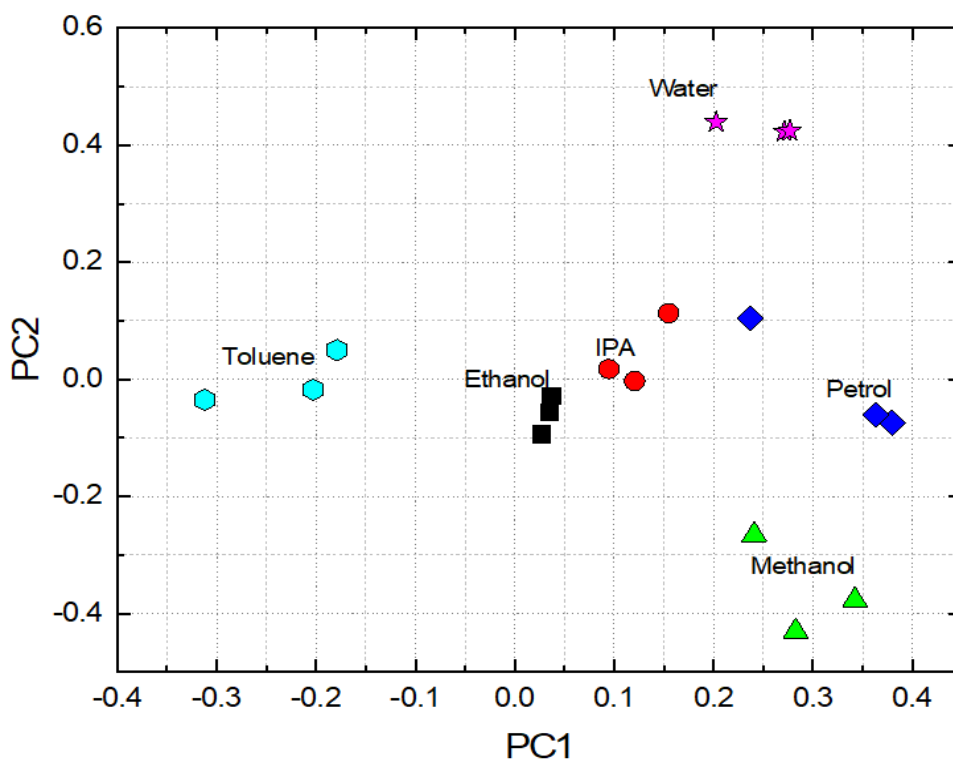


Fig. 4.32 Principal component analysis PPy/H₂SO₄ (S1), PPy/pTSA (S2), PANI/ H₂SO₄ (S3) and PANI/pTSA (S4) sensor response to 6.315% flow of 6 different analyte vapours relative to nitrogen, 3 different sets of exposure

such groups of isolated clusters. Both principal components, when combined, present the cluster information with a very easy visible distinction.

The previous two studies show that the PCA analysis proved to be very useful in highlighting isolated groups of data points, each linked to a given analyte under test. The large dataset of such multiple sensors / multiple exposures experiments would be very useful for ‘training’ the system for detection of any unknown exposure of an analyte from the given set of analytes. The next experiment was performed with PPy, PANI sensors having H₂SO₄ as a dopant and another PPy sensor with oxalic acid as the polymer dopant. The pyrrole and aniline monomers were used in 0.075 M and 0.07 M concentration, respectively. The dopants were used in a 0.1M

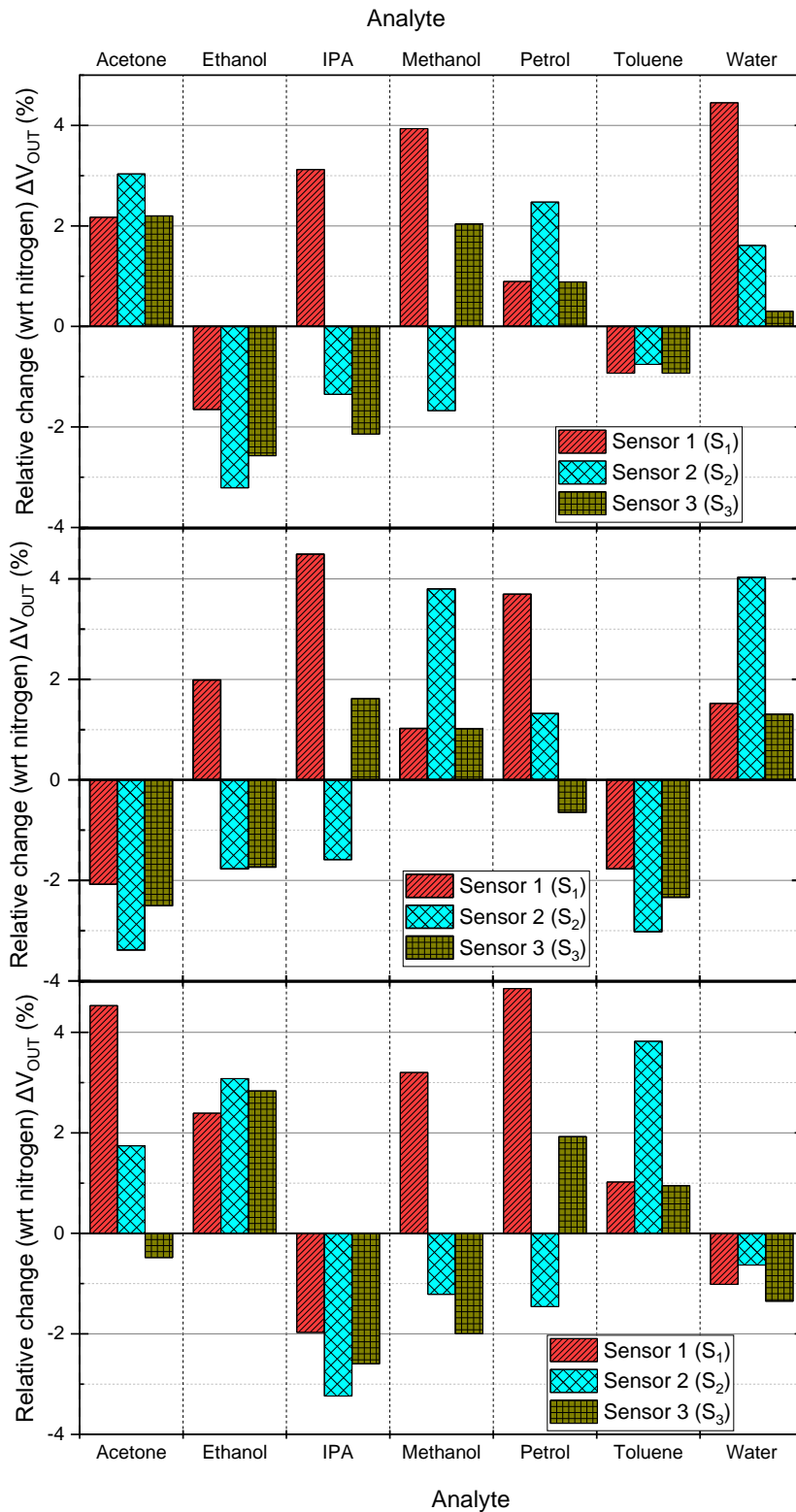


Fig. 4.33 Comparison of PPy/H₂SO₄ (S_1), PANI/ H₂SO₄ (S_2) and PPy/oxalic (S_3) sensor response to 6.315% flow of 7 different analyte vapours relative to nitrogen, 3 different sets of exposure cycles

concentration in 20 ml DI water for the synthesis of the polymer films. The chip was tested for exposure to 7 different analytes of acetone, ethanol, IPA, methanol, petrol, toluene and water. Every analyte was used for 3 different exposure cycles. The total number of exposure cycles was 21. The dataset generated from this experiment, as a V_{OUT} percentage change to nitrogen, is shown in Fig. 4.33. Of the 7 test analytes used in this experiment, 3 analytes were randomly chosen for an additional exposure cycle and the measurements were recorded. The analytes were used from the labelled storage bottles. To keep the information of these analytes concealed, the measurement files of the given analyte exposure experiments were named using random alphabets. The measurements were processed for calculation of the relative response to nitrogen and were appended to the primary data log of the experiment. The complete dataset, 21 initial exposures and

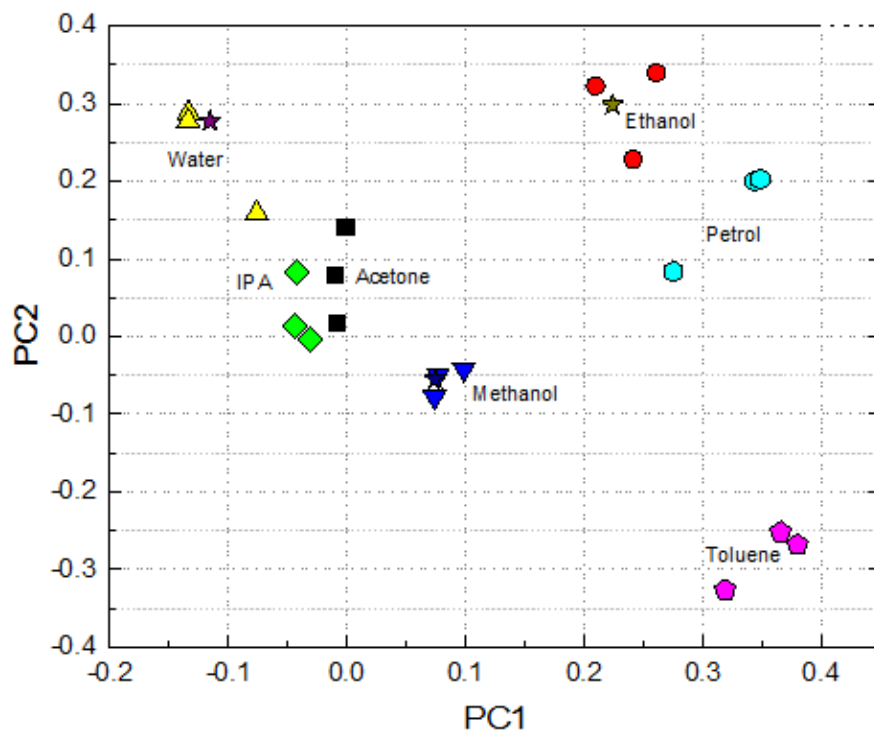


Fig. 4.34 Principal component analysis of PPy/H₂SO₄ (S1), PANI/H₂SO₄ (S2) and PPy/oxalic (S3) sensor response to 6.315% flow of 7 different analyte vapours relative to nitrogen, 3 different sets of exposure cycles

3 additional exposures, was used for PCA. The plot shown in Fig. 4.34 shows 7 different clusters corresponding to each of the analytes. In the PCA plot, a 'star' symbol was used to highlight the additional exposures of the 'unknown' analytes. It can be observed that the 'star' symbol used for the representation of the 'unknown' analytes were correctly plotted in the data point clusters of ethanol, methanol and water. This experiment successfully demonstrates an approach which can be used for detection of unknown analytes. Greater number of polymers on the chip, large measurement dataset for training the system and advanced statistical analysis would make the detection process very accurate.

Chapter 5 – Discussions, conclusion, and future work

The previous chapters describe the design of the floating gate MOS sensor, the sensor array system, post processing and polymer electrodeposition procedures, experimental setups, and gas sensing performance of the chip. The sensing experiments highlighted the selectivity and sensitivity of different polymer-based sensors to multiple vapour analytes. The polymer film functioned as an active layer for the detection of vapour analytes and the FG MOS sensor worked as a transducer to generate an effective electrical change. The analyte influenced change in sensor electrical performance was observed to be reversible upon exposure to pure nitrogen flow. In this section, a discussion on the interaction of some of the vapour analytes and their effect on the sensor operation is presented.

5.1 Discussion on polymer sensing mechanism

The sensing polymers are made up of hydrocarbon-based monomer molecules. The structure of end-to-end connected monomer network define the electrical characteristics of the polymer. The neutral state structure of polypyrrole and polyaniline conducting polymers is shown in Fig. 5.1. The conjugated structure of monomer chain having alternate single and double bonds make these polymers intrinsically conducting polymers. The single bonds are sigma bonds where electrons are localized between atoms. The double bonds, π -bonds, have significant overlapping of their bonding orbits instigating delocalized electrons and contributing to charge mobility in the polymer chain [75]. The electrical properties of these polymers can be modified with the introduction of dopants into the polymer chain. The dopants change the structure of the polymer chain by addition or removal of electrons from π -bonds of the conjugated chain network. Removal or addition of electrons is due to oxidation or reduction, respectively, of the polymer by the dopant

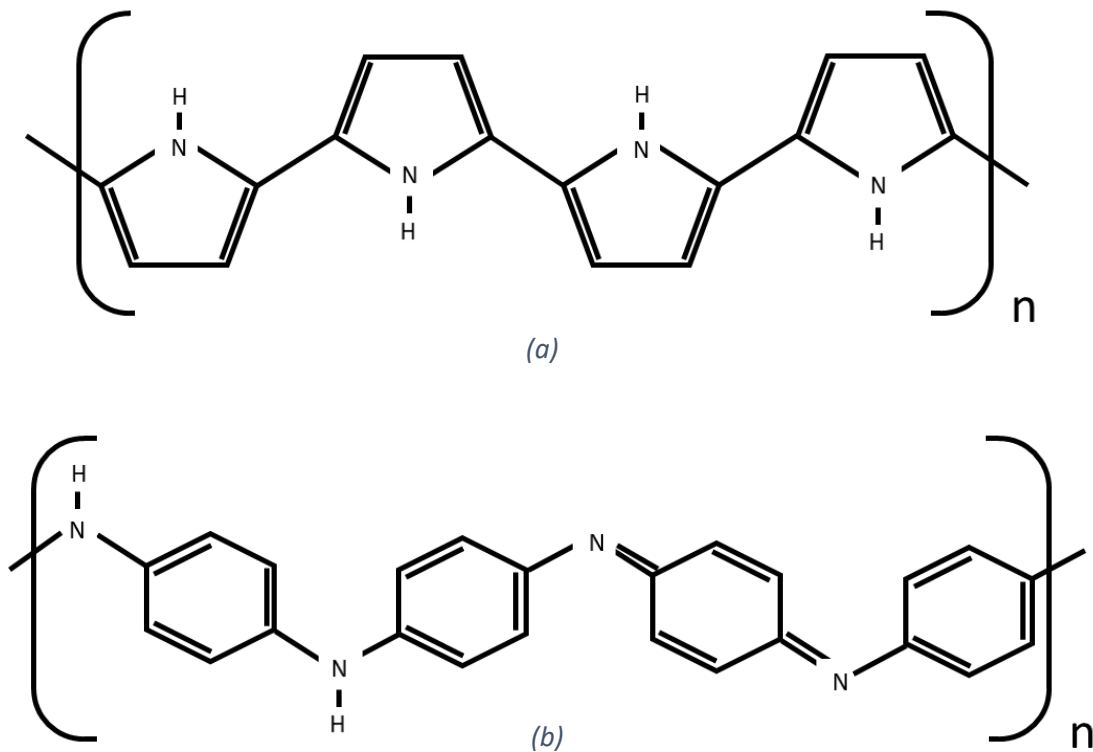


Fig. 5.1 Typical structure of (a) polypyrrole and (b) polyaniline conducting polymers in their intrinsic state

molecules. In an electrochemical synthesis of these conducting polymers, polymer growth and doping occur simultaneously which is controlled using the electrical potential of the working electrode [76][77]. The process of doping conducting polymers is a redox reaction rather than an addition of impurities to the polymer structure.

The doping redox reactions that generate delocalized charge carriers in the polymer chain also result in the formation of counterions on the polymer backbone to maintain charge neutrality. The counterions are confined charge and do not contribute to the polymer conductivity. The counterions create localized energy states in the polymer which results in lattice distortion in the polymer chain. This lattice deformation coupled to charge results in formations of quasi particles known as polarons and bipolarons. The polarons and bipolarons introduce new polaronic

energy states between the conduction and valence bands of the polymer [77]. The new energy states impart increased electrical conductivity to the doped conducting polymers.

Conducting polymers used in this work were synthesised using different dopant compounds. Doping introduces physical and chemical diversity in the polymers enabling their differential response to different vapour analytes [54]. Doping of polymers affects the charge transfer mechanism between the polymers and analyte vapours and introduces differential sensitivity [46]. Figure 5.2 shows the oxidation reaction of the neutral state of polypyrrole (PPy) to generate a polaronic state of the polymer. The oxidation of PPy, by the means of electrochemical reaction with the dopant, removes electrons from the polymer backbone and generates a positive charge. This charge is balanced by counterion, X^- , induced close to the polymer chain. Further oxidation and removal of electrons from the polymer backbone creates a quasi state of the bipolaron which further enhances the polymer conductivity. The doping of conducting polymers

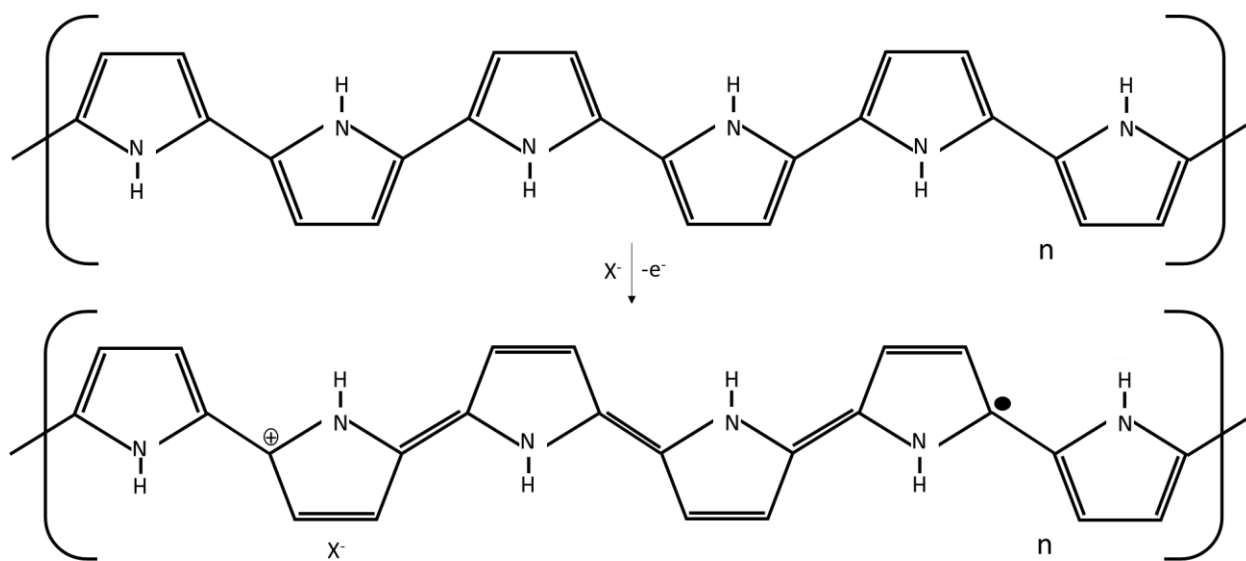


Fig. 5.2 Mechanism of polaron formation on polypyrrole backbone through oxidation doping

is a reversible process. The oxidized polymer, upon exposure to reducing agents, can be brought back to its initial state through the process of chemical reduction [51][78].

Many theories, explaining different mechanisms of interaction of the conducting polymer films with different vapour analytes, have been reported. This primarily includes studies on change in the physical properties of the polymer because of the absorption/adsorption of analyte vapours [46][78]. The large experimental set of this work, which includes many different polymers, dopants and vapour analyte combinations, make it difficult to analyse every exposure experiment and investigate every possible interaction mechanism. The following discussion highlights some of the chemical interactions to explain the transduction mechanism of the sensor operation.

The doped conducting polymers when exposed to vapour analytes experience a change in their doping levels through chemical reactions between the polymer and analyte molecules. This causes a change in the charge density of the polymer. The vapour analytes can also be considered as secondary dopants of the polymer [51]. Any change in charge density of the polymer is electrically coupled with the floating gate of the sensor. This change modulates the electric field originating from the control gate and modifies the charge density of the channel in the substrate. The variations in substrate channel charge are directly observed in the threshold voltage and the source-drain current of the sensor. The sensitivity of the sensor would be dependent on the number of the reaction sites in the polymer and the polymer's affinity towards the analyte under test. In the case of vapour analytes, that cause a chemical reduction of the polymer by donating electrons to the polymer, the charge coupled to the floating gate will oppose to the electrical field between the control gate and the channel of the n type FG MOS sensor. This will

cause a decrease in the charge density in the channel and the threshold voltage of the device should increase. The opposite effect is anticipated for oxidizing vapour analytes.

The sensors based on polypyrrole (PPy) and polyaniline (PANI) conducting polymer films have shown specific response towards multiple different analytes. The effect of the addition of different dopants to the polymer on the sensor threshold voltage was shown in Fig. 4.9. This figure showed a comparative representation of the threshold voltage variations as observed in different sensors for exposure to six different analytes. These sensors were integrated to PPy and PANI films synthesised using different dopants. The PANI films in this work were prepared using two different dopants of sulfuric acid and pTSA. The film doped with sulfuric acid has shown stronger sensitivity for water as compared to the pTSA doped film. The PANI films with different dopants were reported to have a sensitivity to water vapours which is known to be a proton donor for the aniline chain [46]. Sulfuric acid is a stronger acid compared to pTSA. The higher sensitivity of the sulfuric acid doped PANI film-based sensor can be a result of the sulfuric acid being a stronger oxidizing agent which in turn creates a greater number of reactions sites in the polymer film.

The PPy films using different dopants have also shown a unique sensitivity to different vapour analytes. The p-type structure of polypyrrole film experiences a decrease in electrical conductivity when exposed to analyte vapours that can donate electrons. In case of the sensor operation, additional electrons on the floating gate will generate a repulsive force for the electrons in the channel. This effect is observed as an increase in the threshold voltage of the sensor. The sulfuric acid doped PPy sensor experienced an increase in the threshold voltage for exposures to five different vapour analytes including ethanol, IPA, methanol, petrol and water. Most of these analytes have been reported as reducing agents and as such have electron donating

properties [79]. Methanol was observed to produce the greatest change in the threshold voltage of the PPy/H₂SO₄ sensor. This can be attributed to the stronger reducing property of methanol as compared to the other analytes used in the experiment. The differential sensitivity of the PPy/oxalic acid sensor as compared to the PPy/H₂SO₄ sensor can be due to large differences in their oxidizing strengths. The working electrode potential of the polymer impacts the oxidation state of the polymer and will cause a noticeable change in sensing properties of the polymer films[54]. The variations in the threshold voltage due to the charge coupled to the floating gate was examined in section 4.3. The overall sensitivity of the polymer and hence the sensor is dependent on multiple different factors. The broad chemistry of polymer analyte interaction was not studied in this work. The research was more focused towards the development and optimization of sensor array system including the methodology of polymer integration, experimental setups and advanced analysis of the system response.

5.2 Conclusion

This research work began with an objective to develop an electronic olfactory system using commercially available silicon technology and gas sensitive conducting polymers. The FGMOS sensor was designed and optimized on the 350 nm technology node from TSMC. The electronic system containing an array of these sensors was developed with the required addressing, control and signal processing circuitry all designed on the same chip. Different vapour sensing conducting polymers were successfully integrated onto the sensor array chip. The polymer functionalized chips were electrically characterized under the influence of different vapour analytes. The mostly unique electrical response of the polymer functionalized sensor array system demonstrated the feasibility of the array system for the purpose of vapour analyte detection. The nitrogen assisted recovery of the sensors is very useful for detection of multiple exposure cycles

and longer operation life of the sensors. Up to six different polymers were functionalized on a single chip and the sensing experiments involved nine different vapour analytes. The sensor operation was repeatable for sensors on any given chip. There were instances of having noticeable change in the sensor performances for sensors on different chips, even when integrated to similar polymers and exposure to a given analyte. Such variations can be due multiple different factors such as, the silicon process variations in the semiconductor technology, any unintentional change in any of the factors controlling the electrodeposition process (dopant concentration, working electrode potential, polymer thickness etc.), or the sequence in which multiple polymers were deposited. In case of deposition of multiple polymers on the same chip, there is suspicion that the chemicals in a given polymer recipe may interact with other already existing polymers on the chip and modify their sensing properties. The sensor performance variation observations, although rare, needs further investigation. The analyte “training” of the chips accounts for the variations and enables accurate detection of analytes using the statistical approach.

The compatibility issue of electrodeposition of conducting polymers on to the aluminum surface of the sensing area on the chip was resolved by developing a 3 stage electroless plating technique. In this technique, a process of electroless gold deposition was developed to coat the extended floating gate pads of the FGMOS sensors using subsequent electroless plating of zinc, nickel and then gold layers. The electroless gold deposition process developed and demonstrated in this work, on a small microelectronics chip, can be adopted by other research groups to solve the issues related to the native oxide layer on the aluminum surface. This cyanide free process provides a safe and effective way for mass processing of samples for gold depositions. This process successfully facilitated electrodeposition of polymer films onto the gold-plated extended floating gate pads. The depositions of these metal films were confirmed using energy dispersive x-ray

spectroscopy (EDS) and optical microscope imaging. The bond wires from the chip to the ceramic package were encapsulated using SU-8 photoresist to avoid undesired electrodeposition of the polymers onto the gold wirebonds. Electrodeposition the polymers was done successfully on individual sensors as well as on the sensors in the array. The sensors in the array were selectively coated for different chemically diverse polymer films.

A special vapour flow setup was created that contained a controlled test environment for exposure of the sensors to the vapour analytes. The polymer coated sensor was tested for different analytes including acetone, acetic acid, ammonium hydroxide, ethanol, isopropyl alcohol, methanol, petrol, toluene and water. The sensor system produced unique electrical responses for each analyte and for different concentrations of analyte vapour. The dataset from different analyte exposure experiments was used for the advanced statistical method of principal component analysis (PCA). The PCA study showed that the analytes from any multiple random order analyte exposure experiment can be separated as clusters of data points in the principal component domain. One such experimental dataset was analysed to demonstrate a methodology for the detection of unknown analytes.

The major contribution of this research work to the field of microelectronic sensing system is its electronic design and the very concept of using this platform for sensing applications. The silicon “chips” were designed as a platform such that any electrochemically deposited sensing material may be used making the sensor array “effectively programmable” for any groups of volatile molecules from different domains of applications. This platform has the potential to be used for development of robust sensing systems targeting different applications. The sensing materials can be designed to have a specific sensitivity to different analytes. This has an advantage that the designed electrical system can be used as a platform for applications in multiple different

industries that include food production, agriculture, cosmetic, wine and spirit production, automobiles and even defence. Given that these chips are fabricated using a commercial silicon CMOS technology, it would be economical to fabricate in mass production. The silicon chip can be easily redesigned to have a larger array of sensors to facilitate a greater number of chemically diverse sensing materials in applications where superior sensitivity is desired. A combined response from a large array would enable better use of statistical (pattern recognition, signature analysis, principal component etc.) and even learning algorithms to accurately predict very complex analyte information. Such a system would be applicable in many different applications.

5.3 Future Work

The sensor array chip, designed and fabricated in this work, has been lab tested and verified for its functionality to a group of vapour analytes. The work can now progress with advanced experiments that involve testing the system response for exposure to a known mixture of different analytes. This would be helpful to plan and prepare for the chip usage in the industrial applications where the sensing environment usually has multiple different vapours. This should be followed with testing the sensor chip performance for some specific industrial application, for example, monitoring of fermentation in winemaking. A prior study of the sensitivity of the conducting polymer in the given selected application would be helpful for the selection of polymers with maximum sensitivity to be electrodeposited on the chip.

The chip in this work has 64 FGMOS sensors in its largest sensor array. The present work had far fewer numbers of conducting polymers deposited on the chip. The decision to include a number of chemically diverse polymers should be dependent considering the application requirements. This work can progress in close collaboration with the chemistry group so as to test and decide the optimal combination of polymers for any given application. Larger sensor arrays

with a greater number of sensors can be designed for the cases where more than 64 chemically diverse polymers are expected on the chip. This will enable a truly chemically diverse sensor array for the selected application.

Other silicon technologies for the design of this olfactory system can also be explored, with the sensor design carefully adapted to the given technology rules. The advanced low power CMOS technologies that operate on lower electrical fields would be interesting to investigate if they are able to produce higher sensitivities for a similar sensor array system. Some of these technologies offer gold studs on the top metal contact surface. This can be explored to check if such gold studs would be directly compatible for polymer electrodeposition on direct off the foundry chips, eliminating the requirement of metal stack electroless depositions. Advanced customized packaging options can also be explored to eliminate all the post processing steps required before the electrodeposition of the polymers. For example, a die on board type of packaging can be considered on specially designed two layer printed circuit boards (PCB) where one side of the PCB is completely given to the chip mounting and the other side used for making the electrical connections. This can make chips completely portable without the need for mounting setups. Work can be done to research different data processing algorithms and improve the analyte discrimination and classification process. The interdisciplinary nature of this research has potential for future graduate students to research and further develop the sensor array system with new and promising conducting polymers tailored for different applications.

References

- [1] L. Buck and R. Axel, “A novel multigene family may encode odorant receptors: A molecular basis for odor recognition,” *Cell*, vol. 65, no. 1, pp. 175–187, Apr. 1991, doi: 10.1016/0092-8674(91)90418-X.
- [2] L. B. Buck and W. P. T. James, “Olfactory receptors and odor coding in mammals,” *Nutr. Rev.*, vol. 62, no. 11 SUPPL., 2004, doi: 10.1301/nr.2004.nov.S184-S188.
- [3] T. Wasilewski, J. Gębicki, and W. Kamysz, “Bioelectronic nose: Current status and perspectives,” *Biosens. Bioelectron.*, vol. 87, pp. 480–494, 2017, doi: 10.1016/j.bios.2016.08.080.
- [4] H. Nazemi, A. Joseph, J. Park, and A. Emadi, “Advanced micro-and nano-gas sensor technology: A review,” *Sensors (Switzerland)*, vol. 19, no. 6, 2019, doi: 10.3390/s19061285.
- [5] S. Feng *et al.*, “Review on Smart Gas Sensing Technology,” *Sensors*, vol. 19, no. 17, p. 3760, Aug. 2019, doi: 10.3390/s19173760.
- [6] M. S. Freund and N. S. Lewis, “A chemically diverse conducting polymer-based ‘electronic nose,’” *Proc. Natl. Acad. Sci. U. S. A.*, vol. 92, no. 7, pp. 2652–2656, 1995, doi: 10.1073/pnas.92.7.2652.
- [7] A. A. Iyogun, D. A. Buchanan, and M. S. Freund, “Analyte discrimination with chemically diverse sensor array based on electrocopolymerized pyrrole and vinyl derivatives,” *RSC Adv.*, vol. 6, no. 39, pp. 32549–32559, 2016, doi: 10.1039/C6RA03613A.

- [8] M. Ramesh Kumar, S. Ryman, M. O. Tareq, D. A. Buchanan, and M. S. Freund, “Chemical diversity in electrochemically deposited conducting polymer-based sensor arrays,” *Sensors Actuators, B Chem.*, vol. 202, pp. 600–608, 2014, doi: 10.1016/j.snb.2014.05.120.
- [9] S. E. Zohora and N. Hundewale, “Chemical Sensors Employed In Electronic Noses : A Review,” *Soft Comput. Eng.*, vol. 3, no. 2, pp. 405–408, 2013, doi: 10.1007/978-3-642-31600-5.
- [10] J. Gutiérrez and M. C. Horrillo, “Talenta Advances in arti fi cial olfaction : Sensors and applications,” vol. 124, pp. 95–105, 2014, doi: 10.1016/j.talanta.2014.02.016.
- [11] R.W. Moncrieff, “An instrument for measuring and classifying odors,” *J. Appl. Physiol.*, vol. 16, no. July 1961, p. Pages 742-749, 1961, [Online]. Available: <http://jap.physiology.org.uml.idm.oclc.org/content/jap/16/4/742.full.pdf>.
- [12] T. Seiyama, K. Fujiishi, M. Nagatani, and A. Kato, “A New Detector for Gaseous Components Using Zinc Oxide Thin Films,” *J. Soc. Chem. Ind. Japan*, vol. 66, no. 5, pp. 652–655, 1963, doi: 10.1246/nikkashi1898.66.5_652.
- [13] S. Y. Park, Y. Kim, T. Kim, T. H. Eom, S. Y. Kim, and H. W. Jang, “Chemoresistive materials for electronic nose: Progress, perspectives, and challenges,” *InfoMat*, vol. 1, no. 3, pp. 289–316, 2019, doi: 10.1002/inf2.12029.
- [14] S. W. Chiu and K. T. Tang, *Towards a chemiresistive sensor-integrated electronic nose: a review*, vol. 13, no. 10. 2013.
- [15] A. Dey, “Semiconductor metal oxide gas sensors: A review,” *Mater. Sci. Eng. B*, vol. 229,

- no. July 2017, pp. 206–217, Mar. 2018, doi: 10.1016/j.mseb.2017.12.036.
- [16] N. Barsan and U. Weimar, “Conduction model of metal oxide gas sensors,” *J. Electroceramics*, vol. 7, no. 3, pp. 143–167, 2001, doi: 10.1023/A:1014405811371.
- [17] T. Tesfamichael, M. Arita, T. Bostrom, and J. Bell, “Thin film deposition and characterization of pure and iron-doped electron-beam evaporated tungsten oxide for gas sensors,” *Thin Solid Films*, vol. 518, no. 17, pp. 4791–4797, 2010, doi: 10.1016/j.tsf.2010.01.037.
- [18] M. Löfdahl, C. Utaiwasin, A. Carlsson, I. Lundström, and M. Eriksson, “Gas response dependence on gate metal morphology of field-effect devices,” *Sensors Actuators, B Chem.*, vol. 80, no. 3, pp. 183–192, 2001, doi: 10.1016/S0925-4005(01)00886-3.
- [19] P. C. Chen, G. Shen, and C. Zhou, “Chemical sensors and electronic noses based on 1-D metal oxide nanostructures,” *IEEE Trans. Nanotechnol.*, vol. 7, no. 6, pp. 668–682, 2008, doi: 10.1109/TNANO.2008.2006273.
- [20] N. Joshi, T. Hayasaka, Y. Liu, H. Liu, O. N. Oliveira, and L. Lin, “A review on chemiresistive room temperature gas sensors based on metal oxide nanostructures, graphene and 2D transition metal dichalcogenides,” *Microchim. Acta*, vol. 185, no. 4, 2018, doi: 10.1007/s00604-018-2750-5.
- [21] W. Göpel, “Chemical imaging: I. Concepts and visions for electronic and bioelectronic noses | Presented in part as plenary talk at EUROSENSORS 1997 (Warsaw, PL).1,” *Sensors Actuators B Chem.*, vol. 52, no. 1–2, pp. 125–142, Sep. 1998, doi: 10.1016/S0925-4005(98)00267-6.

- [22] W. Gopel, "From electronic to bioelectronic olfaction, or: From artificial 'moses' to real noses," *Sensors Actuators, B Chem.*, vol. 65, no. 1, pp. 70–72, 2000, doi: 10.1016/S0925-4005(99)00308-1.
- [23] S. H. Lee and T. H. Park, "Recent advances in the development of bioelectronic nose," *Biotechnol. Bioprocess Eng.*, vol. 15, no. 1, pp. 22–29, 2010, doi: 10.1007/s12257-009-3077-1.
- [24] H. S. Song, S. H. Lee, E. H. Oh, and T. H. Park, "Expression, solubilization and purification of a human olfactory receptor from escherichia coli," *Curr. Microbiol.*, vol. 59, no. 3, pp. 309–314, 2009, doi: 10.1007/s00284-009-9435-6.
- [25] H. J. Ko and T. H. Park, "Bioelectronic nose and its application to smell visualization," *J. Biol. Eng.*, vol. 10, no. 1, p. 17, Dec. 2016, doi: 10.1186/s13036-016-0041-4.
- [26] A. F. Smith *et al.*, "Bioelectronic protein nanowire sensors for ammonia detection," *Nano Res.*, vol. 13, no. 5, pp. 1479–1484, May 2020, doi: 10.1007/s12274-020-2825-6.
- [27] S. H. Lee *et al.*, "Mimicking the human smell sensing mechanism with an artificial nose platform," *Biomaterials*, vol. 33, no. 6, pp. 1722–1729, Feb. 2012, doi: 10.1016/j.biomaterials.2011.11.044.
- [28] T. T. Dung, Y. Oh, S. J. Choi, I. D. Kim, M. K. Oh, and M. Kim, "Applications and advances in bioelectronic noses for odour sensing," *Sensors (Switzerland)*, vol. 18, no. 1, 2018, doi: 10.3390/s18010103.
- [29] G. Panneerselvam, V. Thirumal, and H. M. Pandya, "Review of surface acoustic wave

- sensors for the detection and identification of toxic environmental gases/vapours,” *Arch. Acoust.*, vol. 43, no. 3, pp. 357–367, 2018, doi: 10.24425/123908.
- [30] G. Korotcenkov, *Handbook of Gas Sensor Materials*, vol. 2. New York, NY: Springer New York, 2014.
- [31] K. J. Albert *et al.*, “Cross-Reactive Chemical Sensor Arrays,” *Chem. Rev.*, vol. 100, no. 7, pp. 2595–2626, Jul. 2000, doi: 10.1021/cr980102w.
- [32] X. Qi, J. Liu, Y. Liang, J. Li, and S. He, “The response mechanism of surface acoustic wave gas sensors in real time,” *Jpn. J. Appl. Phys.*, vol. 58, no. 1, 2019, doi: 10.7567/1347-4065/aaf223.
- [33] W. H. King, “Piezoelectric Sorption Detector.,” *Anal. Chem.*, vol. 36, no. 9, pp. 1735–1739, Aug. 1964, doi: 10.1021/ac60215a012.
- [34] J. D. N. Cheeke and Z. Wang, “Acoustic wave gas sensors,” *Sensors Actuators, B Chem.*, vol. 59, no. 2, pp. 146–153, 1999, doi: 10.1016/S0925-4005(99)00212-9.
- [35] I. Bársony, C. Dücsö, and P. Fürjes, *Solid State Gas Sensing*. Boston, MA: Springer US, 2009.
- [36] J. Devkota, P. R. Ohodnicki, and D. W. Greve, “SAW sensors for chemical vapors and gases,” *Sensors (Switzerland)*, vol. 17, no. 4, pp. 13–15, 2017, doi: 10.3390/s17040801.
- [37] J. Hodgkinson and R. P. Tatam, “Optical gas sensing: A review,” *Meas. Sci. Technol.*, vol. 24, no. 1, 2013, doi: 10.1088/0957-0233/24/1/012004.
- [38] R. Bogue, “Detecting gases with light: a review of optical gas sensor technologies,” *Sens.*

- Rev.*, vol. 35, no. 2, pp. 133–140, Mar. 2015, doi: 10.1108/SR-09-2014-696.
- [39] D. Popa and F. Udrea, “Towards integrated mid-infrared gas sensors,” *Sensors (Switzerland)*, vol. 19, no. 9, pp. 1–15, 2019, doi: 10.3390/s19092076.
- [40] T. A. Dickinson, J. White, J. S. Kauer, and D. R. Walt, “A chemical-detecting system based on a cross-reactive optical sensor array,” *Nature*, vol. 382, no. 6593, pp. 697–700, 1996, doi: 10.1038/382697a0.
- [41] W. Jin, H. L. Ho, Y. C. Cao, J. Ju, and L. F. Qi, “Gas detection with micro- and nano-engineered optical fibers,” *Opt. Fiber Technol.*, vol. 19, no. 6 PART B, pp. 741–759, 2013, doi: 10.1016/j.yofte.2013.08.004.
- [42] H. Shirakawa, E. J. Louis, A. G. MacDiarmid, C. K. Chiang, and A. J. Heeger, “Synthesis of electrically conducting organic polymers: Halogen derivatives of polyacetylene, (CH)_x,” *J. Chem. Soc. Chem. Commun.*, no. 16, pp. 578–580, 1977, doi: 10.1039/C39770000578.
- [43] J. J. Miasik, A. Hooper, and B. C. Tofield, “Conducting polymer gas sensors,” *J. Chem. Soc. Faraday Trans. 1 Phys. Chem. Condens. Phases*, vol. 82, no. 4, pp. 1117–1126, 1986, doi: 10.1039/F19868201117.
- [44] S. J. Park, C. S. Park, and H. Yoon, “Chemo-electrical gas sensors based on conducting polymer hybrids,” *Polymers (Basel)*, vol. 9, no. 5, 2017, doi: 10.3390/polym9050155.
- [45] Y. C. Wong, B. C. Ang, A. S. M. A. Haseeb, A. A. Baharuddin, and Y. H. Wong, “Review—Conducting Polymers as Chemiresistive Gas Sensing Materials: A Review,” *J. Electrochem. Soc.*, vol. 167, no. 3, p. 037503, 2020, doi: 10.1149/2.0032003jes.

- [46] B. Lakard, S. Carquigny, O. Segut, T. Patois, and S. Lakard, "Gas Sensors Based on Electrodeposited Polymers," *Metals (Basel)*, vol. 5, no. 3, pp. 1371–1386, 2015, doi: 10.3390/met5031371.
- [47] A. G. MacDiarmid, "'Synthetic Metals': A Novel Role for Organic Polymers (Nobel Lecture)," *Angew. Chemie Int. Ed.*, vol. 40, no. 14, pp. 2581–2590, Jul. 2001, doi: 10.1002/1521-3773(20010716)40:14<2581::AID-ANIE2581>3.0.CO;2-2.
- [48] B. Weng, R. L. Shepherd, K. Crowley, A. J. Killard, and G. G. Wallace, "Printing conducting polymers," *Analyst*, vol. 135, no. 11, pp. 2779–2789, 2010, doi: 10.1039/c0an00302f.
- [49] Y. Wang, A. Liu, Y. Han, and T. Li, "Sensors based on conductive polymers and their composites: a review," *Polym. Int.*, vol. 69, no. 1, pp. 7–17, 2020, doi: 10.1002/pi.5907.
- [50] K. Potje-kamloth, "Chemical Gas Sensors Based on Organic Semiconductor Polypyrrole," *Crit. Rev. Anal. Chem.*, no. June 2002, pp. 121–140, 2002, doi: 10.1080/10408340290765489.
- [51] K. C. Persaud, "Polymers for chemical sensing," *Mater. Today*, vol. 8, no. 4, pp. 38–44, 2005, doi: 10.1016/S1369-7021(05)00793-5.
- [52] P. Taylor and K. Potje-kamloth, "Critical Reviews in Analytical Chemistry Chemical Gas Sensors Based on Organic Semiconductor Polypyrrole Chemical Gas Sensors Based on Organic Semiconductor Polypyrrole," no. May 2013, pp. 37–41, 2010.
- [53] A. A. Iyogun, M. R. Kumar, and M. S. Freund, "Chemically diverse sensor arrays based on

- electrochemically copolymerized pyrrole and styrene derivatives,” *Sensors Actuators, B Chem.*, vol. 215, pp. 510–517, 2015, doi: 10.1016/j.snb.2015.03.070.
- [54] A. A. Iyogun, “Chemically Diverse Sensor Arrays Based on Conducting Polymers in Sensing Characterization and Application,” University of Manitoba, Winnipeg, 2016.
- [55] M. O. Tareq, M. R. Kumar, M. Freund, and D. Buchanan, “An Extended Floating Gate Gas Sensor,” no. 2, pp. 275–279, 2012.
- [56] M. O. Tareq, “Floating Gate Metal-Oxide-Semiconductor Based Gas Sensor,” University of Manitoba, Winnipeg, 2014.
- [57] D. Kahng and S. M. Sze, “A Floating Gate and Its Application to Memory Devices,” *Bell Syst. Tech. J.*, vol. 46, no. 6, pp. 1288–1295, 1967, doi: 10.1002/j.1538-7305.1967.tb01738.x.
- [58] M. A. Reyes Barranca *et al.*, “Using a Floating-Gate MOS Transistor as a Transducer in a MEMS Gas Sensing System,” *Sensors*, vol. 10, no. 11, pp. 10413–10434, Nov. 2010, doi: 10.3390/s101110413.
- [59] N. Lajnef, N. G. Elvin, and S. Chakrabarty, “A piezo-powered floating-gate sensor array for long-term fatigue monitoring in biomechanical implants,” *IEEE Trans. Biomed. Circuits Syst.*, vol. 2, no. 3, pp. 164–172, 2008, doi: 10.1109/TBCAS.2008.2001473.
- [60] S. T. Wang, “On the I-V characteristics of floating-gate MOS transistors,” *Electron Devices, IEEE Trans.*, vol. 26, no. 9, pp. 1292–1294, 1979, doi: 10.1109/T-ED.1979.19595.
- [61] R. H. Fowler and L. Nordheim, “Electron emission in intense electric fields,” *Proc. R. Soc.*

- London. Ser. A, Contain. Pap. a Math. Phys. Character*, vol. 119, no. 781, pp. 173–181, 1928, doi: 10.1098/rspa.1928.0091.
- [62] E. H. Snow, “Fowler-Nordheim tunneling in SiO₂ films,” *Solid State Commun.*, vol. 5, no. 10, pp. 813–815, 1967, doi: 10.1016/0038-1098(67)90715-6.
- [63] A. Thomsen and M. A. Brooke, “A floating-gate MOSFET with tunneling injector fabricated using a standard double-polysilicon CMOS process,” *IEEE Electron Device Lett.*, vol. 12, no. 3, pp. 111–113, 1991, doi: 10.1109/55.75728.
- [64] G. Groeseneken, H. Maes, J. Van Houdt, and J. Witters, “Basics of nonvolatile semiconductor memory devices,” *Nonvolatile Semicond. Mem. Technol.*, pp. 1–88, 1971.
- [65] K. Cao, “A Chemical Sensor Design Using a Standard CMOS Process,” University of Manitoba, Winnipeg, 2007.
- [66] R. Jacob Baker, *CMOS Circuit Design, Layout and Simulation*, no. 2nd Edition. 2005.
- [67] G. Li and P. Miao, *Electrochemical Analysis of Proteins and Cells*. Berlin, Heidelberg: Springer Berlin Heidelberg, 2013.
- [68] M. Datta, S. A. Merritt, and E. Mario Dagenais, “Electroless metallization of aluminum bond pads on CMOS driver chip for flip-chip attachment to vertical cavity surface emitting lasers (VCSEL’s),” *IEEE Trans. Components Packag. Technol.*, vol. 22, no. 2, pp. 299–306, 1999, doi: 10.1109/6144.774749.
- [69] R. G. KING, “Electroplating on Aluminium,” *Surf. Treat. Finish. Alum.*, pp. 34–46, 1988, doi: <https://doi.org/10.1016/B978-0-08-031138-8.50010-0>.

- [70] R. Ansari, “Polypyrrole Conducting Electroactive Polymers: Synthesis and Stability Studies,” *CODEN ECJHAO E-Journal Chem.*, vol. 3, no. 4, pp. 973–4945, 2006, doi: 10.1155/2006/860413.
- [71] A. Ortiz-Conde, F. J. García-Sánchez, J. Muci, A. Terán Barrios, J. J. Liou, and C. S. Ho, “Revisiting MOSFET threshold voltage extraction methods,” *Microelectron. Reliab.*, vol. 53, no. 1, pp. 90–104, 2013, doi: 10.1016/j.microrel.2012.09.015.
- [72] P. N. Bartlett and S. K. Ling-Chung, “Conducting polymer gas sensors Part III: Results for four different polymers and five different vapours,” *Sensors and Actuators*, vol. 20, no. 3, pp. 287–292, 1989, doi: 10.1016/0250-6874(89)80127-1.
- [73] R. E. Martin, T. J. Peckham, and A. B. Holmes, “Conjugated Oligomers and Polymers, Synthesis of,” *Encycl. Mater. Sci. Technol.*, pp. 1509–1526, 2001, doi: 10.1016/b0-08-043152-6/00272-2.
- [74] J. Lever, M. Krzywinski, and N. Altman, “Points of Significance: Principal component analysis,” *Nat. Methods*, vol. 14, no. 7, pp. 641–642, 2017, doi: 10.1038/nmeth.4346.
- [75] A. J. Heeger, “Semiconducting and metallic polymers: The fourth generation of polymeric materials,” *J. Phys. Chem. B*, vol. 105, no. 36, pp. 8475–8491, 2001, doi: 10.1021/jp011611w.
- [76] J. Heinze, B. A. Frontana-Uribe, and S. Ludwigs, “Electrochemistry of conducting polymers-persistent models and new concepts,” *Chem. Rev.*, vol. 110, no. 8, pp. 4724–4771, 2010, doi: 10.1021/cr900226k.

- [77] J. L. Bredas and G. B. Street, "Polarons, Bipolarons, and Solitons in Conducting Polymers," *Acc. Chem. Res.*, vol. 18, no. 10, pp. 309–315, 1985, doi: 10.1021/ar00118a005.
- [78] H. Bai and G. Shi, "Gas Sensors Based on Conducting Polymers," *Sensors*, vol. 7, no. 3, pp. 267–307, Mar. 2007, doi: 10.3390/s7030267.
- [79] Z. H. N. Al-Azri *et al.*, "The roles of metal co-catalysts and reaction media in photocatalytic hydrogen production: Performance evaluation of M/TiO₂ photocatalysts (M = Pd, Pt, Au) in different alcohol–water mixtures," *J. Catal.*, vol. 329, no. June, pp. 355–367, Sep. 2015, doi: 10.1016/j.jcat.2015.06.005.